LB271.

Structural alterations in Spinocerebellar Ataxia Type 3: A 3T MRI study of cerebellar peduncles and cerebral pathways

M. Ferreira[1], P. Wegner[1], J. Theisen[1], E. M. study group[1], T. Klockgether[1], J. Faber[1]

[1]DZNE, Bonn, Germany

Introduction: Spinocerebellar ataxia type 3 (SCA3), is the most common autosomal dominantly inherited ataxia worldwide, caused by a translated CAG repeat expansion mutation[1]. With the start of the first clinical gene silencing trials, there is an urgent need for non-invasive quantitative biomarkers. Of particular interest is the pre-ataxic stage of SCA3 (preSCA3), since clinical scales lack sensitivity prior to the onset of ataxia. Characterizing features of SCA3 include neuropathology of the dentate nucleus, basal ganglia, substantia nigra and spinal cord[1] causing atrophy of the brainstem and cerebellum and consequently impairment of the associated white matter (WM) tracts. Understanding these structural alterations can be further enhanced through diffusion MRI techniques. By describing the directionality of water diffusion, fractional anisotropy (FA) reflects the microstructure of the tissue and can be interpreted as a marker of WM integrity. Herein, we investigate WM tracts related to the neuropathological of SCA3, specifically focusing on the corticospinal tracts (CST) as well as the superior, middle, and inferior cerebellar peduncles (SCP, MCP, ICP).

Methods: In a multicenter, cross-sectional study we acquired diffusion data of 169 participants (46 HC, 35 preSCA3, 88 SCA3). Data was acquired on 3T Siemens scanners using an EPI sequence with sequence parameters described in Fig.1. Data was pre-processed with FSL[2,3]. Tracking was performed with MRtrix using multi-shell multi-tissue constrained spherical deconvolution[4]. Streamlines were generated by entering pre-defined regions of interest[5,6], cleaned and clipped[6]. FA maps were generated with FSL and harmonized with COMBAT[7]. Scale for the Assessment and Rating of Ataxia (SARA) values, indicating ataxia severity, were plotted against the mean FA of each tract (Fig. 2). The coefficient of determination (R^2) and the associated p-value of the linear relationship were added to the top right side of each subplot. The delineation of FA was given for 100 equidistant locations along the CST and 30 locations for the cerebellar peduncles. Here, we used a linear regression model between the FA values at each location and the variables group, gender, and age. To visualize significant inter-group differences following Tukey post hoc analysis, we added coloured horizontal lines where the respective group comparison differed significantly (p-value < 0.05).

Results: In SCA3, we found a negative correlation of SARA with mean FA in the CST, SCP, MCP and ICP (Fig. 2). Additionally, significant linear relationship between mean FA and SARA was found in SCA3 for the left CST, left and right SCP, left and right ICP, and, in preSCA3, for the left and right SCP. FA profiles are given in Fig. 3. We found consistent decrease in the FA values across all locations within the tracts in SCA3 compared to HCs. FA within the cerebellar peduncles of preSCA3 is lower than that of HCs, a pattern that is less prominent within the CST. In the cerebellar peduncles, the extent of the alterations was almost comparable between preSCA3 and SCA3.

Discussion: In this study we showed statistically significant relationships between mean FA and SARA scores particularly for the SCA3 group. FA was already decreased in the SCP before ataxia onset. This suggests an early affection of the WM integrity, confirming that structural changes occur even before the full clinical manifestation of SCA3. The SCP is a crucial connection between the cerebellum and other brain regions involved in motor control and coordination as part of the dentato-rubro-thalamo-cortical tract. Therefore, the sensitivity of the SCP to changes in FA might be attributed to its strategic position in transmitting information related to motor function. Fig. 3 shows a sequential pattern with HCs having higher FA values compared to those of preSCA3, which, in turn, are higher than those in SCA3. Comparing HC and SCA3 showed significant differences across all locations in all tracts. Notably, the comparisons of HC and preSCA3 revealed significant differences in all peduncles. A significant decrease in FA values is attributed to the progressive deterioration of WM microstructures compromising the integrity of the WM tracts.

Conclusion: These findings underline the significance of the cerebro-cerebellum WM connections and the potential of FA as a promising imaging biomarker in particular for the pre-ataxic stage of SCA3.

References:
1 - Klockgether et al, 2019; doi:10.1038/s41572-019-0074-3
2 - Andersson et al, 2015; doi:10.1016/j.neuroimage.2015.10.019
3 - Andersson et al, 2003; doi:10.1016/S1053-8119(03)00336-7
4 - Tournier et al, 2009; doi:10.1016/j.neuroimage.2019.116137
5 - Wakana et al, 2007; doi:10.1016/j.neuroimage.2007.02.049
6 - Yeatman et al, 2012; doi:10.1371/journal.pone.0049790
7 - Fortin et al, 2017; doi:10.1016/j.neuroimage.2017.08.047

b-values (s/mm^2)	700 and 1000
number of directions per shell	30
resolution	2 mm isotropic
TE (ms)	88
TR (ms)	12100
nominal flip angle	90

Fig. 1. Sequence parameters.

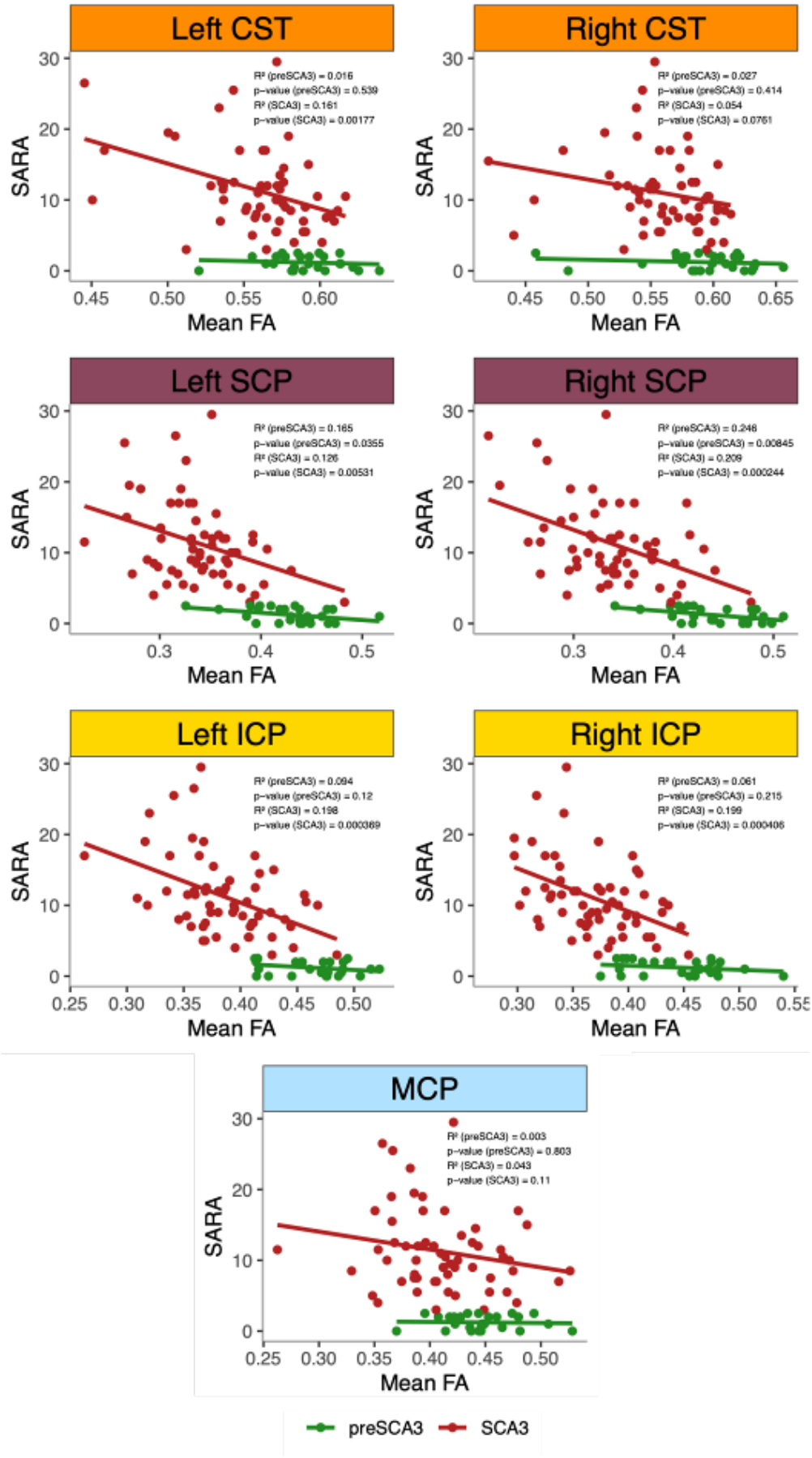

Fig. 2. Plots of Scale for the Assessment and Rating of Ataxia (SARA) values, indicating ataxia severity, against the mean FA of each tract (orange - CST; purple - SCP; yellow - ICP, blue - MCP) for both mutation carrier groups (green - preSCA3; red - SCA3). The coefficient of determination (R2) and the associated p-value of the linear relationship were added to the top right side of each subplot.

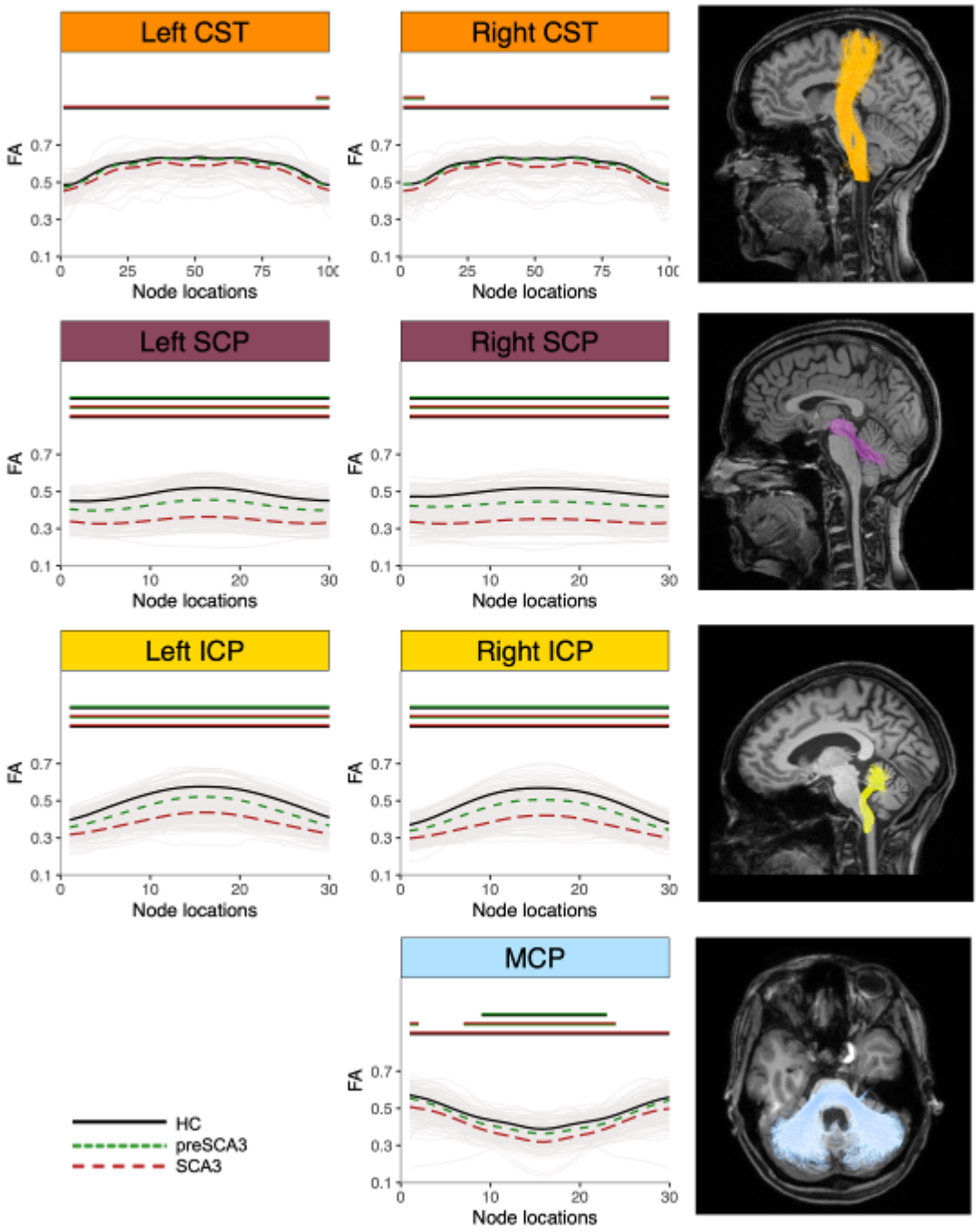

Fig. 3. Fractional anisotropy profiles of involved WM tracts in SCA3 (orange - CST; purple - SCP; yellow - ICP, blue - MCP). For each tract, the mean FA profile at baseline for HC (black), SCA3 (red), and preSCA3 (green). The horizontal doubled lines in the upper part of each subplot are located at those locations where the respective group comparison differed significantly (p-value < 0.05). For example, doubled line black and red means that in those locations there was significantly differences between HCs and SCA3.

LB272.

Rapid quantification of T_1 in white and grey matter at 64 mT

B. Lena[1], Y. Dong[1], F. Padormo[2], R. P. A. Teixeira[2], P. C. Sundgren[3,4], A. Webb[1], E. Ljungberg[5,6]

[1]Leids Universitair Medisch Centrum, C.J. Gorter MRI Center, Leiden, Netherlands
[2]Hyperfine Inc., Guilford, CT, United States
[3]Lund University, Section of Diagnostic Radiology, Department of Clinical Sciences Lund, Lund, Sweden
[4]Lund University, Lund BioImaging Center, Lund, Sweden
[5]Lund University, Department of Medical Radiation Physics, Lund, Sweden
[6]King's College London, Department of Neuroimaging, London, United Kingdom

Introduction: Low-field, point-of-care (POC) MRI is a promising technology with the potential for increased accessible and efficient diagnostics (1). Quantitative parameter mapping is an important tool for future neuroscience studies into brain development, disease progression and technique optimization for novel clinical applications and offers an important venue for fully utilizing the value of POC MRI. Recent studies have explored the characterization of T_1 values in the brain at very low field (2–4), but with long acquisition times. We present a method for reducing the acquisition time from 40 min down to 10 min using a locally low rank (LLR) constraint (5,6) for image reconstruction. The proposed method is evaluated in a quantitative phantom and in vivo experiments.

Methods:
Acquisition: A Hyperfine Swoop (Hyperfine Inc., CT) operating at 64 mT with a single coil transmit 8-channel receive head coil was used for all experiments. T_1 maps were acquired using a 3D inversion recovery turbo spin-echo (TSE) sequence, with acquisition parameters: TR=1500 ms, effective TE=5 ms, echo train length 32, 6 inversion times (TI) logarithmically spaced between 50 and 1000 ms, FOV 220x180x200 mm^3, resolution 1.6x1.6x5 mm^3. The fully sampled protocol (R=1) had a total scan time of 42.3 min, 7.05 min per TI. Using the same parameters but with a k-space undersampling factor of 4 (R=4), the total scan time was reduced to 10.8 min, 1.8 min per TI.

Reconstructions and Fitting: Image reconstruction was performed using Sigpy (v0.1.25) with sensitivity maps generated using JSENSE (7), and final images reconstructed with a Locally Low Rank (LLR) constraint (5,6) with a regularization factor 3 and a block size 4x4x4. To obtain real-valued data for T_1-fitting, phase correction was performed using the longest TI image (8). The real data were then fitted to the signal equation presented by Padormo et al. (4).

Experiments: The performance of the R=4 T_1 protocol was tested against R=1 in a quantitative phantom (Caliber MRI, Boulder, CA, model 137) which included T_1-mimics with known concentrations of NiCl. To demonstrate the method in vivo, the R=4 protocol was used in four healthy volunteers, who signed informed consent prior to scanning and were scanned with the approval of the institutional review board (NL53099.041.15). The R=1 protocol was acquired in two volunteers for comparison. The average T_1 values in white (WM) and grey matter (GM) were calculated by placing a ROIs of 16 pixels in frontal white matter and cortical grey matter, both on the left and right side of the brain (Figure 4A).

Results: The phantom experiment demonstrated good agreement between the R=1 and R=4 protocols for the phantom vials with a concentration that corresponded to T_1 values expected in vivo (Figure 1A-C). A linear relationship between R_1 ($1/T_1$) and NiCl concentration is expected and was observed. The longest and shortest T_1s, i.e., the lowest, and highest NiCl concentration, produced unreliable T_1-fits since the protocol was not optimized for this parameter range.

Similar image contrast was observed when comparing the R=1 and R=4 datasets and the main anatomical structures were identifiable in both cases (Figure 2). The R=4 images showed minor undersampling artefacts and slight blurring. A comparison of the T_1-maps calculated from the R=1 and R=4 datasets is shown in Figure 3 and shows a slight blurring with R=4. Bland-Altman analysis of the two acquisitions demonstrated no apparent bias in the estimated T_1 values. The mean T_1 values across all four subjects with R=4 were 352 ± 5 ms in GM and 261 ± 3 ms in WM (mean±SE).

Discussion: The T_1 values measured using the accelerated protocol (R=4) were consistent with both the fully sampled T_1 estimates from this study, and the T_1 values reported in other works at similar field strengths in vivo (2,3). The protocol used in this work was optimized for WM and GM. Quantification of T_1 in CSF would require longer inversion delay, and thus longer acquisition time. In this work we have focused on accelerating the protocol by optimizing the image reconstruction, future work should explore potential alternatives to TSE readout for further accelerating the data acquisition.

Conclusion: We have demonstrated a method for rapid T_1 mapping on a 64 mT portable MRI system which enabled accurate quantification of T_1 values in WM and GM, with minimal compromise in image quality.

References

1. Arnold TC, et al. Magn Reson Imag. 2022 Sep 19
2. Jordanova KV, et al. Magn Reson Mater Phy. 2023 May 20
3. O'Reilly T & Webb AG. Magn Reson Med. 2022;87(2):884–95.
4. Padormo F, et al. Magn Reson in Med. 2023;89(3):1016–25.
5. Zhang T, et al. Magn Reson Med. 2015;73(2):655–61.
6. Tamir JI, et al. Magn Reson Med. 2017;77(1):180–95.
7. Ying L & Sheng J. Magn Reson Med. 2007 Jun;57(6):1196–202.
8. Bydder M, et al., Magn Reson Med. 2002 Mar;47(3):539–48.

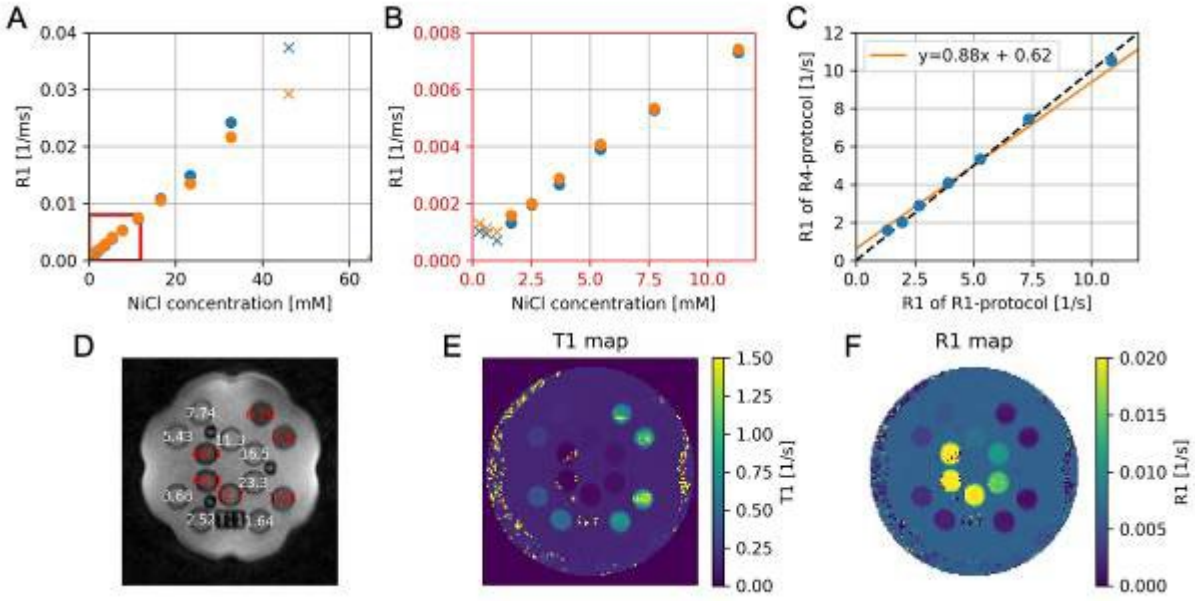

Fig.1: (A) and (B): Calculated R_1 values in the phantom for the two protocols vs. phantom doping agent (NiCl) concentration.(C): Correlation plot of R_1 in the R=1 and R=4 protocols showing good correspondence. (D): Image of phantom with the NiCl concentrations. (E) and (F): T_1 and R_1 map of the phantom.

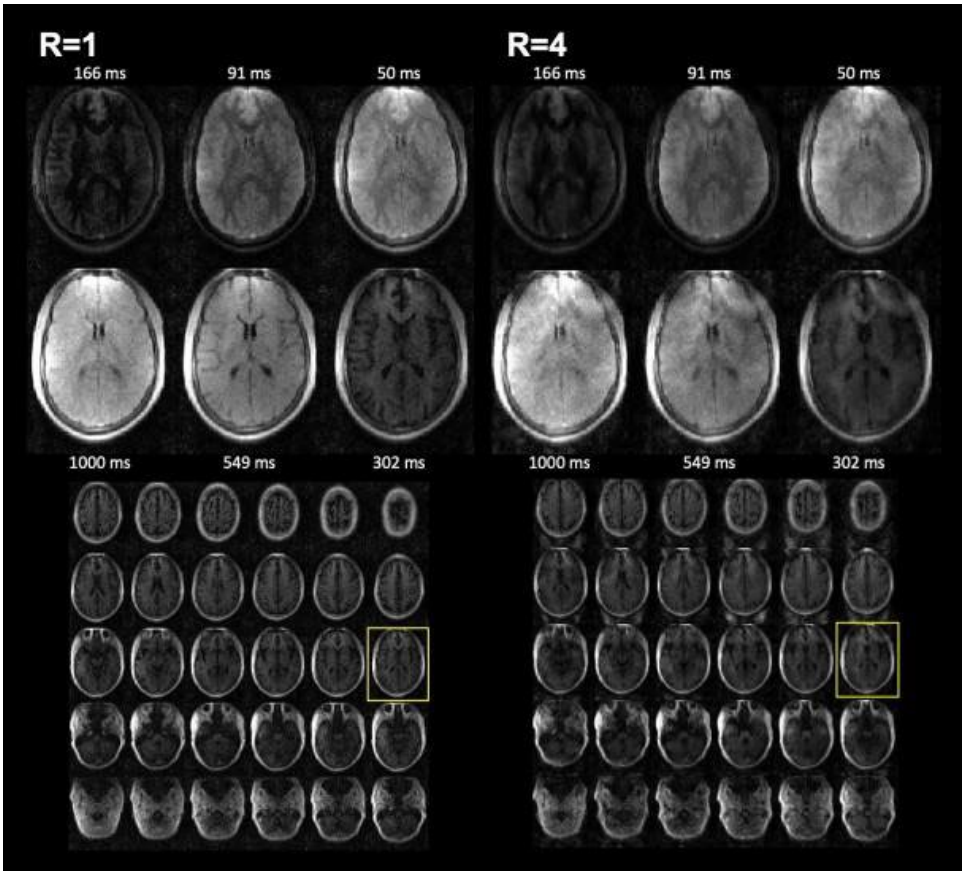

Fig.2. Example of the data from each inversion time with R=1 and R=4 from the same volunteer (V2), reconstructed with a locally low rank constraint (LLR).

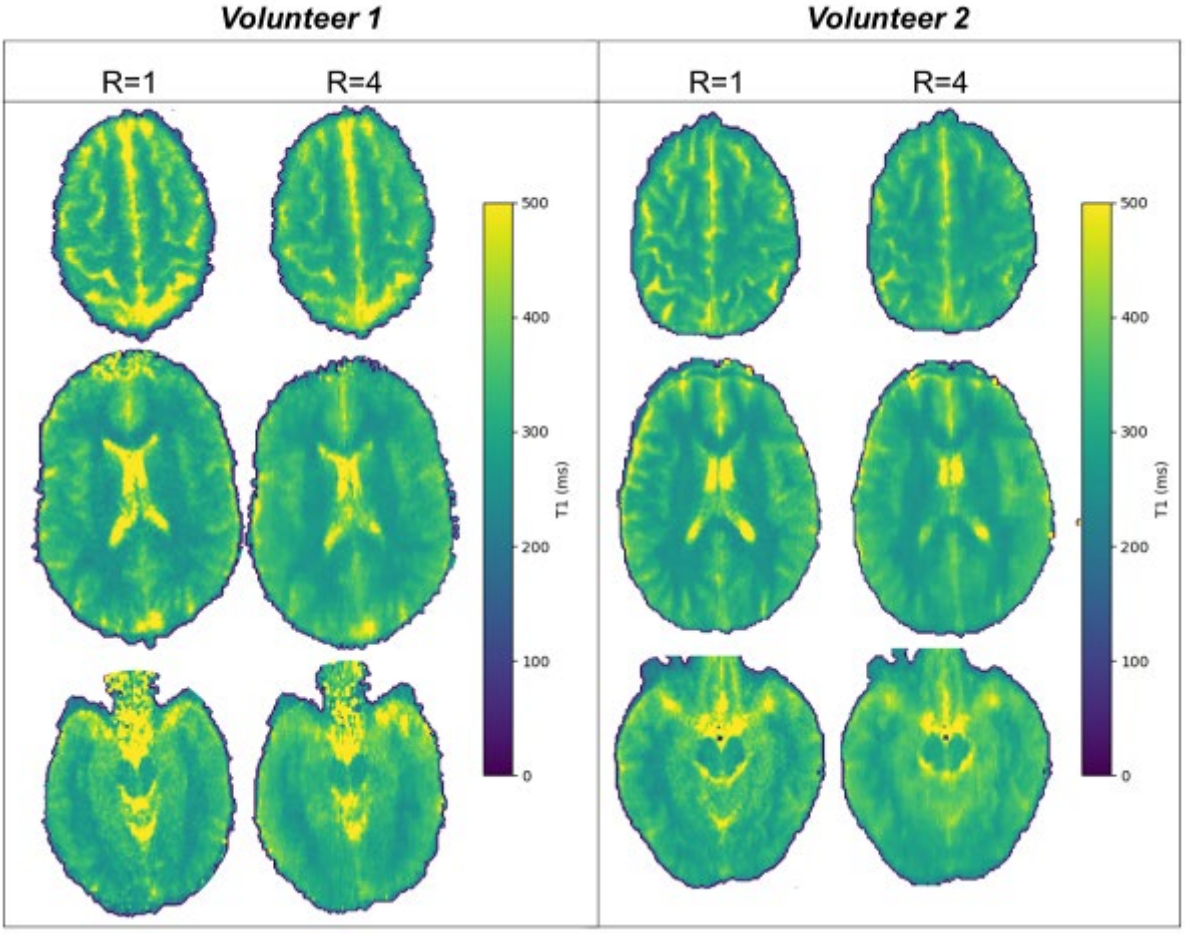

Fig.3. Comparison of T_1 maps calculated from the R=1 and R=4 datasets.

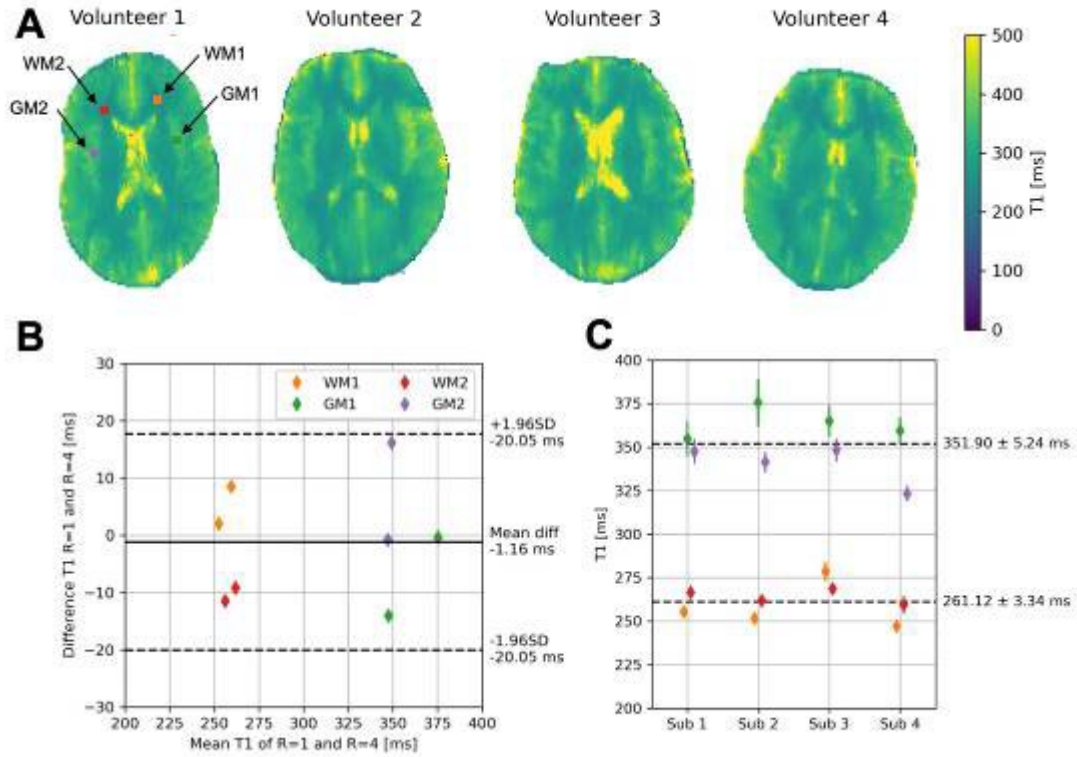

Fig.4. (A) T_1 maps from the R=4 data, with the ROIs shown in volunteer 1. (B) Bland-Altman plot comparing the R=1 and R=4 protocol from two volunteers, showing no significant difference. (C) T_1 values in white and grey matter for the four volunteers with R=4 data. The dashed lines show WM and GM averages and standard error.

LB273.

A novel compact Wireless Integrated Sensing Detector for EEG and MRI (WISDEM)

Y. Chen[1,2], W. Qian[3], X. Yu[4], C. Qian[2,3]

[1]Max Planck Institute for Biological Cybernetics, Tuebingen, Germany
[2]Michigan State University, Radiology, East Lansing, MI, United States
[3]Michigan State University, Department of Electrical and Computer Engineering, East Lansing, MI, United States
[4]Massachusetts General Hospital and Harvard Medical School, Martinos Center for Biomedical Imaging, Charlestown, MA, United States

Introduction: Understanding the quantitative relationship between the BOLD signal and the underlying neural activities is crucial for interpreting fMRI data and better understanding neurovascular coupling. Extracellular local field potential (LFP) recordings could provide complementary electrophysiological information. However, two challenges limit this combined method in most fMRI labs: First, the complicated MRI apparatus and sequences bring tremendous noise to LFP signals when no Faraday cage is allowed inside the scanner. Second, the long connection cable to the conventional EEG electrodes picks up electromagnetic interference artifacts, making simultaneous fMRI/EEG difficult to implement. To overcome these challenges, we fabricated a wirelessly integrated sensor to detect simultaneous fMRI and LFP without modifications to the MRI scanner's hardware/software. This design provides the possibility to surpass conventional paradigms of concurrent fMRI/LFP, to boost their individual performance via complementary strengths, thus better interpreting fMRI and understanding neurovascular coupling.

Methods: Fig.1a shows the design of the WISDEM. We created a voltage-sensing resonator by filling the gaps of a rectangular inductor (blue lines) with 2 varactor diodes (red triangles) connected in head-to-head configuration (**Fig.1b**). When we connected two electrodes (pink) across circuit edges, low-frequency voltages applied across the sensing electrodes can be contactlessly detected as resonance frequency shifts [1]. We coaxially overlapped the resonator with another parametric resonator (orange rectangle) that can be antenna-powered to enable sustained circuit oscillation and enhance remote detectability [2]. To simultaneously acquire MRI and LFP signals and encode them onto the same oscillation carrier wave, we can adjust the pumping frequency on the antenna to make the oscillation carrier overlap with the edge of field-of-view in the frequency domain (**Fig.1c**). Subsequently, the fast (MRI) and slow (EEG) signals can be separated in the frequency domain for separate decoding.

All procedures in this study were conducted in accordance with guidelines set by the Institutional Animal Care and Use Committee of Michigan State University. The Sprague-Dawley rats were scanned in a 7T Bruker scanner and anesthesia was maintained via subcutaneous infusion of dexmedetomidine (0.1 mg/kg/h) during scanning. EEG and MRI signals were encoded onto the oscillation carrier signal of the WISDEM and detected by a 10 mm-diameter ring surface coil placed apart. After derivatizing the phase of the carrier signal, EEG and MRI signals can be separately retrieved by low-pass and high-pass filtering. EPI functional images are registered into the SIGMA rat brain atlas with the parameters as follows: TR=997.6 ms, TE=20.4 ms, FOV=78x26 mm, resolution=0.6 mm3, 326-kHz bandwidth, and LFPs were sampled at the same rate as the imaging bandwidth.

Results: As a proof-of-concept demonstration, we first detected BOLD signals from the right somatosensory forepaw region (SIFL) upon electrical forepaw stimulation (**Fig.2**). The robust functional maps overlaid on SIGMA rat brain atlas [3] and time courses indicate the reliable detectivity of WISDEM. Next, we validated this approach to measure LFPs with optogenetic stimulation in the left S1FL (**Fig.3c**). The optical fiber (200-μm) and a 75-μm copper wire as detection electrode were implanted in the left S1FL (0 mm AP, -4 mm ML from bregma, and -1.2 mm DV from brain surface, confirmed by high resolution T2RARE anatomical images). Upon light exposure, we observed increased BOLD in the S1FL simultaneously with LFPs (**Fig.3e**). **Fig.3d** shows negative and positive peak latency (9.07± 2.48 ms, and 18.24 ± 2.46 ms, respectively, mean ±Std) and laser power dependency from 4 rats, which are highly consistent with reported studies.

Discussion/Conclusion: We have constructed a multi-modal sensor that allows simultaneous encoding and wireless transmission of fMRI and LFP signals without modifications to the scanner's hardware/software. These signals can be received by a standard MRI coil, without the need to modify the scanner"s hardware/software. This device can be easily implemented in preclinical fMRI labs for combined electrophysiology-fMRI. It may also open up new avenues in brain research by providing a deeper understanding of neurovascular coupling in healthy and diseased brains.

References

1. Qian, et.al. Frequency Modulated Parametric Oscillation for Antenna Powered Wireless Transmission of Voltage Sensing Signals. IEEE Transaction on Biomedical Circuits and Systems, 13(6), (2019) 1783-1791.
2. Qian, et.al. Wireless Powered Encoding and Broadcasting of Frequency Modulated Detection Signals. IEEE Access, 8, (2020) 200450-200460.

3. Barriere, D.A., et al., *The SIGMA rat brain templates and atlases for multimodal MRI data analysis and visualization.* Nat Commun, 2019. **10**(1): p. 5699.

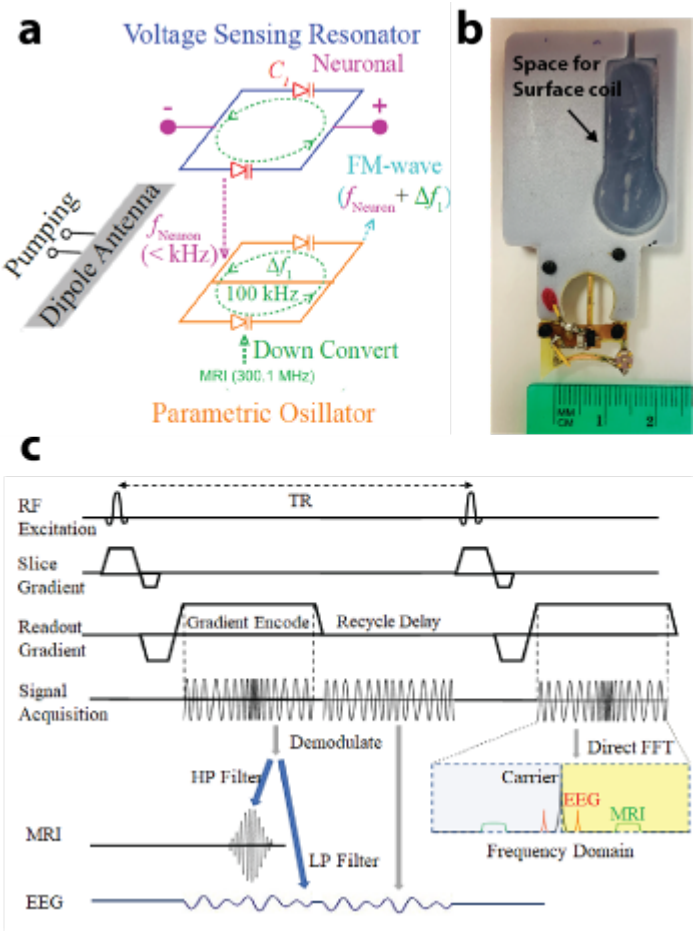

Fig.1. a. Diagrams and photograph of the WISDEM(b). c. During the gradient encoding period, because neuronal signals and down-converted MR signals have distinct frequency separations from the oscillation carrier wave (OCA), they can be encoded into the same CA but at different sidebands. After derivatizing the phase angles of the OCA, we can retrieve neuronal signals through low-pass filtering, and MRI signals through high-pass filtering.

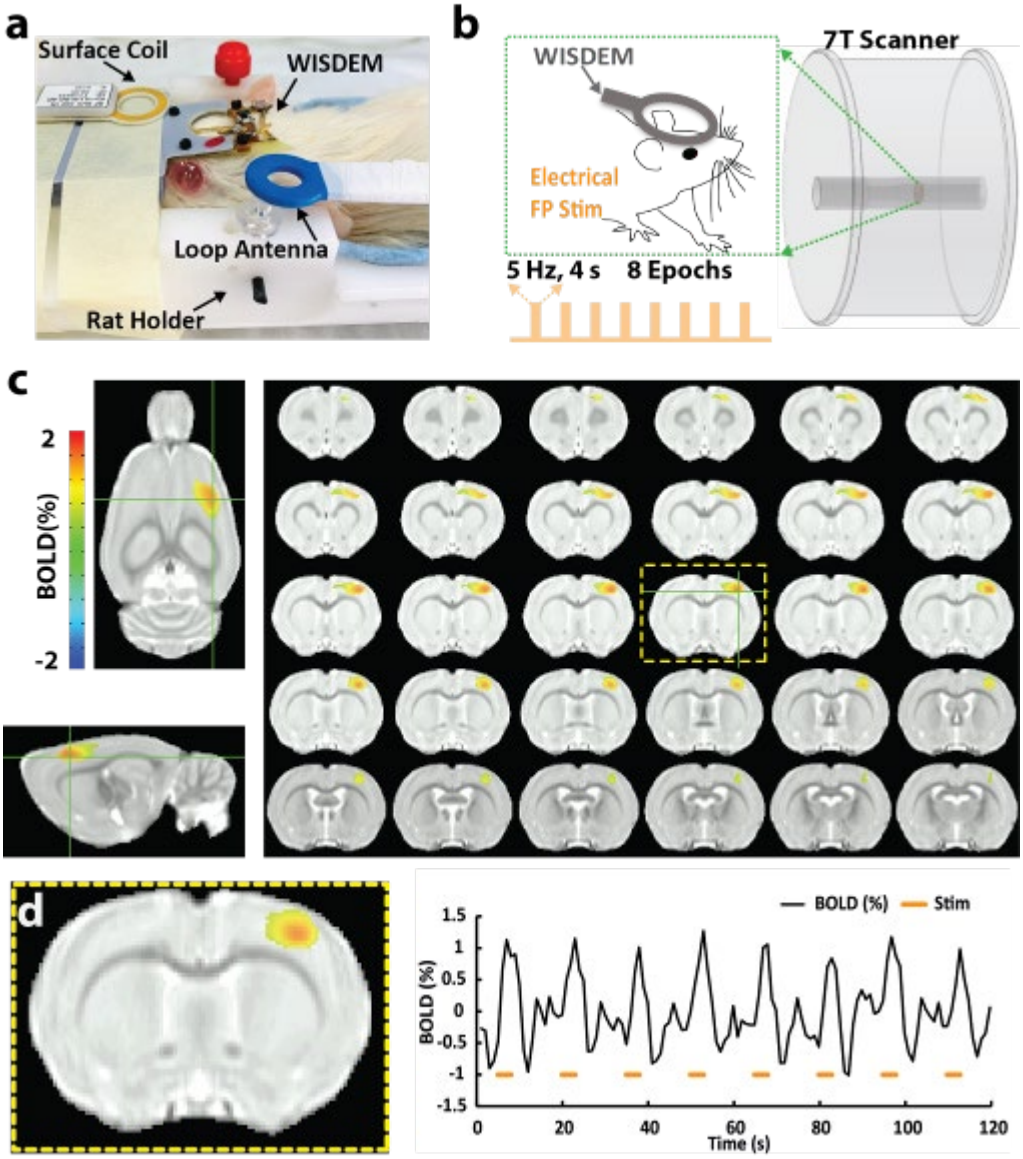

Fig.2. Validation of WISDEM. a. Photograph of WISDEM placed on the rat brain. b. The schematic drawing of the experiment design. c. Task evoked BOLD mapping overlaid on the SIGMA rat brain atlas [3] from a representative rat with an enlarged map and time courses in (d).

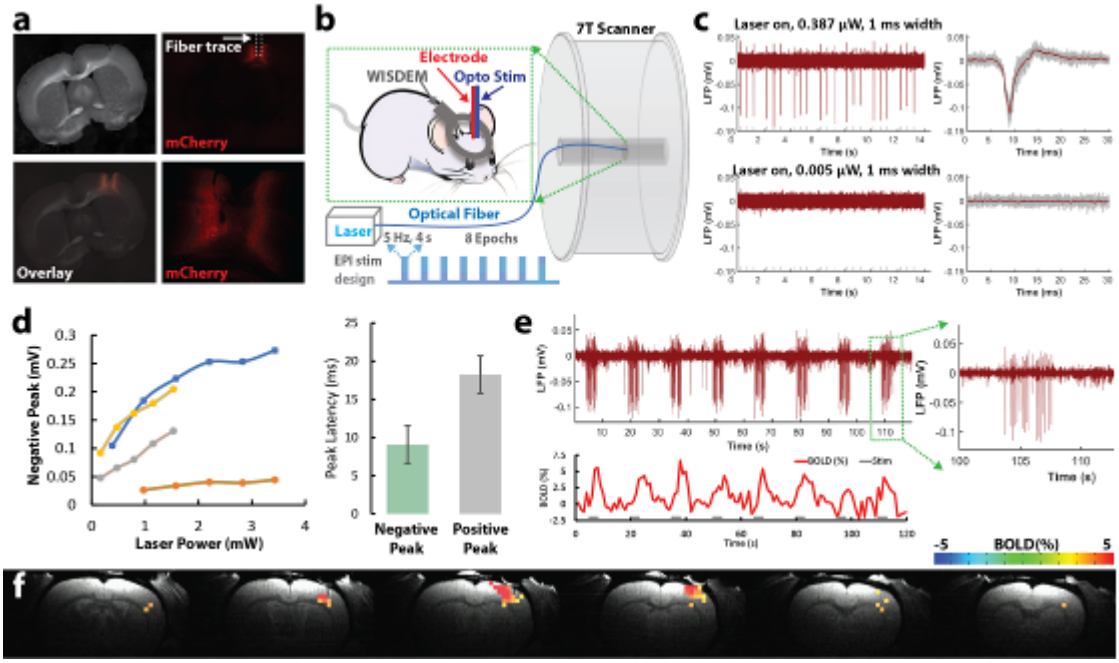

Fig.3. Validation of WISDEM with optogenetic stimulation. a. Virus expression (ChR2-mCherry). b. Experiment design c. Representative LFPs from Exp/Control trials. d. Time to a negative peak depends on laser power from 4 rats. e. LFPs and BOLD time course from EPI. f. Evoked BOLD mapping overlaid on RARE images from a representative rat.

LB274.

Deuterium MR spectroscopy and imaging of tumor models to examine their glycolytic / oxidative balance and inhibition of O_2 consumption

E. Berkhout[1], D. Boreel[1], J. van Asten[1], A. Veltien[1], S. Heskamp[1], A. Heerschap[1]

[1]Radboud University Medical Centre, Medical Imaging, Nijmegen, Netherlands

Introduction: The presence of O_2 in tumors is important for successful radiotherapy as it promotes ionization damage of DNA and can initiate anti-tumor immune responses. A promising way to increase the level of O_2 in tumors is by inhibiting its consumption in oxidative phosphorylation (OXPHOS) [1]. The effect of OXPHOS inhibitors on O_2-related metabolism can be investigated in model systems such as tumor cells growing in culture medium and subcutaneously implanted in mice. It has been demonstrated that O_2-related energy metabolism in tumors can be assessed by deuterium metabolic spectroscopy or imaging (DMS/DMI) after administration of deuterated D-glucose-6,6-d2 [2,3,4,5]. The aim of this study was therefore to use DMS/DMI to measure lactate production and glucose consumption, as markers for the balance in glycolytic/oxidative tumor metabolism, and to assess the effect of OXPHOS inhibitors on this balance in metabolically different tumor cells.

Methods: For in vitro studies the tumor cells MOC1 (mouse squamous cell carcinoma), B16ova (mouse melanoma), MC38 (colon carcinoma) were grown in DMEM to which 11 mM D-[6,6"2H2]glucose was added. After 1, 2, 4, 8, 24 and 48 hours a sample of 550 µl was obtained from the medium for 2H MRS. MOC1 and B16ova cells were also subjected for 24 hours to hypoxia (1% O2) and to 0.1 or 1.0 µM of complex 1 inhibitor IACS-010759.

^{2}H MRS was performed on a 500 MHz Bruker NMR machine. After field shimming on the H_2O signal (1H channel), ^{2}H MRS was performed without a lock with a 90^0 pulse (150 µs), a repetition time of 2 sec and 6144 averages. Postprocessing was done in Bruker Topspin by integrating the ^{2}H MR signals and correcting for the ^{2}H content per molecule to assess concentrations assuming initial [HOD]=13.8 mM.

For in vivo experiments tumors were grown subcutaneously on the hind limb of C57BL/6J mice up to ~500 mm^3 in size. Mice were anaesthetized with isoflurane. We injected 2 gr/kg [6,6 $^2H_2$]glucose in a 0.2 ml saline solution IV in ~10 sec. MR was performed on a Bruker Biospec at 11.7T with a home-built ^{2}H coil. After ^{1}H imaging and shimming, DMRS was performed with a 90^0 excitation pulse, TR = 500 ms, 2:24 min per acquisition. 3D DMI was performed with a nominal spatial resolution of 2x2x2 mm, TR = 400 ms, TE = 0.4 ms, total acquisition time of 36 min. Data was processed in DMIWizard with initial tissue [HOD]=13.7mM [5].

Results and discussion: ^{2}H MR spectra of medium of the cells showed decreasing signals for glucose and increasing signals for lactate and HOD (Fig 1a). The metabolite concentration/cell in the medium as a function of incubation time revealed that the MC38 and MOC1 cells produce more lactate than the B160va cells, despite that the latter consumes slightly more glucose (Fig1b,c). The lactate/ (glucose consumption) ratio was higher for MOC1 and MC38 cells indicating more glycolytic activity in these cells than in B16ova cells (Fig. 2).

Under 24 hours hypoxic conditions (1% O_2) MOC1 and B16ova produced >2 fold higher amounts of lactate/cell than under normoxia. Hypoxia increased the lactate/(glucose consumption) ratio from 0.77 to 0.97 for MOC1 and from 0.44 to 0.78 for B16ova (Fig 3a, control). Applying complex 1 inhibitor IACS under normoxia increased the lactate concentration/cell in both cell lines by ~2. The lactate/(glucose consumption) ratio increased for MOC1 from 0.77 to 1.21 / 1.12 (0.1/1.0 µM IACS) and for B16ova from 0.44 to 0.84 / 0.99 (0.1/1.0 µM IACS), indicating enhanced glycolysis in both cell lines (Fig. 3a). This enhancement was most prominent in B16ova, which is in agreement with a more substantial increase of the % FDG uptake and extracellular acidification rate (Seahorse assay) of B16ova compared to MOC1 after IACS administration (Fig. 3b,c).

After injecting [6,6 $^2H_2$]glucose in a mouse the DMI spectra of the subcutaneously growing tumors clearly showed separate signals for HOD, glucose and lactate (Fig. 4a). DMI spectra of 8 µl voxels placed centrally in the tumors showed a much higher glucose uptake in MOC1 than in MC38 (Fig. 4b, c). However, the lactate levels increased to the same extent (~5 mM), suggesting that in vivo relatively more glucose carbons in MOC1 are consumed in oxidative metabolism. The increase in HOD was also much higher (to ~35 mM) in MOC1 than in MC38 (~20 mM). As the same mice types were used this confirms that MOC1 tumors have a more active tumor metabolism producing more HOD from [6,6 $^2H_2$]glucose.

Conclusion: This study reveals that DMS/DMI is able to assess differential glycolytic states of tumor types and thereby can sense OXPHOS inhibition, applied to reduce O_2 consumption.

References

Boreel ea. Clin Cancer Res 2021;27. doi: 10.1158/1078-0432.CCR-20-3913
Low ea .2023 Prog. NMR doi.org/10.1016/j.pnmrs.2023.02.002 0079-6565/
De Feyter ea. Sci Adv. 2018; 4 : eaat7314 Kreis ea. Radiology 2019; doi.org/10.1148/radiol.2019191242
Veltien ea. Cancers 2021, 13. doi.org/10.3390/cancers13164034

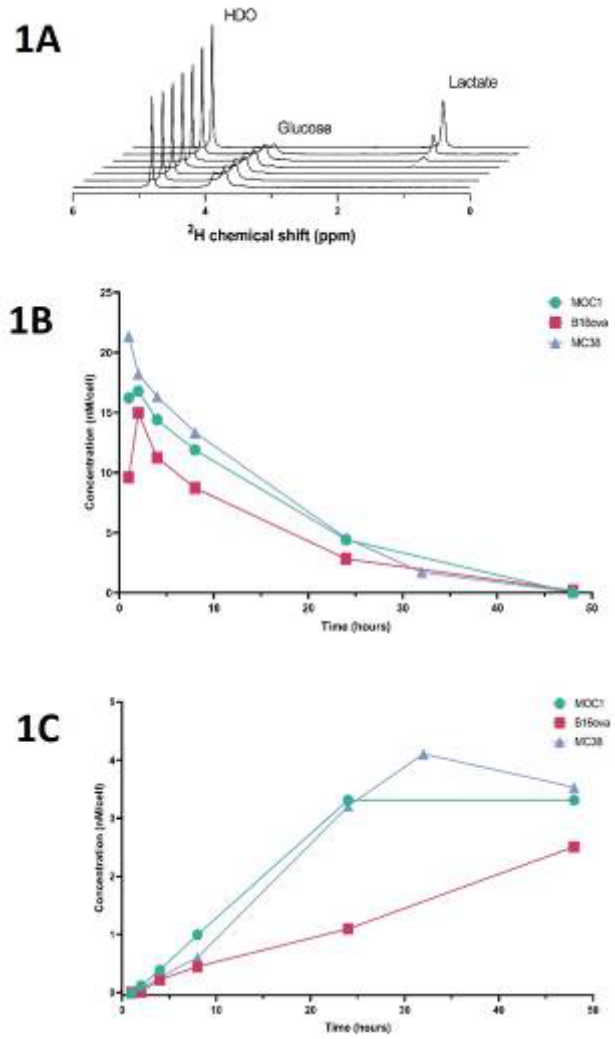

Figure 1.
a. ^{2}H MR spectra of medium of MOC1 cells vs incubation time (0, 1, 2, 4, 8, 24, 48 hrs) after D-[6,6"$^2H_2$]glucose addition.
b. [^{2}H glucose]/cell in medium vs incubation time.
c. Idem for [^{2}H lactate]/cell.

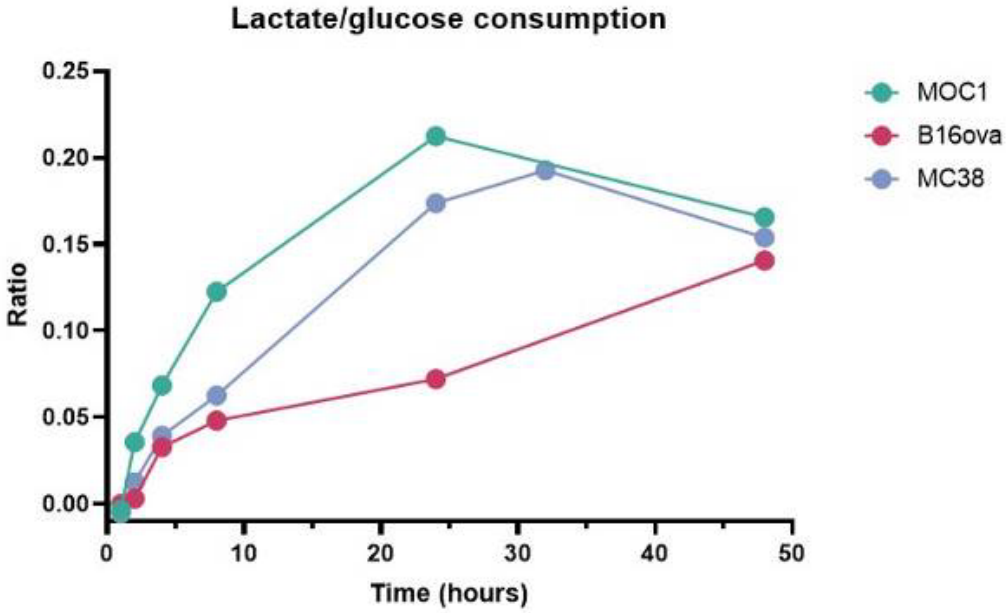

Figure 2. Lactate/(glucose consumption) ratio vs incubation time.

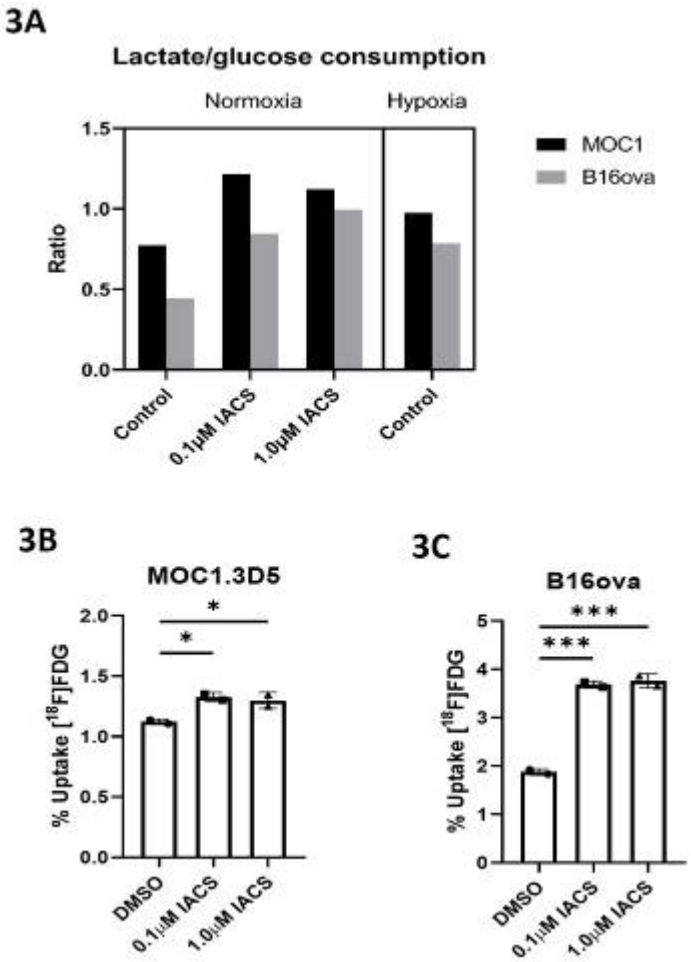

Figure 3.
a. Lactate/(glucose consumption) ratio 24 hours after D-[6,6"$^2H_2$]glucose addition to medium of MOC1 and B16ova under normoxia and with 0.1 and 1.0 μM IACS and under hypoxia (1% O_2).
b. Percentage uptake [^{18}F]FDG in MOC1 cells in medium without and with 0.1 and 1.0 μM IACS. FDG was applied for 2 hrs (37^{0}C).
c. Idem with B16ova cells.

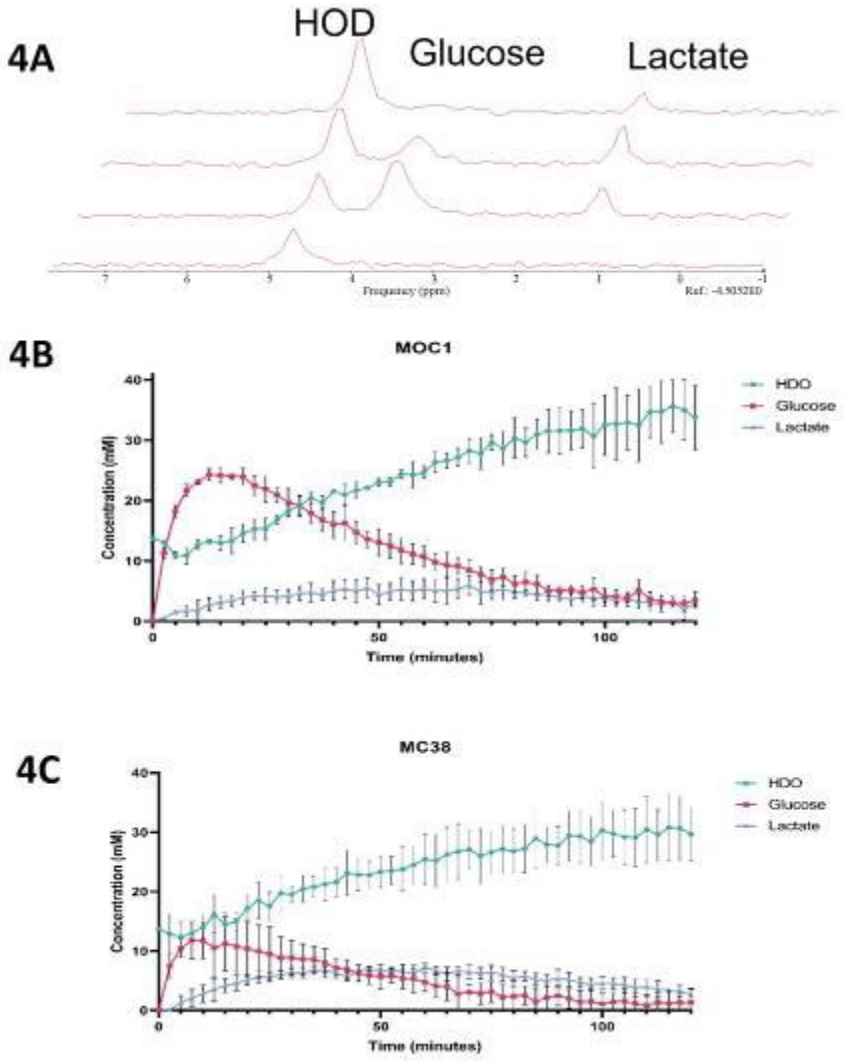

Figure 4.
a. ^{2}H MR spectra from a voxel in a subcutaneous MC38 tumor, at 0, 15, 52.5 and 115 min. after IV injection of D-[6,6"$^{2}H_{2}$]glucose.
b. Tumor tissue [^{2}H glucose], [^{2}H lactate] and HOD vs time after IV injection of D-[6,6"2H2]glucose in mice with subcutaneous MOC1 tumors.
c. Idem for MC38 tumors. N=3, error bars indicate SD for both tumors.

LB275.

Prediction of patient outcome in stroke patients based on radiomics features of super resolved ADC maps using enhanced deep residual networks

A. Samlı[1], E. Sümer[1], M. Şahin Erdoğan[1], H. Saybaşılı[1], E. Öztürk-Işık[1]

[1]Bogazici University, Biomedical Engineering Institute, Istanbul, Turkey

Introduction: Stroke presents a heterogenous group of vascular pathologies characterized by neurological deficits in the central nervous system, which is a major cause of disability and mortality [1]. Diffusion-weighted imaging (DWI) and the corresponding apparent diffusion coefficient (ADC) maps have emerged to be applicable in early diagnosis of stroke, with the highest sensitivity ranging from 73% to 92% within the first three hours and 95% to 100% within the first six hours after infarction [2,3]. Predicting long-term outcomes in the early stages of stroke improves the clinical decision-making, treatment planning, and surveillance [4]. Modified Rankin Scale (mRS) is used to predict patient outcome in stroke cases, and is essential for post-stroke treatment planning [5]. Radiomics is an emerging field that extracts quantitative and minable features from MRI [6]. Radiomics features obtained from high-resolution ADC maps have been shown to successfully predict mRS scores of stroke patients [7]. High-resolution MRI data might not always be available due to scan time considerations, and deep learning based super-resolution (DL-SR) algorithms have been proposed to increase image spatial resolution [8]. The purpose of this study was to generate super-resolved ADC maps using the Enhanced Deep Residual (EDSR) network [9], and evaluate their performance for predicting the mRS scores of stroke patients using radiomics features.

Methods: MRI data of 43 stroke patients, manual segmentation of their infarct lesions, and mRS scores were obtained from the publicly available ISLES 2017 dataset [10]. The stroke imaging protocol was performed on a 1.5T (Siemens Magnetom Avanto, Erlangen, Germany), or a 3T MRI scanner (Siemens Magnetom Trio, Erlangen, Germany), and included a DWI scan (TR=3,200 ms, TE=87 ms, 128x128x24, b=1000 s/mm²). The ADC maps were calculated from DWI using the scanner software. Ground truth ADC maps were down-sampled to half resolution using scikit-image package v0.19.2 [11]. Transfer learning was used to employ the EDSR network for single-image SR. Additionally, linear interpolation was used to upsample the ADC maps for performance comparison. The patient cohort was divided into two groups, patients managing their daily life without assistance (mRS<2, n=22) and those who required assistance (mRS>2, n=21). 1820 radiomics features of the infarct lesions, obtained from the SR, interpolated and ground truth ADC maps, were computed using PyRadiomics [12]. The most important radiomics features were selected using Least Absolute Shrinkage and Selection Operator (LASSO) [13]. Then, classical machine learning (ML) classifiers, including linear support vector classifier (SVC), logistic regression and multilayer perceptron (MLP), were used to predict mRS scores using the selected features. The ML algorithms were run 50 times with stratified train-test splits (80% training and 20% testing data) with different seed values and the average performances were reported. The peak signal to noise ratio (PSNR), structural similarity index (SSIM) and mean square error (MSE) metrics were compared between the SR and interpolated images.

Results: Figure 1 shows original, SR, interpolated and LR images of an example patient, which depicts better lesion definition on SR than interpolated images. MLP resulted in the highest accuracy for both original (0.95±0.06) and SR (0.82±0.13), while the performance dropped significantly when interpolated images were used (0.50±0.14) (Table 1). SR also resulted in better PSNR (31.29 vs 27.75) and SSIM (0.97 vs 0.92) and lower MSE than interpolation.

Discussion and Conclusion: EDSR network produced super-resolved ADC maps that were used to successfully predict the mRS scores of stroke patients based on the radiomics features of the infarct lesion. Despite a 10% decrease in classification accuracy compared to the ground truth, radiomics features extracted from the SR images achieved an 80% accuracy in predicting the mRS scores. On the other hand, the interpolated images did not lead to a successful prediction. Our findings suggest that when obtaining high-resolution images is not feasible, super-resolution images could be considered as a viable alternative. The effects of hyperparameter fine-tuning and domain adaptation of the EDSR network will be explored in future studies.

References

1. Sacco et al., Stroke 44, 7, 2013
2. Muir et al., Lancet Neurol 5, 9, 2006
3. Power et al., Stroke 46, 10, 2015
4. Nezu et al., J Atheroscler Thromb 29, 1, 2022
5. Broderick et al., Strok 48, 7, 2017
6. Gillies et al., Radiology 278, 2, 2016
7. Sahin et al., UKCI 2023
8. Kaur et al., J Imaging 7, 6, 2021
9. Lim et al., IEEE CVPRW 2017

10. Winzeck et al., Front Neurol 9, 2018
11. van der Walt et al., PeerJ
12. van Griethuysen et al., Cancer Res 77, 21, 2017
13. Tibsirani R, J R Stat Soc, B: Stat Methodol 58, 1, 1996

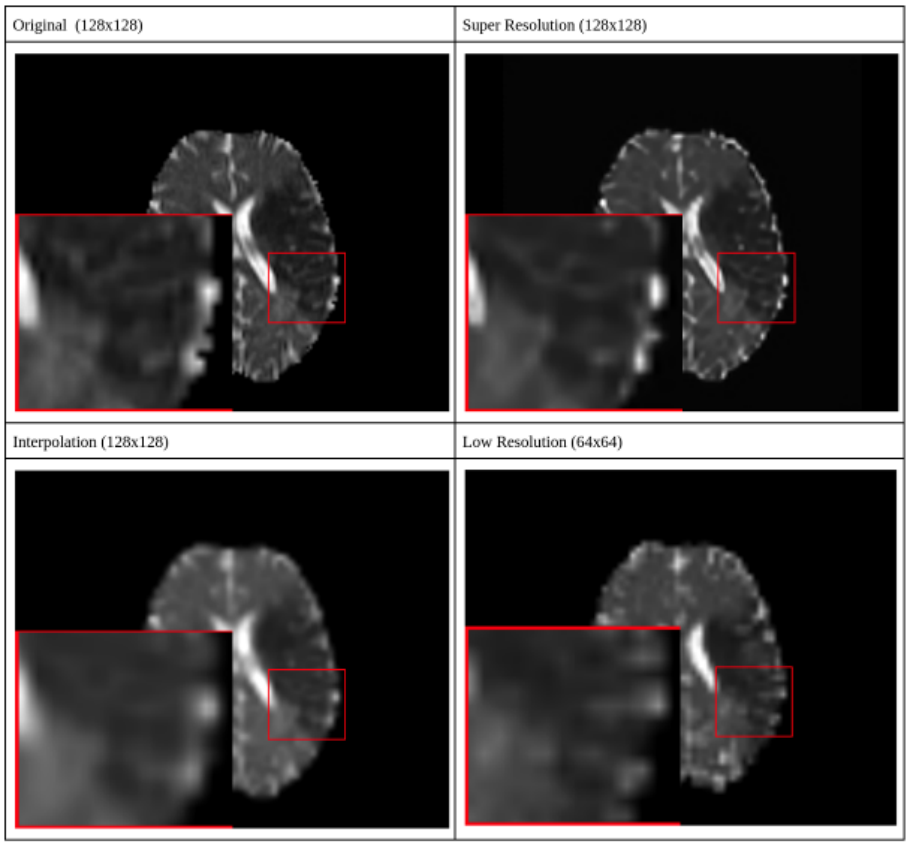

Figure 1. Original, SR, interpolated and LR ADC maps of an example stroke patient at a single slice that depicts the lesion boundaries well on the SR image.

	Original Images	Super Resolution	Interpolation
	Acc / Sens / Spec	Acc / Sens / Spec	Acc / Sens / Spec
MLP	0.95±0.07 / 0.95±0.11 / 0.95±0.10	0.82±0.12 / 0.82±0.17 / 0.82±0.17	0.42±0.16 / 0.30±0.25 / 0.52±0.31
Logistic Regr	0.94±0.07 / 0.93±0.11 / 0.95±0.10	0.79±0.15 / 0.81±0.21 / 0.77±0.19	0.47±0.15 / 0.37±0.24 / 0.55±0.25
Linear SVC	0.93±0.08 / 0.91±0.14 / 0.95±0.10	0.78±0.15 / 0.81±0.21 / 0.77±0.20	0.50±0.14 / 0.40±0.26 / 0.59±0.28

Table 1. The performance metrics of the mRS score classification using the radiomics features obtained from the original, super resolution and interpolated ADC maps.

	PSNR	SSIM	MSE
Super Resolution	31.29	0.97	2.1×10^{-4}
Interpolation	27.75	0.92	7.1×10^{-4}

Table 2. The PSNR, SSIM and MSE results for the super resolved and interpolated ADC maps with respect to the original images.

This work is supported by Bogazici University Research Fund (BAP) with grant number 19363

LB276.

Rapid multi-parametric relaxometry on a point-of-care 46 mT Halbach MRI scanner using balanced steady-state free precession imaging

F. Birk[1,2], C. Najac[3], T. O'Reilly[3], K. Scheffler[1,2], A. Webb[3], R. Heule[1,2,4]

[1]Max Planck Institute for Biological Cybernetics, High Field Magnetic Resonance, Tübingen, Germany
[2]University of Tübingen, Department of Biomedical Magnetic Resonance, Tübingen, Germany
[3]Leiden University Medical Center, C.J Gorter MRI Center, Department of Radiology, Leiden, Netherlands
[4]University Children's Hospital, Center for MR Research, Zurich, Switzerland

Introduction: Advances in low-field MRI (B_0<0.1T) empower the use of portable point-of-care (POC) systems as additional information source for the clinical routine and low-income countries[1,2]. Despite SNR limits and associated longer scan times, benefits like low-cost, smaller footprint, and safety promote new methods to increase the diagnostic value of low-field MRI worldwide[3]. Quantitative MRI potentially improves clinical certainty, but precise parameter estimation at low-field is hampered by long scan times[4]. The balanced steady-state free precession (bSSFP) sequence provides the highest SNR per unit time and mixed T2/T1 sensitivity[5], offering rapid multi-parametric relaxometry[6]. We investigate a frequency offset-cycled bSSFP sequence using our 46 mT POC MRI scanner for simultaneous T1 and T2 mapping in vitro. We further propose a procedure to mitigate and correct for B_0 drift on a Halbach low-field scanner.

Methods:

Data acquisition: Imaging was performed with an elliptical spiral-solenoid head coil on a portable 46 mT Halbach scanner[4,7] in a brain-like phantom[8] (WM/GM-like compartments with nominal reference values of T1≈215/250 ms and T2≈85/100 ms). Multi-shot 3D bSSFP data were acquired with 8, 10, or 12 frequency offsets (N_{off}) in the range (0, 1/TR) described by $v_{nom}(i)=(1/(TR*2*N_{off}))*(2*i-1)$ with $i=1,2,\ldots,N_{off}$, a resolution of 2.5x2.5x5 mm^3, a TR/TE of 14/7 ms, and a flip angle (FA) of 30°. The k-space was sampled using zig-zag phase-encoding. Each 3D acquisition was segmented into multiple shots. For each shot, all offsets were acquired sequentially within <1 min. A frequency adjustment was performed in-between shots to reduce the impact of drift.

Drift correction: The total drift $v_{drift,tot}$ per shot during N_{off} acquisitions was estimated visually using the 2π periodicity of the bSSFP frequency profile. This initial guess was refined iteratively using a step size of 0.2 Hz. Step 1: The incremental drift $v_{drift,incr}(i)=v_{drift,tot}/N_{off}*(i-1),\ i=1,2,\ldots,N_{off},$ was added to the nominal frequency vector $v_{new}(i)=v_{nom}(i)+v_{drift,incr}(i)$. Step 2: The acquired complex data was interpolated voxelwise from v_{new} to v_{nom}.

Quantitative mapping: The lowest order SSFP configurations (F_{-1}, F_0, F_1) were calculated via a Fourier transform of the drift corrected complex bSSFP data, employing 8, 10, or 12 offsets[6]. The SSFP configurations (magnitude) were denoised[9] and unringed[10,11] prior to quantitative mapping. Based on prior B_1^+ analysis, it was assumed that the actual FA equals the nominal FA (B_1^+=1.0). Iterative fitting using a golden section search allowed voxelwise estimation of T1 and T2[6,12].

Results: Figure 1 shows bSSFP magnitudes, maximum intensity projection (MIP), and F_{-1}, F_0, and F_1 for a representative axial slice. Residual banding-like artifacts in the SSFP configurations and MIP image remain without drift correction. Figure 2 shows the simulated impact of frequency drift ($v_{drift,tot}$) on the SSFP configurations, expressed as percentage error relative to the ideal non-drifted configurations[13] for a range of $v_{drift,tot}$ and local off-resonances (ΔB_0). All configurations are strongly affected by frequency drift, emphasizing the need for drift reduction (multi-shot acquisition with frequency adjustments) and correction (postprocessing). The error along ΔB_0 repeats periodically since 2 x 1/TR is covered. The two main drift correction steps are shown in Figure 3. The interpolation to the nominal offsets (step 2) further reduces artifacts, especially in F_{-1} (orange arrows). The F_1 mode is most prone to image artifacts, affecting the T1 and T2 maps in Figure 4. The T2 maps in Figure 4 appear robust whereas the T1 estimates for the WM- and GM-like compartments using 8 offsets are lower compared to 10 or 12 offsets. The boundaries between CSF-like and tissue-like compartments are well preserved.

Discussion: Low-field MRI holds potential for non-invasive imaging and clinical applications. The high SNR of bSSFP is advantageous, especially since the T2/T1 ratio increases at lower fields, enhancing SNR efficiency. However, the high frequency sensitivity could limit the use of bSSFP at low-field. Our work demonstrates the feasibility of multi-parametric mapping at 46 mT using frequency offset-cycled bSSFP and a sophisticated drift correction strategy.

Conclusion: Simultaneous multi-parametric relaxometry was achieved in vitro on a 46 mT Halbach MRI scanner using frequency offset-cycled bSSFP data. The effects of B_0 drift were simulated and a drift correction method for the bSSFP data was proposed.

References

[1]Marques et al., MRM (2019)
[2]Sarracanie et al., Front Phys. (2020)
[3]Arnold et al., MRM (2023)
[4]O"Reilly et al., MRM (2022)
[5]Scheffler et al., Eur Radiol. (2003)
[6]Nguyen et al., MRM (2017)
[7]O"Reilly et al., MRM (2021)
[8]Najac et al., ISMRM #1587 (2023)
[9]Maggioni et al., IEEE (2013)
[10]Kellner et al., MRM (2016)
[11]Neto Henriques, (2017)
[12]Heule et al., MRM (2014)
[13]Hänicke et al., MRM (2003)

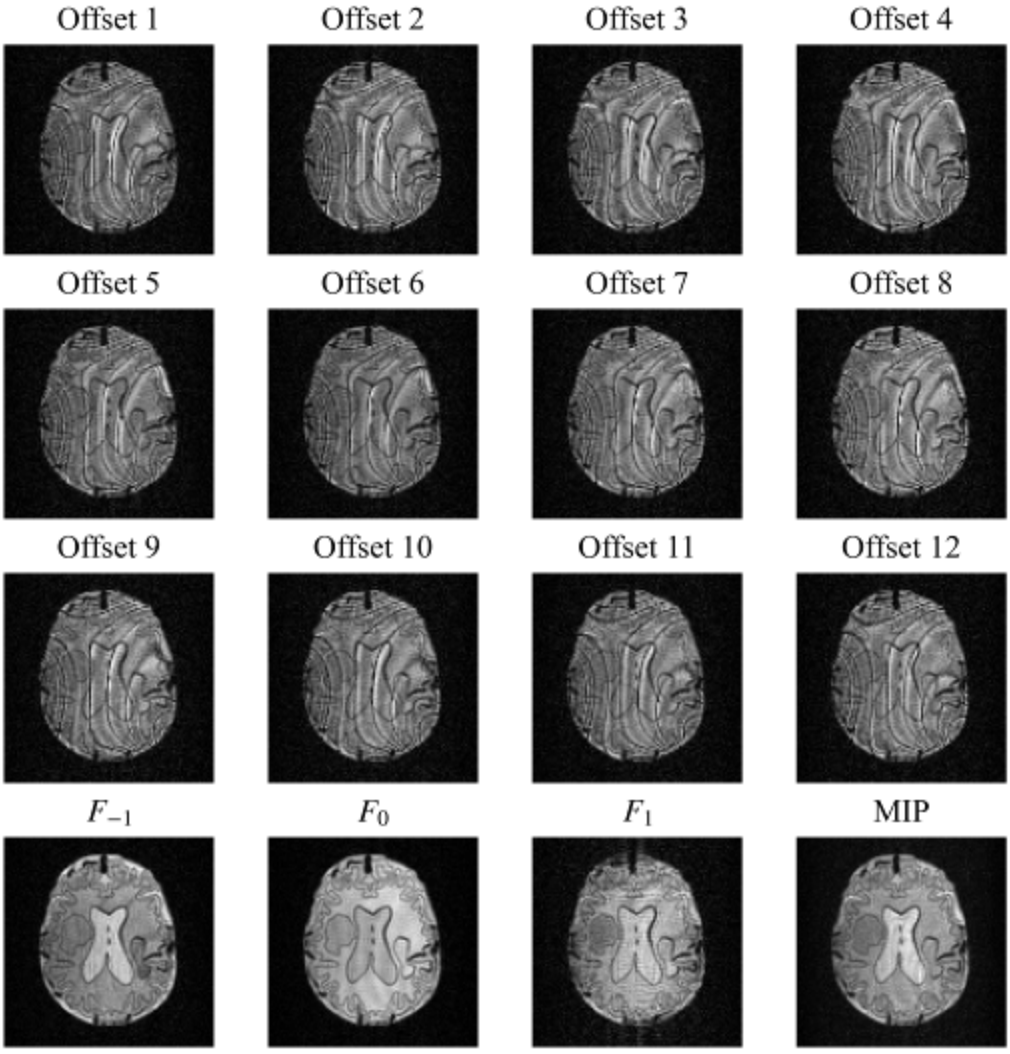

Fig. 1 bSSFP data acquired at 12 equidistant frequency offsets (FA of 30°), the three lowest-order SSFP configurations, and the MIP across all offsets for a representative axial slice.

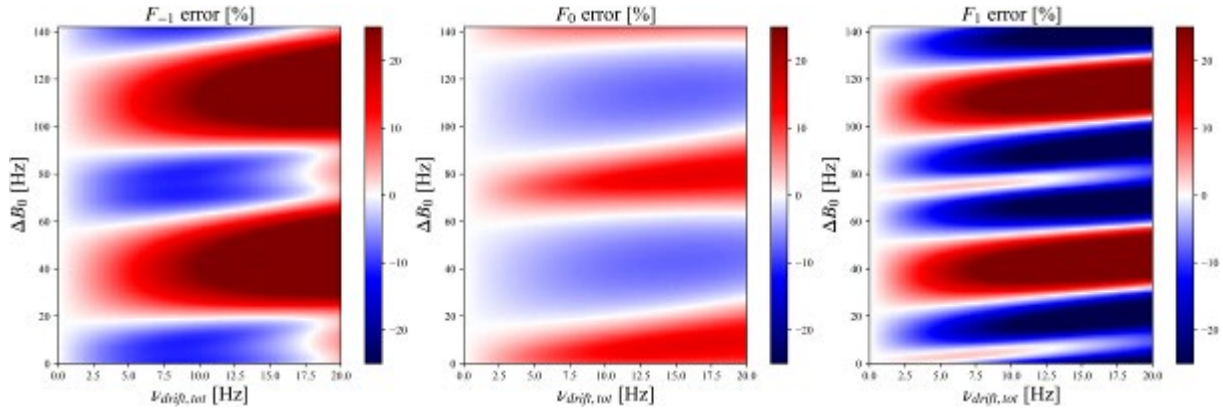

Fig. 2 Simulated relative deviation (%) between ideal[13] and drifted SSFP configurations calculated from 12-point frequency offset-cycled bSSFP data for a range of drifts ($v_{drift,tot}$) and off-resonances (ΔB_0). TR/TE: 14/7 ms, FA=30°, T1=300 ms, T2=100 ms. Red implies underestimation, blue overestimation relative to the ideal configurations.

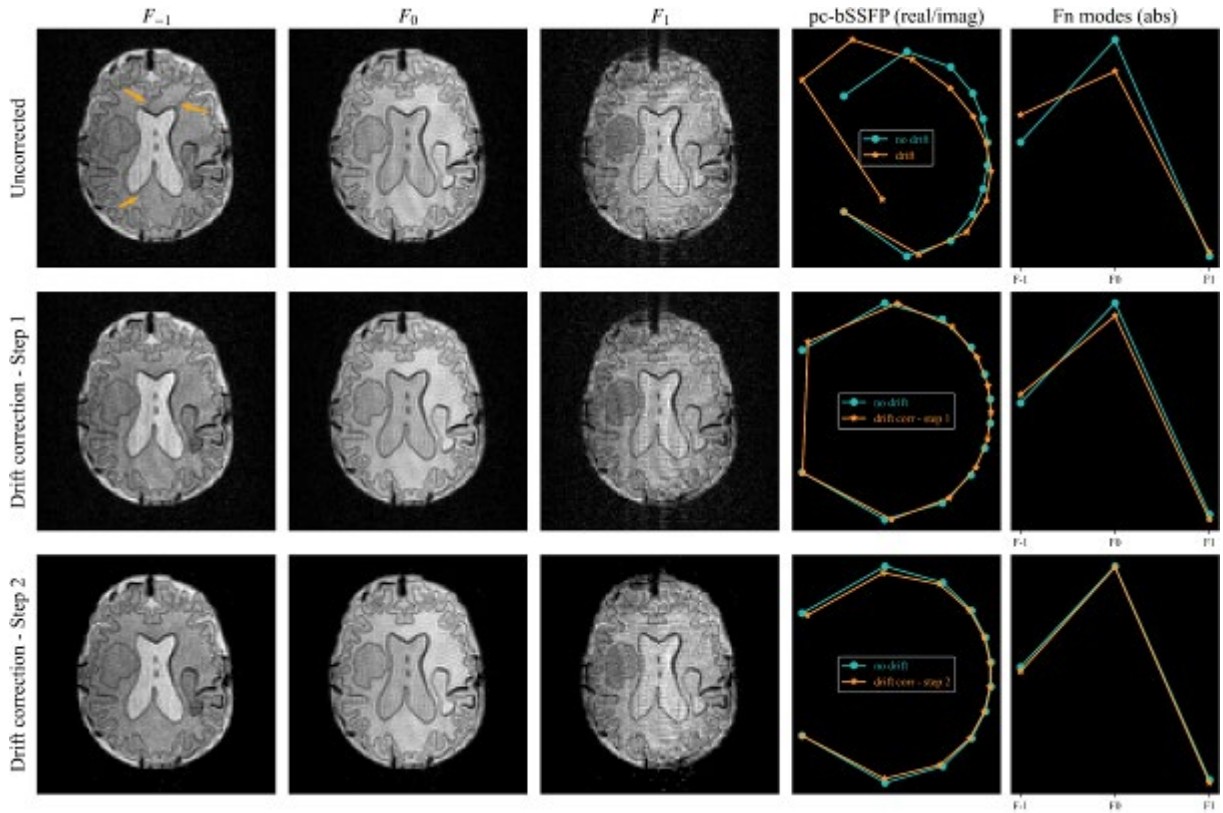

Fig. 3 The two main drift correction steps for in vitro (columns 1-3) and in silico (columns 4+5) data. The total drift estimated for in vitro data was 6 Hz and also used for the simulation (TR/TE:14/7ms, FA=30°, T1=300ms, T2=100ms). Orange arrows display the artifacts mitigated during the correction process.

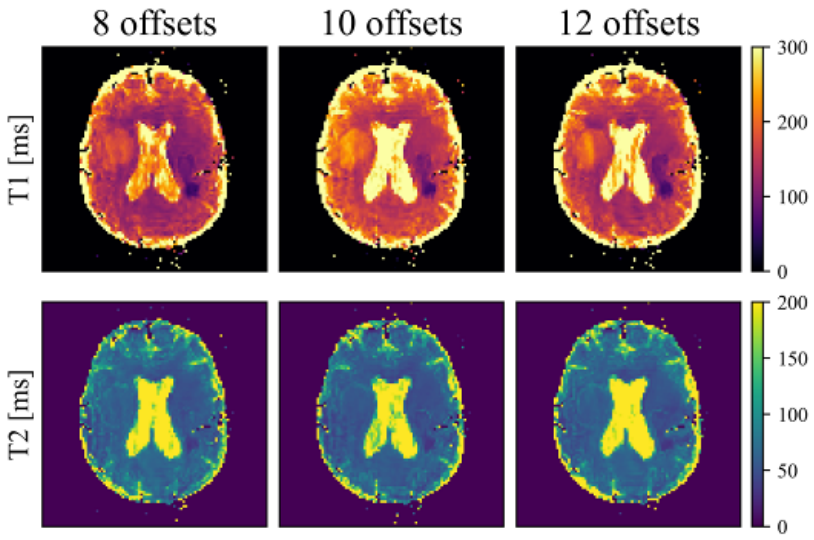

Fig. 4 T1 and T2 maps obtained from 8, 10, and 12-point frequency offset-cycled bSSFP data are shown for a representative axial slice.

LB277.

T2 mapping with GRAPPATINI in temporal lobe epilepsy improves epileptogenic zone characterization: a pilot study

M. C. Bonacci[1], M. E. Caligiuri[1], I. Sammarra[2], T. Kober[3], D. Zacà[4], F. Fortunato[2], A. Gambardella[2]

[1]University Magna Graecia of Catanzaro, Department of Medical and Surgical Science, Catanzaro, Italy
[2]University Magna Graecia, Institute of Neurology, Department of Medical and Surgical Sciences, Catanzaro, Italy
[3]Lausanne University Hospital and University of Lausanne, Department of Radiology, Lausanne, Switzerland
[4]Siemens Healthcare, Milan, Italy

Introduction: Temporal lobe epilepsy (TLE) is characterized by seizures originating from the mesial or lateral temporal lobe. Quantitative MRI (qMRI) techniques, such as quantitative T2 mapping, measure intrinsic properties of brain tissue, and thus may represent a useful addition to the standardized assessment of MRI in epilepsy patients.In this study we have analyzed T2 maps of 10 patients with TLE using GRAPPATINI, an accelerated T2 mapping technique used to calculate T2 relaxation times of a certain tissue and display them voxel-wise on a parametric map.

Methods: Ten patients with TLE (3 M, 7F; age: 45,6±17,35), diagnosed by EEG and apparently negative to standard MRI alterations, were scanned on a 3T PET-MR Biograph mMR (Siemens Healthineers). The protocol comprised standard HARNESS acquisition optimized for epilepsy patients[1] and a T2 relaxometry sequence (GRAPPATINI[2], TR=4s, 16 echos, 0:174.4ms, spaced by 10.9 ms; Resolution: 0.45 x 0.45 x 4 mm3).T2 mapping acquisition and reconstruction were performed using a vendor-supplied package (WIP #899C), based on a multi-contrast spin-echo sequence and enabled to perform the blocked undersampling pattern which is optimized for the employed iterative reconstruction technique. Reconstruction is started by calculating an initial guess of the M0 image and the T2 map. Subsequently, the signal model is applied to calculate simulated image data for all scanned TEs, i.e. a set of estimated T2 contrast images. These images are Fourier-transformed. In order to compare only k-space points which were actually sampled, the resulting estimated k-spaces are multiplied by a binary mask representing the employed block-sampling scheme ("artificial subsampling"). Subsequently, the difference between the actually measured data and the estimated k-space data are calculated. The l2-norm of this residual k-space yields a cost value. Having this cost value, the algorithm checks whether the error between its estimation and the measured data meets a fixed termination criterion. If the criterion is not met, the iterative reconstruction tries to improve the M0 and T2 estimations. To this end, a CG descent optimizer is used, which needs the derivative maps for all fitted parameters. For each patient, we processed the T1 images with Freesurfer, to obtain segmentations of grey and white matter and of the bilateral hippocampi. Afterwards, using FSL, the simulated image for TE=80s was used to calculate the linear transform to the individual structural space. This transform was then applied to the T2map. Finally, we calculated histograms of T2 value distributions in the following regions: whole-brain, hippocampus, temporal lobe GM and WM. Regions were classified as ipsi-lateral or contra-lateral to EEG seizure focus. Histograms were calculated after masking out CSF voxels, to avoid contamination of high signal values. Normalization and graphical representation of the histograms were performed using an in-house script in matlab: for each patient and each ROI, we compared the individual histogram towards the first quartile, second quartile (median) and third quartile of the cohort distribution of T2 values.

Results: Out of ten patients, 5 had a clear epileptogenic side on the EEG, 1 had bilateral electrophysiological abnormalities, and 1 had conflicting evidence of hippocampal sclerosis (Hs) between two expert raters.Interestingly, distribution of T2 values in the temporal region (either whole temporal GM, hippocampus or both) was altered in agreement with the epileptogenic side. Fig.1 shows the T2 distributions in left and right hippocampi of a patient with left EEG abnormalities. It can be observed how the peak position of the histogram is shifted towards higher T2 values in the ipsilateral side (Left peak = 55.5 ms; Right peak = 50.6 ms). Fig.2 shows the doubt Hs case, highlighting how the histogram parameters for the ipsilateral hippocampus were all severely affected. Of note, Hs and EEG side coincided in this case.

Discussion and Conclusion: T2 relaxometry might be a promising tool for a better and non-invasive lateralization of the epileptogenic zone, as well as for identifying lesions that are not visible on standard MRI**.** Quantification of epilepsy-related abnormalities using qMRI can improve the identification of optimal candidates for both surgical treatment of the epileptogenic zone and/or testing of anti-epileptic drugs.

References: (1) Bernasconi A, Cendes F, Theodore WH, Gill RS, Koepp MJ, Hogan RE, Jackson GD, Federico P, Labate A, Vaudano AE, Blümcke I, Ryvlin P, Bernasconi N. Recommendations for the use of structural magnetic resonance imaging in the care of patients with epilepsy: A consensus report from the International League Against Epilepsy Neuroimaging Task Force. Epilepsia. 2019 Jun;60(6):1054-1068. doi: 10.1111/epi.15612. Epub 2019 May 28. PMID: 31135062. (2) Hilbert, T et al. "MARTINI and GRAPPA – When Speed is Taste." Proc Int Soc Magn Reson Med. Milan, Italy(2014).

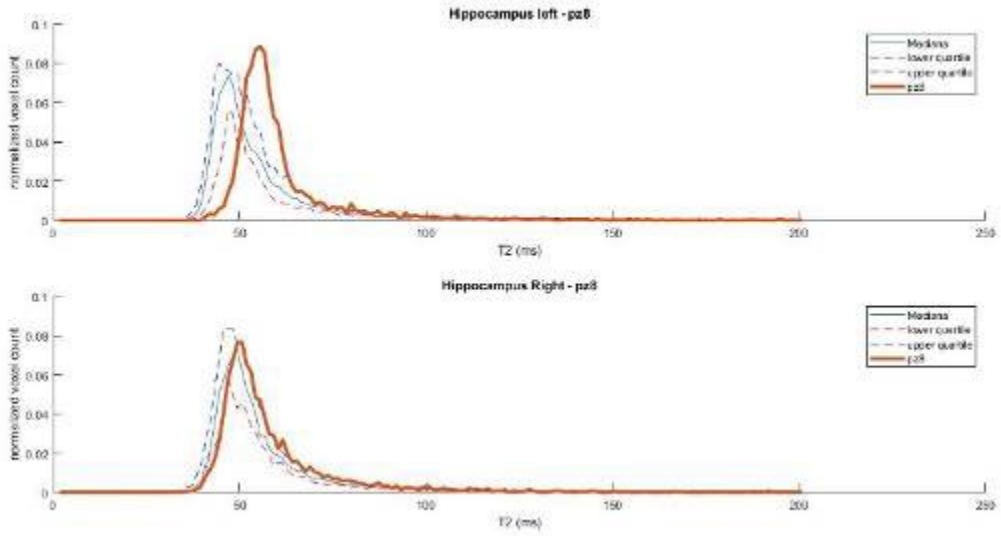

Fig.1. Distributions of T2 values in left and right hippocampi of a patient with left EEG abnormalities.

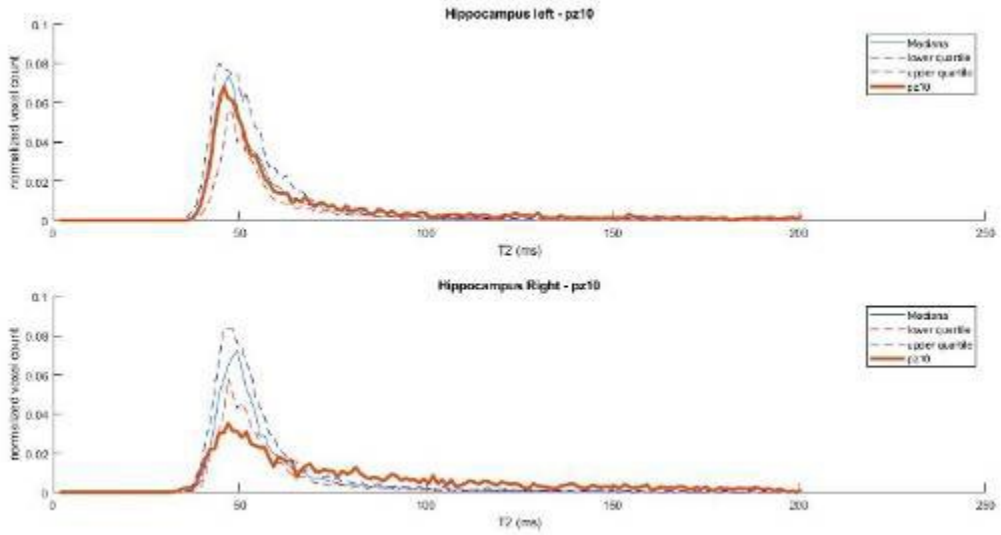

Fig.2. Distribution of T2 values in the ipsilateral hippocampus of a patient with doubt hippocampal sclerosis case.

LB278.

T2 mapping with GRAPPATINI for the characterization of adult-onset and juvenile-onset Huntington Disease

M. E. Caligiuri[1], M. C. Bonacci[2], T. Kober[3], D. Zacà[4], U. Sabatini[5], F. Squitieri[6], A. Quattrone[7]

[1]University Magna Graecia, Neuroscience Research Center, Department of Medical and Surgical Sciences, Catanzaro, Italy
[2]University Magna Graecia of Catanzaro, Department of Medical and Surgical Science, Catanzaro, Italy
[3]Lausanne University Hospital and University of Lausanne, Department of Radiology, Lausanne, Switzerland
[4]Siemens Healthcare,, Milan, Italy
[5]University Magna Graecia, Institute of Neuroradiology, Department of Medical and Surgical Sciences, Catanzaro, Italy
[6]Huntington and Rare Diseases Unit, Fondazione IRCCS Casa Sollievo della Sofferenza Hospital, Viale Cappuccini, San Giovanni Rotondo, Italy
[7]University Magna Graecia, Institute of Neurology, Department of Medical and Surgical Sciences, Catanzaro, Italy

Introduction: Juvenile-onset Huntington"s disease (joHD, neurological onset ≤ 20 years) is a rare HD variant associated with large CAG repeat-size alleles (> 60), which shows different clinical features from adult-onset HD, and typically progresses more rapidly.(1) For these reasons, it is crucial to monitor and characterize patterns of disease progression in joHD and compare them to the more studied adult form. Quantitative MRI (qMRI) techniques, which measure intrinsic properties of brain tissue, may provide further insight regarding the changes that differentially underlie the two forms of HD. In this study we have analyzed T2 maps of 14 patients with HD (12 with adult-onset HD, 2 with joHD) using GRAPPATINI, an accelerated T2 mapping technique used to calculate T2 relaxation times of a brain tissue and display them voxel-wise on a parametric map.

Methods: Fourteen patients with HD (12 adult-onsetHD 8M/4F, age: 44.1±10.5; 2 joHD, 2F, 22 and 24 yo), underwent an hybrid acquisition on a 3T PET-MR Biograph mMR (Siemens Healthcare). The protocol comprised, among other MRI sequences and FDG-PET, a T2 relaxometry sequence (GRAPPATINI (2), TR=4s, 5 undersampling blocks, 16 echos, 0:174.4ms, spaced by 10.9 ms; Resolution: 0.45 x 0.45 x 4 mm3). T2 mapping acquisition and reconstruction were performed using a vendor-supplied package (WIP #899C), based on a multi-contrast spin-echo sequence. The WIP applies an iterative reconstruction procedure that allows to obtain T2 maps directly on the scanner, with a very convenient acquisition time (~3 minutes). In particular, a block-sampling scheme is employed to split the k-space in N blocks, one per echo time. At each TE, only one block is sampled, meaning that the k-space center is sampled once in N echo times. As an empirical result, it is suggested that improved results are obtained by sampling the center at least 3 times (3*N+1 echoes should be sampled - here we had 5 undersampling blocks and 16 echos). During offline post-processing, we processed the 3D T1-weighted images (ADNI-style MPRAGE) with Freesurfer, to obtain segmentations of gray and white matter and of the bilateral striatum (putamen + caudate). The striatal region of interest was chosen since it is a crucial site for HD-related abnormalities, usually detected earlier and in larger measure in joHD rather than HD. Afterwards, using FSL, a simulated TE=80s image (output of the WIP package, with more anatomical detail) was used to calculate the linear transform to the individual structural space. This transform was then applied to the T2map. Finally, we calculated histograms of T2 value distributions in left and right caudate nucleus and putamen. Histograms were calculated after masking out CSF voxels, to avoid contamination of high signal values. Normalization and graphical representation of the histograms were performed using an in-house script in matlab: for each patient and each ROI, we compared the individual histogram towards the first quartile, second quartile (median) and third quartile of the cohort distribution of T2 values.

Results: The distributions of T2 values in the striatal regions greatly differed between adult-onset and joHD (Figures 1 & 2 show caudate distribution for the two joHD patients, Figures 3 & 4 show the putaminal distributions). In particular, the median shape of the distribution in the adult cohort was indeed different from the expected T2 distribution in healthy tissue, as reported in literature, but at least it was centered on plausible T2 values for GM structures (~ 50 ms). On the contrary, the histograms derived from the two joHD patients were more narrow but completely shifted towards higher T2 values, suggesting that the processes of striatal degeneration in this subtype of HD are greatly accelerated compared to the adult form (of note: the joHD patients have half the age of most adultHD). Furthermore, we also found evidence of asymmetric damage between the two hemispheres, in both structures and for both patients.

Discussion and Conclusion:T2 relaxometry, and qMRI techniques in general, might provide great benefits to the field of HD research. In particular, they might provide additional information, complementary to what is already known from post-mortem histopathology in these rare (and rarest, in case of joHD) patients. Earlier and better characterization of disease status and progression might help to better identify optimal candidates for novel trials of newly developed drugs.

References: (1) Fusilli, C.; Migliore, S.; Mazza, T.; et al. Biological and clinical manifestations of juvenile Huntington"s disease: a retrospective analysis. Lancet Neuro 2018, 17.11, 986-993. **(2)** Hilbert, T et al. "MARTINI and GRAPPA – When Speed is Taste." Proc Int Soc Magn Reson Med. Milan, Italy(2014).

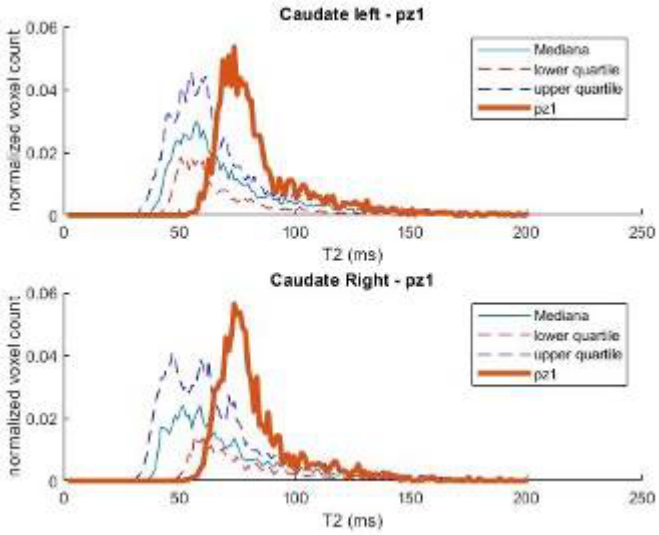

Figure 1: Caudate T2 distribution for a HDstage 3 patient with joHD (bold line) compared to the median and IQR distribution of the adult HD patients.

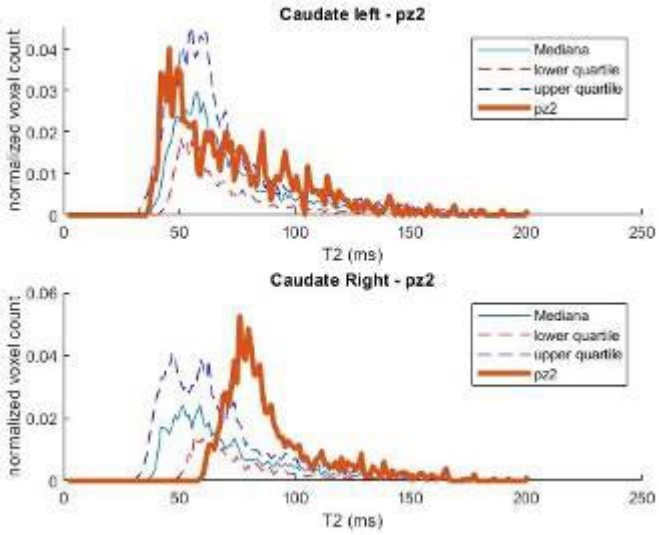

Figure 2: Caudate T2 distribution for a HDstage 2 patient with joHD (bold line) compared to the median and IQR distribution of the adult HD patients.

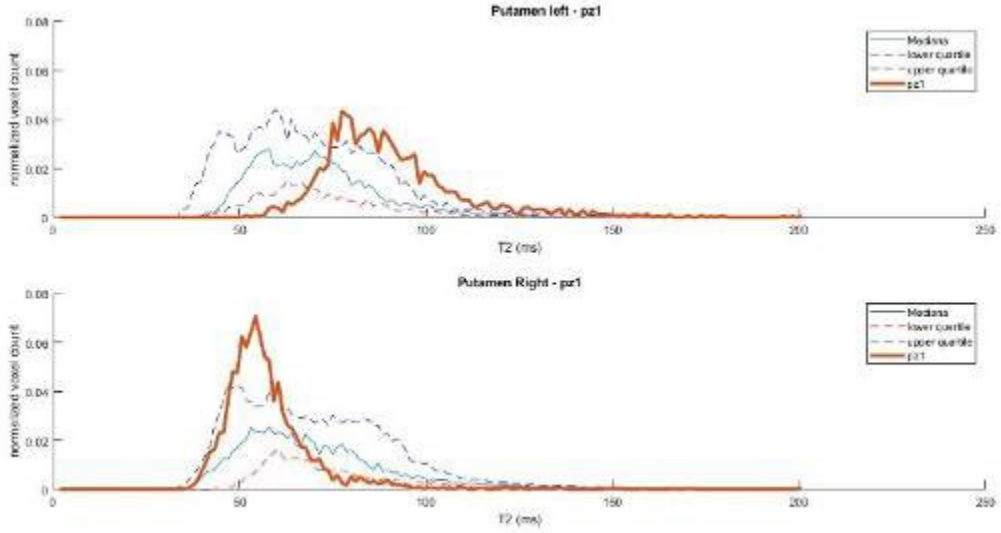

Figure 3: Putaminal T2 distribution for a stage 3 patient with joHD (bold line) compared to the median and IQR distribution of the adult HD patients.

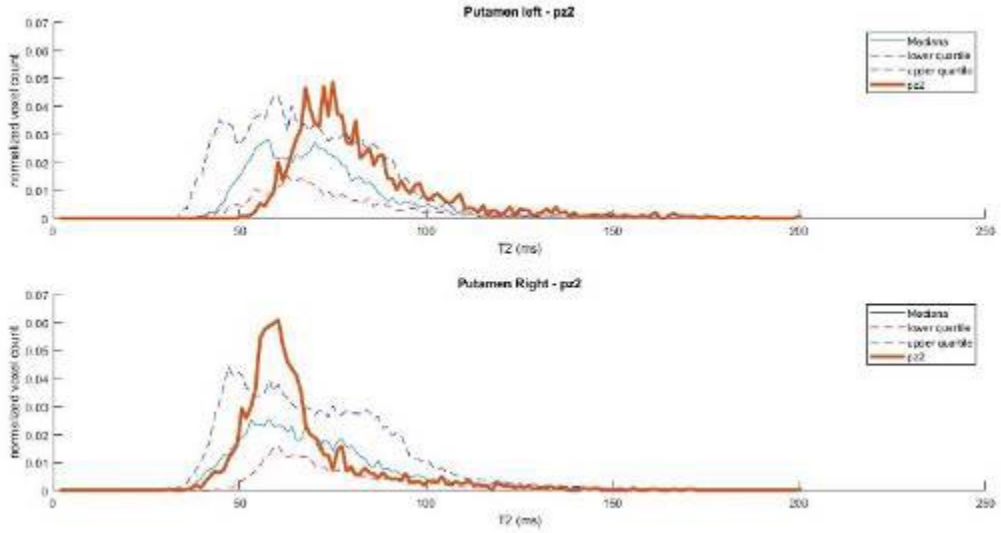

Figure 4: Putaminal T2 distribution for a stage 2 patient with joHD (bold line) compared to the median and IQR distribution of the adult HD patients.

LB279.

7T MRI exploration of cortical atrophy of Type 2 Diabetes Mellitus and metabolic syndrome patients from the Maastricht Study

K. Liu[1], R. Haast[2], K. Uludağ[3], H. Smeets[4], J. Jansen[5], E. Formisano[1], B. A. Poser[1], D. Ivanov[1]

[1]Maastricht University, Maastricht Brain Imaging Centre, Maastricht, Netherlands
[2]Aix-Marseille University, The Center for Magnetic Resonance in Biology and Medicine, Marseille, France
[3]University of Toronto, Department of Medical Biophysics, Toronto, Canada
[4]Maastricht University, Department of Genetics and Cell Biology, Maastricht, Netherlands
[5]Maastricht University, Department of Radiology, Maastricht, Netherlands

Introduction: Type 2 Diabetes Mellitus (T2DM), characterized by relative insulin deficiency and insulin resistance increasing with age [1], induces complex alterations in metabolism and impacts target organs progressively. Accompanying abnormalities often commence before the clinical presentation with T2DM. The cluster of the following risk factors: abdominal obesity, hypertension, dyslipidemia, and impaired fasting glucose, referred to as the metabolic syndrome (MetS), is often considered as a pre-diabetic condition [2]. Macrostructural imaging using conventional 1.5T and 3T MRI showed accelerated loss of brain volume due to T2DM, compared to normal aging [3]. Scanning at 7T enables high spatial resolution quantitative mapping which provides helpful information with regards to brain abnormalities. We aim to explore cortical morphology between groups (from controls to MetS to T2DM patients) that differ in their metabolic and hemodynamic health status.

Methods: 133 participants (40-75 yrs.) were grouped into: controls (C, N = 45), MetS (MS, N = 44) or T2DM patients (DM, N = 44) [4]. T2DM was diagnosed in case the participant was using diabetes medication or had a fasting plasma glucose (FPG) level ≥ 7.0mmol/L and/or a 2-h blood glucose ≥ 11.1mmol/L after an oral glucose tolerance test. All participants within the T2DM group were diagnosed with T2DM and a minimum of 2 MetS criteria; ones without T2DM but 3 or more MetS criteria entered the MetS group, controls had 2 of the 5 MetS criteria. MR data were acquired using a whole-body Siemens 7T scanner and a 32-channel Nova head coil. Dielectric pads were placed proximal to the temporal lobe area to locally increase the transmit B_1^+ field. 0.7mm isotropic resolution whole-brain quantitative T1 map was obtained using MP2RAGE [5], which was corrected by a 2mm isotropic B_1^+ map obtained with the Sa2RAGE [6] sequence. Skull-stripping, masking, and non-brain tissue removal were performed using FSL, MATLAB and PreSurfer. The skull-stripped and gradient-distortion-unwrapped MP2RAGE UNI volume was aligned using affine transformation to the MNI space template. FastSurfer was used for surface-based morphological reconstruction, all surface metrics were registered to the average using sphere-based alignment and smoothed with 10mm kernel. A whole-brain vertex-wise comparison of volume and thickness between groups were performed, a post-hoc cluster correction was conducted with $P < 0.05$ for each test. A second analysis with glycated hemoglobulin (HbA1c) and pulse pressure (PP) [7, 8] as covariates was performed to see whether some regions are more vulnerable to poorly controlled blood sugar level or instable hemodynamics, followed by cluster correction as well. Then regions occurrence was reckoned. Aware of potentially high false positive rate, only regions occurring more than 3 times entered the next stage. To eliminate the nuisance effects, a linear regression was performed for region volume with age, sex and estimated intracranial volume, saving the standardized residual. Similar regression was performed on cortical thickness with age and sex. Residuals went through stepwise linear regression with BMI, waist circumference, blood pressure, blood lipids, FPG and HbA1c as predictive variables [9].

Results: Figures and table illustrate the regions which showed statistical significance (yellow < 0.05, blue < 0.001) in either group analysis (Fig. 1) or correlation analysis (Fig. 2). Gray matter loss was distributed mainly in superior frontal, rostral middle frontal, posterior cingulate and lingual regions (Tab. 1). Superior frontal thickness and volume were entered in stepwise linear regression. Only HbA1c remained in the final model, and the adjusted R^2 was 0.043 ($P = 0.01$).

Discussion & Conclusion: Our research confirmed, at higher resolution, the cortical atrophy and heterogeneity of its distribution found by previous literature [10], validating quantitative MRI as a useful tool to identify multiparameter signatures of the clusters we found. To fully discover risk factors for these brain changes, further studies with additional imaging parameters and advanced statistical methods will be performed.

References

1. Fu, Z., et al., Curr Diabetes Rev, 2013. 9(1): p. 25-53.
2. Ford, E.S., et al., J Am Coll Cardiol, 2010. 55(13): p. 1310-7.
3. Falvey, C.M., et al., Diabetes Care, 2013. 36(3): p. 677-82.
4. Schram, M.T., et al., Eur J Epidemiol, 2014. 29(6): p. 439-51.
5. Marques, J.P., et al., Neuroimage, 2010. 49(2): p. 1271-81.

6. Eggenschwiler, F., et al., Magn Reson Med, 2012. 67(6): p. 1609-19.
7. de Bresser, J., et al., Diabetes Care, 2010. 33(6): p. 1309-14.
8. Gami, A.S., et al., J Am Coll Cardiol, 2007. 49(4): p. 403-14.
9. Petersen, M., et al., bioRxiv, 2023: p. 2023.02.22.529531.
10. Brundel, M., et al., J Neurol Sci, 2010. 299(1-2): p. 126-30.

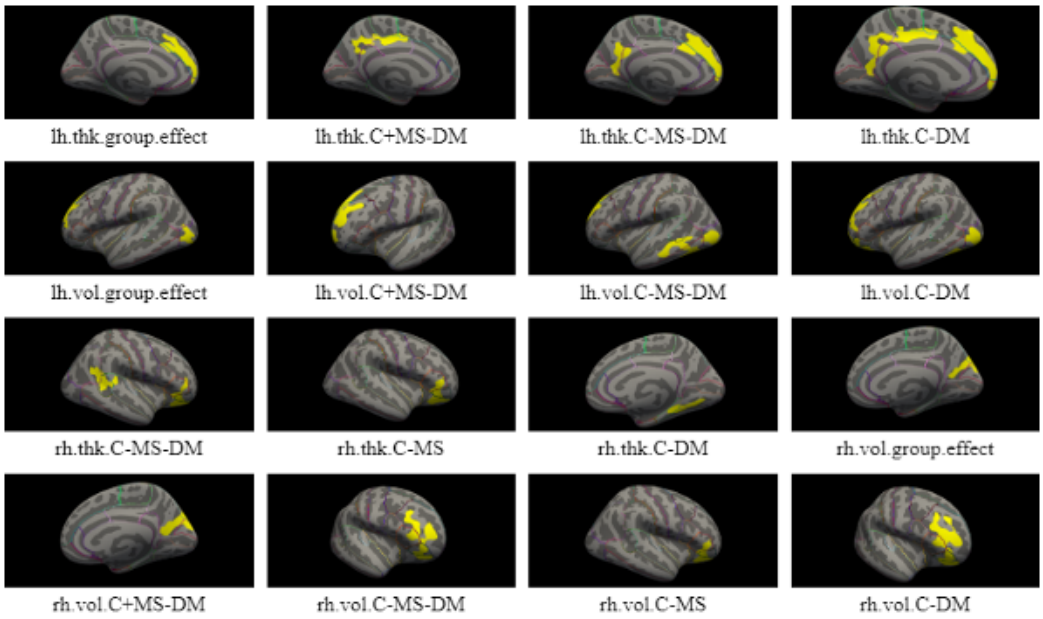

Fig. 1 Group analysis between control (C), metabolic syndrome (MS) and type 2 diabetes mellitus (DM), yellow showing clusteral significance less than 0.05.

Fig. 1 Group analysis
lh = left hemisphere, rh = right hemisphere
thk = thickness, vol = volume
group.effect = compared between control, MetS and T2DM
C+MS-DM = average of control and Met compared with T2DM
C-MS-DM = control compared with average of MetS and T2DM
C-MS = control compared with MetS
C-DM = control compared with T2DM
MS-DM = MetS compared with T2DM

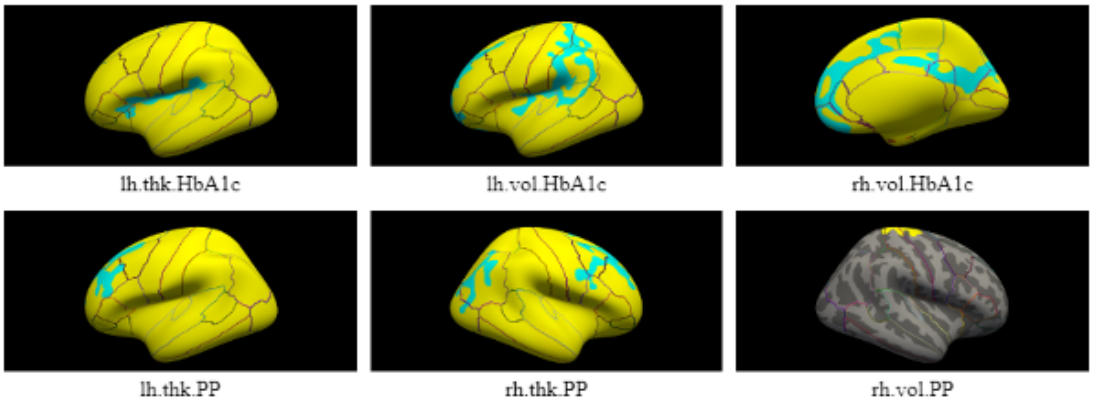

Fig. 2 Correlation analysis with glycated hemoglobin (HbA1c) and pulse pressure (PP), yellow and blue showing clusteral significance less than 0.05 and 0.001, respectively.

Fig. 2 Correlation analysis

lh = left hemisphere, rh = right hemisphere
thk = thickness, vol = volume
HbA1c = correlation with glycated hemoglobin
PP = correlation with pulse pressure

Tab. 1 Regions which showed statistical significance in the analysis

		Left Hemisphere Thickness	Left Hemisphere Volume	Right Hemisphere Thickness	Right Hemisphere Volume
Group Analysis	Group effect	Superior-frontal	Superior-frontal		Superior-parietal
			Lateral-occipital		
	HC+MS-DM	Posterior-cingulate	Superior-frontal		Superior-parietal
	HC-MS-DM	Superior-frontal	Rostral-middle-frontal	Lateralor-bitofrontal	Rostral-middle-frontal
		Precuneus	Inferior-temporal	Bankssts	Lingual
		Rostral-middle-frontal	Lateral-occipital	Lingual	
	HC-DM	Posterior-cingulate	superiorfrontal	Lingual	Rostral-middle-frontal
		superiorfrontal	fusiform		Superior-parietal
					Lingual
	HC-MS			Lateral-orbitofrontal	
	MS-DM				
Correlation Analysis	HbA1c	Insula	Superior-frontal		Rostral-middle-frontal
			Supramarginal		Supramarginal
			Posterior cingulate		Posterior-cingulate

Table 1. Regions which showed statistical significance in the analysis

LB280.

Adaptive Response of Liver Perfusion in Preclinical Portal Vein Ligation

W. T. Zhao[1], W. Wei[2], K. H. Herrmann[1], M. Krämer[1], U. Dahmen[2], J. Reichenbach[1]

[1]Jena University Hospital, Friedrich-Schiller University, Medical Physics Group, Institute of Diagnostic and Interventional Radiology, Jena, Germany
[2]Jena University Hospital, Friedrich-Schiller University, Department of General, Visceral and Vascular Surgery, Experimental Transplantation Surgery, Jena, Germany

Introduction: In clinical practice, portal vein ligation (PVL, Fig.1-A) is a prelude of standard two-step hepatectomy to induce hypertrophy-atrophy complex. However, the regenerated liver volume often exhibits marked heterogeneity [1]. One theory of the liver"s response to PVL-induced blood supply restriction is that increased shear stress in the non-ligated lobes triggers liver regeneration to counterbalance functional decline. Yet, the intricate dynamics between non-ligated lobes and ligated lobes remains elusive [2]. To date, identification of liver function loss has relied on either invasive liver biopsy and/or systemic biochemical data (such as ASAT, ALAT, bilirubin), which provide limited insight into individual lobes [2]. Arterial spin labeling (ASL) MRI is a non-contrast, non-invasive technique that allows quantitative assessment of perfusion and can resolve the intralobar perfusion changes after PVL. The aim of our study was to delineate the changes in perfusion over time at days 1, 2, 3, and 5 after portal vein ligation in a cross-sectional study (Fig.1-B).

Methods: MRI data were collected on a Bruker BioSpec 94/20USR AVIII scanner using an 86 mm quadrature transceiver coil. A total of 23 animals were studied. PVL was performed by surgical ligation of portal branches of left lateral, left median and right lobes representing 65% PVL. After PVL (s. Fig 1A), animals were intubated for mechanical ventilation (tidal volume Vt = 5.5 ml, constant respiratory rate in the range of 45-55 bpm). To quantify the "kinetics" and re-distribution of the blood supply, respiratory-triggered MRI measurements and liver tissue harvesting were performed 1, 2, 3, or 5 days after surgery (POD1,2,3,5). Anatomic T2W images were acquired with a 3D VFA-RARE sequence. TR/TE = 1000/1.97 ms, RARE factor = 100, isotropic Resl = 350μm^3, BW = 250 kHz, TA ~7m30 s with trigger. Multiple single-slice perfusion images were acquired using a FAIR-EPI sequence with TR/TE = 12000/12.87 ms, 14 TIs ranging from 100 – 5150 ms, Resl = (625 x 625 x 2000) μm^3, TA ~ 10m 5s with trigger. Manual segmentation of ROIs on Bruker perfusion maps was performed with MATLAB (R2019a, MathWorks), followed by plotting and statistics (Python v.3.8, Seaborn v. 0.12.2, SciPy v.1.7.1). The Mann-Whitney test was applied, and $p < 0.05$ was considered significant.

Results: Starting from POD1, the ligated lobes (LML, LLL and RL, Fig.2-A, blue dashed line) showed a darker contrast compared with the non-ligated lobes (RML, CL, Fig.2-A, red dashed line), and this contrast persisted in the anatomical images. In control animals (Ctrl), the average tissue perfusion across all lobes was 307±50 ml/min/100g tissue. For the operated animals, both non-ligated lobes exhibited hyperperfusion at POD1 (Fig.2-C, RML: 440 ± 84 ml/min/100g tissue; CL: 390 ± 37ml/min/100g tissue), which was decreased at POD2 (insignificant compared to Ctrl) and reached equilibrium at POD5. In contrast, perfusion of ligated lobes remained minimal at approximately 150±50 ml/min/100g tissue. Notably, RML demonstrated the highest heterogeneity at POD1.

Discussion: The liver has a unique dual blood supply: it is supplied 25% by the hepatic artery and 75% by the portal vein [2]. When the portal vein of a lobe is ligated, the latter is supplied exclusively by the hepatic artery, which delivers oxygenated blood from the heart. Conversely, the non-ligated lobe is supplied with nutrient-rich, oxygen-poor blood from the intestine, resulting in a brighter contrast than the ligated lobes. The time course of the perfusion shows that the key time point is POD1-2. All ligated lobes exhibited an overshoot trend at POD1 and a re-elevated perfusion from POD2 on, suggesting a buffering response of the hepatic artery [3]. Our results demonstrate the dynamics of rapid perfusion changes after PVL in multiple lobes. Further studies are needed to refine and confirm our findings, preferably in a longitudinal study design.

Conclusion: ASL perfusion is a sensitive method to detect perfusion adaptation after PVL in the liver.

References

[1] Giuseppe Aragiusto, Antonio Ceriello, Antonio Giuliani, Carla Migliaccio & Fulvio Calise. Portal vein ligation. *In:* Minimally Invasive Surgery of the Liver, Updates in Liver Surgery. F. Calise and G. Casciola (eds.) Springer, 2013, pp 177–180
[2] Lautt W Wayne. Regulatory processes interacting to maintain hepatic blood flow constancy: Vascular compliance, hepatic arterial buffer response, hepatorenal reflex, liver regeneration, escape from vasoconstriction. *Hepatol Res* 2007; 37: 891–903.
[3] Christian Eipel, Kerstin Abshagen, and Brigitte Vollmar. Regulation of hepatic blood flow: The hepatic arterial buffer response revisited. World J Gastroenterol. 2010,16(48):6046-6057.

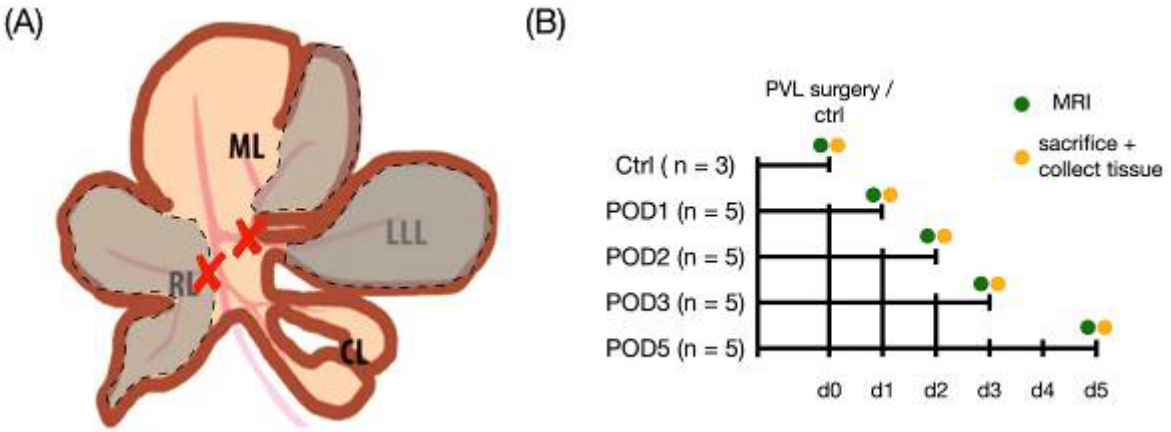

Figure 1. Schematic diagram of the operation and experimental design. (A) Portal vein ligation (PVL) was performed by ligating the right and left branches of the portal vein. (B) Cross-sectional design of the study: groups of five animals each underwent PVL and were examined at different time points after surgery. Liver tissue was collected immediately after MRI. A control group (n=3) was also measured as baseline. POD: post operation day, ML: medial lobe, RL: right lobe, LLL: left lateral lobe, CL: caudate lobe.

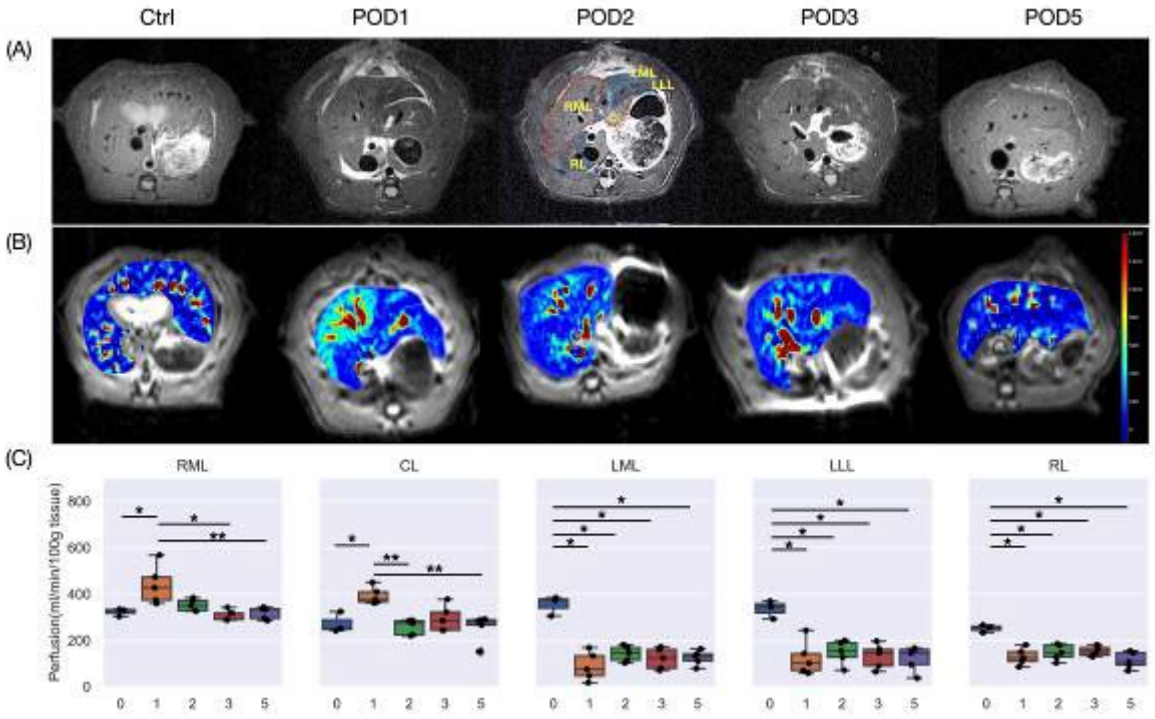

Figure 2. Temporal characteristics of perfusion in control (day 0) and PVL animals at 1, 2, 3, and 5 days after surgery. (A) Anatomy image from a 3D T2W VFA-RARE sequence; the dashed lines indicate the margins of each lobe, red: non-ligated lobe, blue: ligated lobe (B) Perfusion maps resulting from ASL and overlaid on the anatomical images of the FAIR-EPI sequence. (C) ROI-based quantitative perfusion values for each liver lobe. *: p <0.05, **: p <0.01

LB281

Detecting early structural changes of the connectome in Spinocerebellar Ataxia Type 3 using diffusion weighted MRI and machine learning

P. Wegner[1], M. Ferreira[1], J. Theisen[1], E. M. study group[1], T. Klockgether[1], J. Faber[1]

[1]Deutsches Zentrum für Neurodegenerative Erkrankungen, Klinische Forschung, Bonn, Germany

Introduction: Spinocerebellar ataxia type 3 (SCA3) is the most common autosomal dominant inherited ataxia worldwide [1]. So far no treatment is available, but the first gene therapy trials started recently. Thus, there is an urgent need for non-invasive quantitative biomarkers and a particular interest in the pre-ataxic stage of SCA3 as clinical scales lack sensitivity before the onset of ataxia. Understanding the alterations in brain and cerebellar networks associated with SCA3 can provide insights into the pathophysiology, and might serve as biomarkers for monitoring of disease progression or stratification of mutation carriers. Previous efforts showed affection in the connectome of SCA3 mutation carriers, which motivated this work [2].

The aim of this study is to analyze the connections between regions of interest (ROIs) of the human connectome of SCA3 mutation carriers. Specifically, the aim is to identify alterations in the pre-ataxic stage before the ataxia onset that might serve as potential imaging biomarkers.

Methods: In a longitudinal study we acquired diffusion-weighted MRI data of 157 participants from three groups (35 pre-ataxic SCA3 mutation carriers (preATAXIC), 82 ataxic SCA3 (ATAXIC), and 40 healthy controls (HC)) at 11 sites. The Scale for Assessment and Rating of Ataxia (SARA;[3]) was used to assess ataxia severity. Pre-ataxic mutation carriers were defined by the accepted cut-off of < 3 points in the SARA sum score.

Diffusion data was acquired on 3T Siemens scanners using an EPI sequence with: b-values of 700 and 1000s/mm^2, 30 directions per shell, 2mm isotropic resolution, echo time of 88 ms, repetition time of 12100 ms and nominal flip angle of 90 degrees.

A whole brain tractogram of 100 million streamiles was generated by initiating the seeding from a cerebellum and brainstem mask. From the tractogram, an adjacency matrix was extracted where each ROI (125 in total) corresponds to a row/column and each cell is weighted by the number of streamlines connecting two ROIs.

Cerebnet [4] was used for subsegmentation of the cerebellum, Fastsurfer [5] and Freesurfer [6] for subsegmentation of the cerebrum and the brainstem.

First, all considered tracts were ranked by significance using a t-test on each tract comparing groupwise. A shallow neural network (SNN) was trained on classifying HC vs. preATAXIC and HC vs. ATAXIC. The SNN was fed with the number of streamlines between ROIs represented in a joint feature vector. The model was evaluated with a leave-one-out cross validation, while being fed with the k most significant tracts, where k ranged from 1 to the number of tracts below a threshold for which a tract is considered to be significant ($p < 0.01$).

Results: The SNN reported an macro F1-score of 65.01% in the classification of HC vs. preATAXIC and an macro F1-score of 85.30% in the classification of HC vs. ATAXIC.

Generally, the conducted experiments have shown that in early stages of SCA3 (preATAXIC) a lot of tracts are not altered significantly and the model cannot utilize a majority of tracts. In the classification HC vs. preATAXIC the model performed best (65.03% F1), using the k=44 most significant tracts. On the other side, the brain of a patient in ATAXIC shows more tracts affected (Fig. 1,2) and the k=216 most significant tracts given to the model provided the best performance (85.30% F1). Moreover, in ATAXIC the most significant tracts focus on regions mainly located in the cerebellum and the brainstem while in preATAXIC the most significant tracts do not have such a strong focus on those regions (Fig. 3,4). For HC vs. preATAXIC 49 and for HC vs. ATAXIC 561 tracks were significantly affected.

Discussion: The presented work has shown that already in the pre-ataxic stage of SCA3, significant alterations in the connectome are measurable. Moreover, a SNN is able to classify between pre-ataxic and healthy connectomes with 65.02% F1-score. Considering ataxic SCA3 patients, the pattern was more widespread, with 85.30% F1-score. Note, that all tracts between the cerebellum and cerebrum, necessarily pass the brainstem. Hence, if such a tract are affected the corresponding sub-tract between brainstem and cerebrum respectively cerebellum is also affected.

Conclusion: Our results underline that alterations of the connectome start before the clinical onset of ataxia. Correct classification of healthy versus ataxic SCA3 was possible with a high F1-score. It was less persuasive for pre-ataxic

SCA3. Future work will allow more detailed characterization of the structural alterations of the brain in early stages of SCA3, for which longitudinal data will be used.

References

1. https://doi.org/10.1038/s41572-019-0074-3
2. https://doi.org/10.3389/fnins.2018.00935
3. https://doi.org/10.1212/01.wnl.0000219042.60538.92
4. https://doi.org/10.1016/j.neuroimage.2022.119703
5. https://doi.org/10.1016/j.neuroimage.2020.117012
6. https://doi.org/10.1016/j.neuroimage.2012.01.021

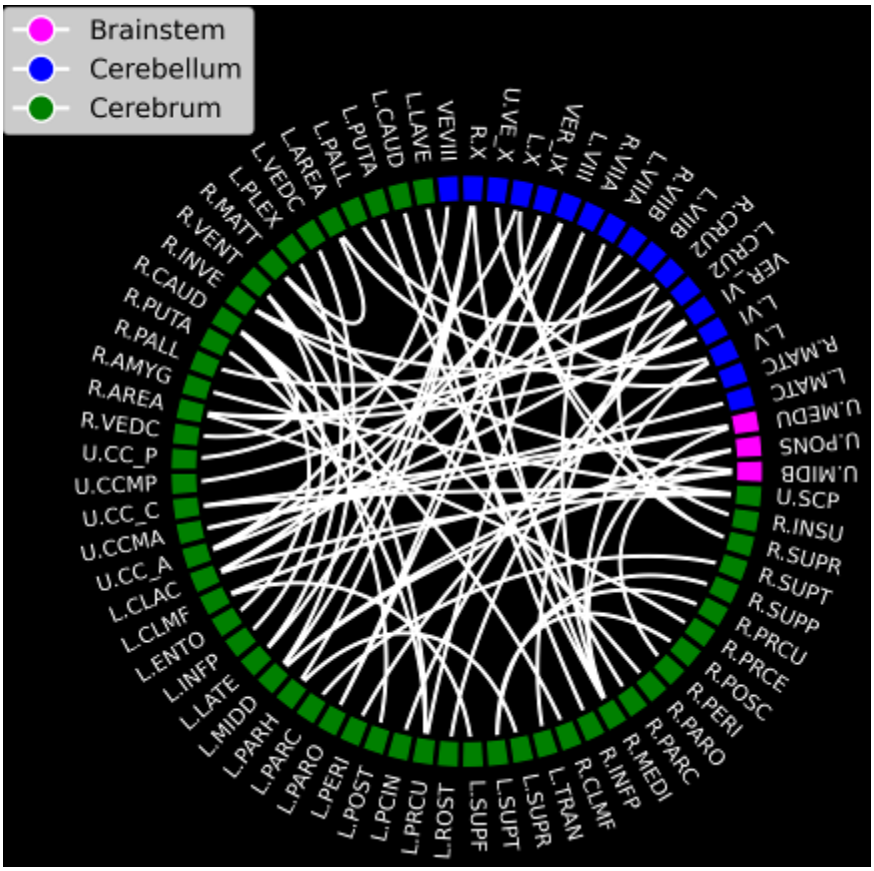

Fig. 1: Tracts for which more than 50% of the preATAXIC population deviates more than the standard deviation of the HC

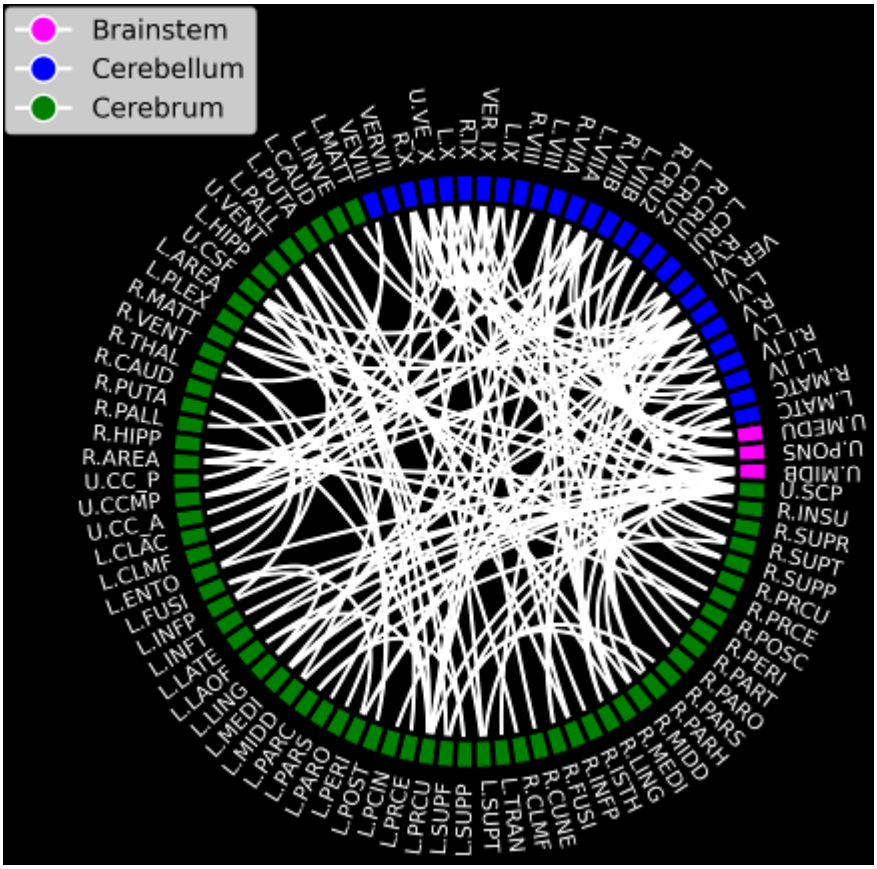

Fig. 2: Tracts for which more than 50% of the ATAXIC population deviates more than the standard deviation of the HC

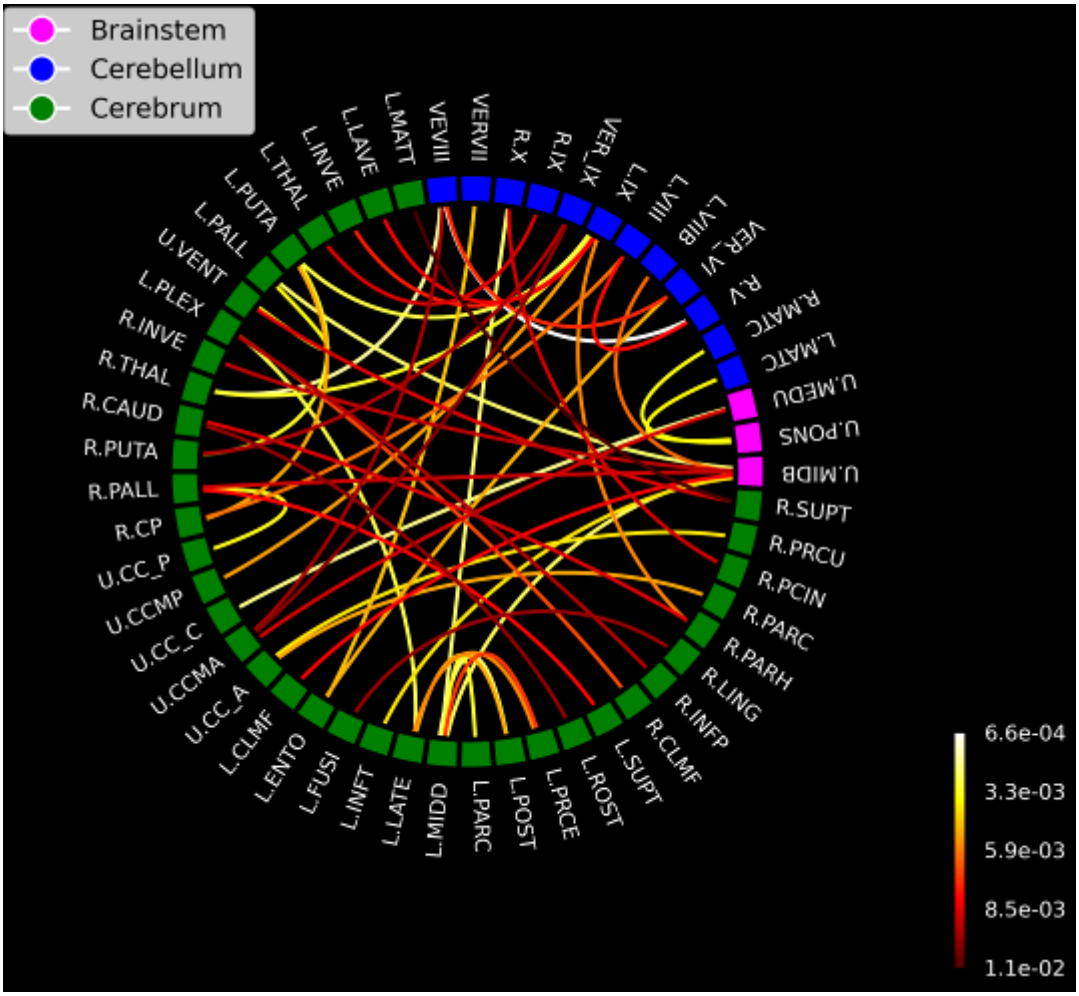

Fig. 3: 50 most significant (group difference HC and preATAXIC) tracts.

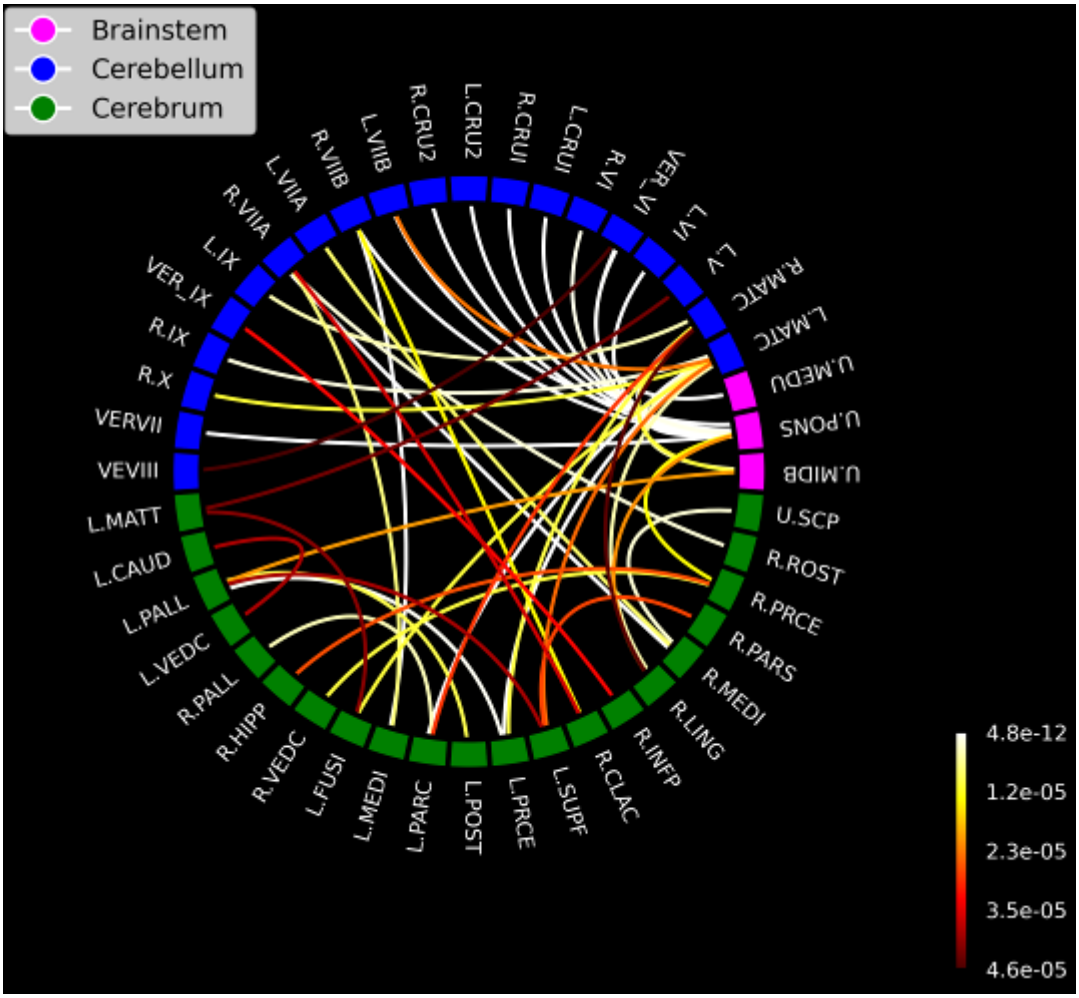

Fig. 4: 50 most significant (group difference HC and ATAXIC) tracts

LB282.

Resting-state functional connectivity analysis using BOLD and diffusion fMRI

I. de Riedmatten[1], W. Olszowy[2], I. Jelescu[1]

[1]Université de Lausanne, Lausanne, Switzerland
[2]Ecole polytechnique fédérale de Lausanne (EPFL), Lausanne, Switzerland

Resting-state functional Magnetic Resonance Imaging(rsfMRI) examines the coordinated activity among brain regions at rest1. Historically based on Blood Oxygenation-Level-Dependent(BOLD) signal, rsfMRI has recently been characterized using diffusion fMRI (dfMRI)2. The latter differs from BOLD by focusing on neuromorphological coupling (transient cell deformation) instead of neurovascular coupling. It offers two advantages: spatial specificity, as the signal arises from neuronal activity and not from neighboring veins3, and temporal specificity, its response function being faster than the hemodynamic one2. This technique paves the way to better understanding brain activity, and in particular activity in the white matter (WM) and functional connectivity (FC) anti-correlations. BOLD signal in WM has been so far regressed out as nuisance variable. Indeed, due to less vasculature and metabolic activity, BOLD exhibits low sensitivity in WM4, as opposed to dfMRI5. As for anti-correlations, in BOLD rsFC analysis, some networks are known to negatively correlate with each other (e.g. default mode vs dorsal attention system6). These anti-correlations are thought to be caused by either neuronal inhibition inducing negative BOLD or vascular effects[6, 7, 8], which should not affect dfMRI. We examine the specific signatures of rs dfMRI in terms of WM sensitivity and anti-correlations, as compared to BOLD.

Data from 13 subjects were collected on a 3T MRI system using DW-TRSE-EPI (dfMRI) and 11 using SE-EPI (T2-BOLD) sequences. DW-TRSE-EPI provided apparent diffusion coefficient (ADC) timecourses (2s resolution), as well as pseudo-BOLD contrast with small diffusion-weighting (2s resolution). SE-EPI yielded BOLD timecourses with 1s resolution. Following established pre-processing2, FC matrices were calculated using ROIs of Neuromorphometrics (NMM) and Johns Hopkins University (JHU) atlases, and partial pairwise correlation, regressing out the global signal (Fig. 1). FDR-corrected Wilcoxon signed-rank tests were employed to determine significant correlations of the BOLD FC. FC in these significant edges was compared between the three techniques within different groups (whole brain, GM-GM, WM-WM, WM-GM, between and within hemisphere(s)), using Mann-Whitney U tests with Bonferroni correction.

Positive correlations for BOLD revealed excellent agreement with dfMRI and pseudo-BOLD (Fig.2), with a slope of linear regression in [0.85, 1.02]. However, the slopes of the negative correlations deviate from the diagonal. The amount of positive and negative correlations in different brain areas are then summarized in Fig.3 and shows that the positive correlations were preserved between ADC, Pseudo-Bold and BOLD. When significant differences in positive connectivity strength exist, Pseudo-Bold displays the largest positive correlations. Regarding the anti-correlations, they were systematically attenuated with decreasing vascular contribution to the contrast (BOLD < Pseudo-BOLD < ADC). No significant anti-correlations were found in the WM-WM case with either contrast.

As depicted in Fig.2, the agreement of positive correlations suggests that ROIs have congruent activation among the contrast. Remarkably, highest positive correlations with pseudo-BOLD suggest either an additive contribution of BOLD and diffusion effects (pseudo-BOLD contains both T2- and diffusion-weighting) or a cleaner functional signal through suppression of direct contributions from the blood pool and physiological artifacts (via b=0.2). However, they induce different anti-correlations. The decreasing amplitude of negative correlation with reduced hemodynamic contributions supports a vascular origin underlying anti-correlations and thereby a distinct functional contrast underlying dfMRI. Indeed, it has been shown that anti-correlations are observed in the vicinity of cerebrospinal fluid (CSF) and large veins6. Neuronal inhibition may also drive negative BOLD, as it has been shown that membrane hyperpolarization leads to vasoconstriction8. As opposed to depolarization that induces significant cell swelling to be detected as ADC drop, cell shrinkage is small during hyperpolarization9. This may explain why the anti-correlations are not as prominent in ADC as in BOLD.

Under comparable brain activity and physiological conditions, dfMRI and BOLD fMRI capture different connectivity patterns, which represents a positive stride towards maximizing the potential of FC. Attenuation of anti-correlations in dfMRI could suggest a vascular origin to this phenomenon or be explained by the non-significant cell shrinkage following neuronal inhibition.

1M.H. Lee, AJNR Am J Neuroradiol 2013
2Wiktor Olszowy, bioRxiv 2021
3Amir Shmuel, NeuroImage 2007
4John C. Gore, Magn Reson Imaging 2019
5Kwon, Lee, NeuroPhotonics 2023

6Marta Bianciardi, J Cereb Blood Flow Metab 2011
7Wade, Neuron 2002
8Anna Devor, J Neurosci 2007
9James A Fraser and Christopher L-H Huang, J Physiol. 2004

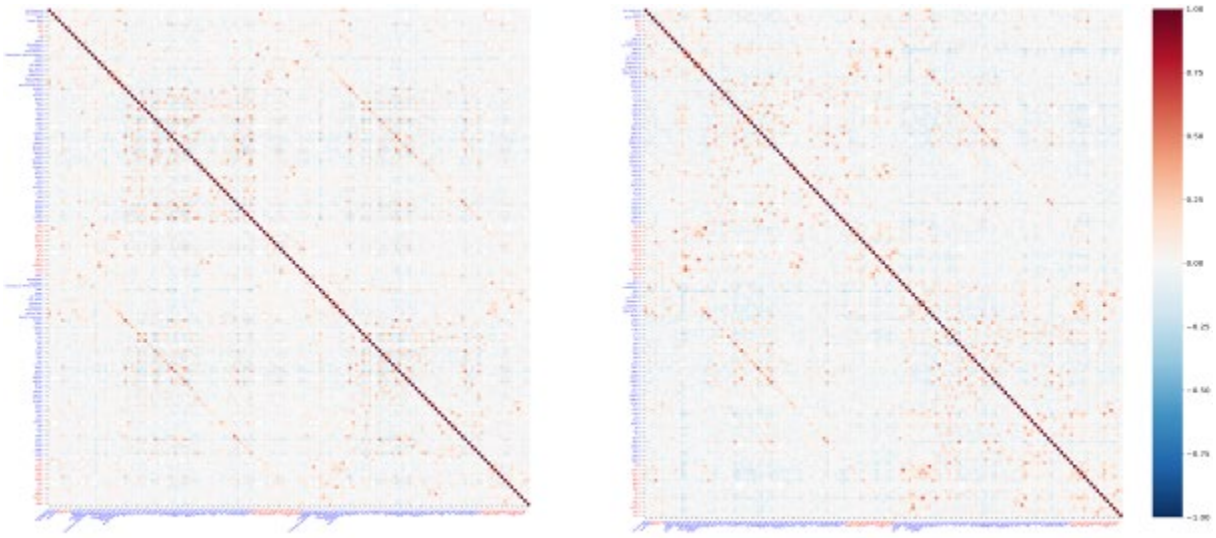

a) b)

Fig.1 BOLD (a) and diffusion (b) functional connectivity at 3T. The labels are ordered according to the right (R) and left (L) hemisphere. Blue and red correspond to GM (NMM atlas) and WM (JHU atlas), respectively.

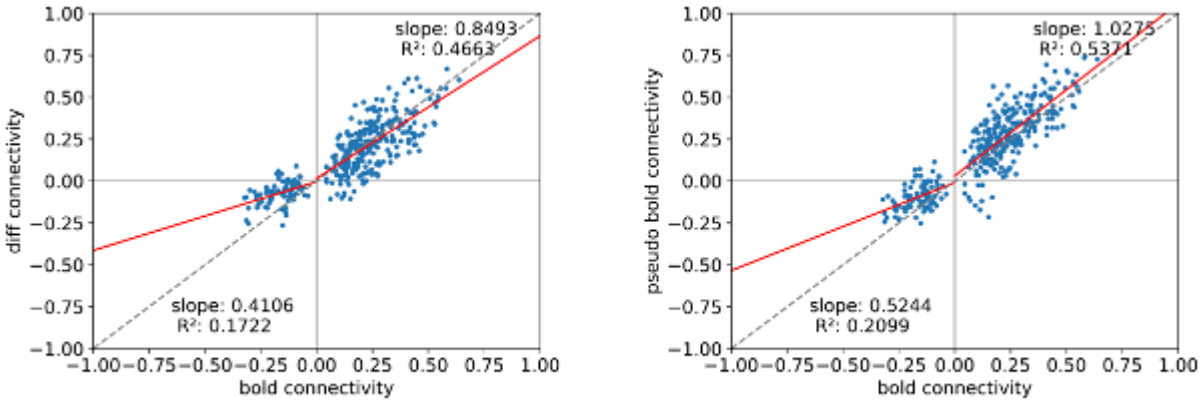

a) b)

Fig. 2 Functional connectivity correlation between Diffusion and Bold (a) and Pseudo-Bold and Bold (b) at 3T.

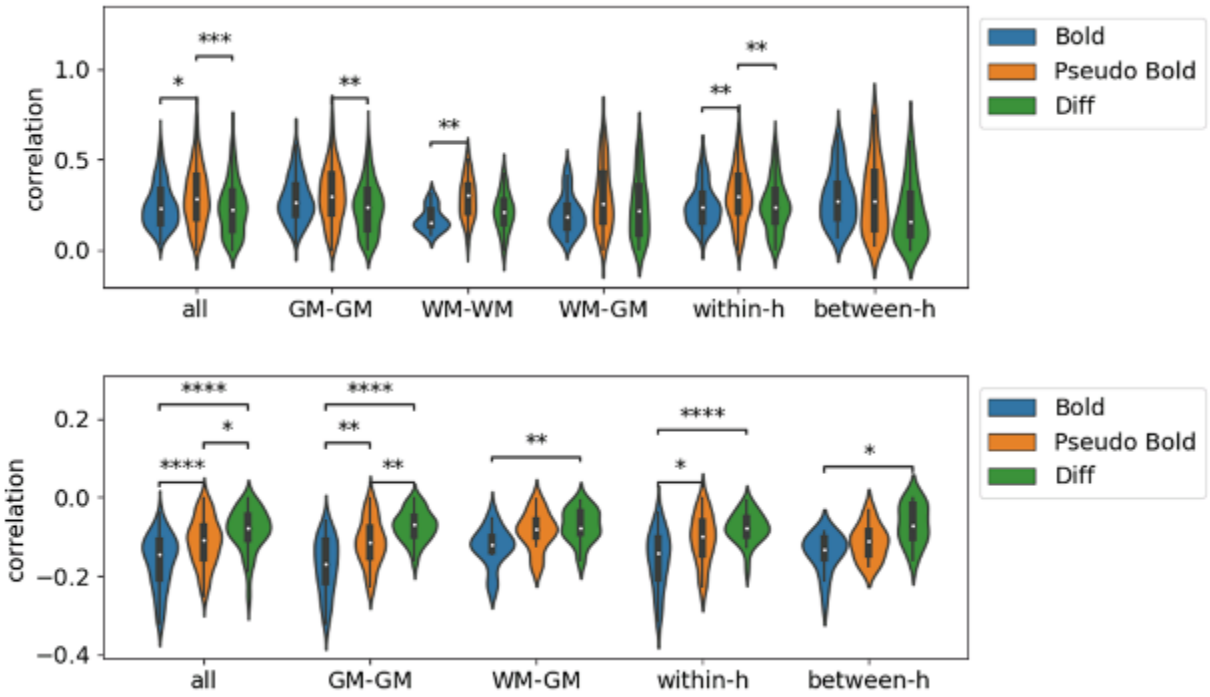

Fig. 3 Positive and negative functional connectivity correlations for Bold, Diffusion and Pseudo-Bold in all the brain, between GM, between WM, between WM and GM, within hemisphere or between hemisphere. Mann-Whitney-Wilcoxon test two-sided with Bonferroni correction. * : 0.01<p<= 0.05, ** : 1e-3<p<=0.01, *** : 1e-4<p<=1e-3, **** : p<=1e-4.

LB283.

Implementation of robust double-diffusion-encoded spectroscopy (DDES) in the human brain on a clinical MR scanner using metabolite cycling

A. Döring[1,2], J. Mosso[2], R. Kreis[3,4], D. K. Jones[1], C. Najac[5], M. G. Hall[6], H. Lundell[7], L. Xin[2], I. Ronen[8]

[1]Cardiff University, Brain Research Imaging Centre (CUBRIC), Cardiff, United Kingdom
[2]EPFL Lausanne, CIBM Center for Biomedical Imaging, Lausanne, Switzerland
[3]University of Bern, MR methodology, Institute of Diagnostic and Interventional Neuroradiology, Bern, Switzerland
[4]University of Bern, Translational Imaging Center, Sitem-Insel, Bern, Switzerland
[5]Leiden University Medical Center, C.J. Gorter Center for High Field MRI, Department of Radiology, Leiden, Netherlands
[6]National Physical Laboratory, Teddington, United Kingdom
[7]Copenhagen University Hospital Amager and Hvidovre, Danish Research Centre for Magnetic Resonance, Hvidovre, Denmark
[8]University of Sussex, Clinical Imaging Sciences Centre, Brighton and Sussex Medical School, Brighton, United Kingdom

Introduction: Diffusion-weighted MR spectroscopy (DW-MRS) allows measuring diffusion properties of intracellular metabolites. Modelling techniques have shown promise in retrieving morphological properties of neuronal (tNAA) and glial (tCho) cells from metabolite diffusion. However, to this end the inverse problem is ill defined. A possible solution is multi-parametric DW-MRS, where diffusion-encoding or echo-time is chosen to sensitize sequences to specific structural features and length scales. Double-diffusion-encoding (DDE) is of particular interest since it allows isolating contributions from compartments such as cylinders and spheres[1]. In combination with MRS, double-diffusion-encoded spectroscopy (DDES) can provide cell specific morphological information[2]–[5]. However, retrieving nuanced directional differences in metabolite diffusion requires careful suppression of motion effects. To alleviate this problem, we study the applicability of DDES in combination with metabolite-cycling (MC) and motion-compensation (MoCom) for obtaining robust microscopic anisotropy data on brain metabolites on a clinical MR scanner.

Methods:
Data acquisition: Measurements were conducted on 3T PRISMA MR scanners (Siemens Healthcare) using a 32-channel headcoil. Non-water suppressed diffusion-weighted spectra were acquired using a semiLASER sequence[6] (TE/TR: 125/2500ms) extended by MC and DDE (Fig. 1). The crushing scheme was optimized to reduce spurious diffusion-weighting. Diffusion-weighting was applied at two b-values of 0 and 5130s/mm². At the lowest b-value 48 transients were acquired. At the highest b-value DDE encoding was applied along three orthogonal planes ([1.0 1.0 -0.5], [-0.5 1.0 1.5] and [1.0 -0.5 1.0]) with an 8-step rotation cycle (θ:0, 45, 90, 135, 180, 225, 270, 315°) in all three planes (3 distinct combinations). The DDE gradient timings were chosen as Δ/δ/ε/τ: 32/14/1/39ms (Fig. 1) resulting in a diffusion-time of 27.3ms. For each rotation angle data with negative and positive gradient polarity were acquired with 24 transients each (total of 144 transients per angle). MPRAGE images (1mm³ isotropic) were used for voxel positioning and tissue segmentation (Fig.2). The total measurement time was 1hr10min per subject. Data were obtained from 3 healthy subjects (29.7±5.9yrs, 1 female). VOI was placed in the corona radiata (CR: 11.6mL) in the first subject, in the posterior cingulate cortex (PCC: 12mL) in the second, and in the Cerebellum (CBM: 12.9mL) in the third (Fig.2).

Analysis, Fitting and Modeling: MC preserves a water reference for each transient, which was used for coil-channel combination, phase-offset, frequency-drift and eddy-current correction and motion compensation (MoCom) relying on an optimized Matlab pipeline[7]. Metabolite basis-sets were simulated with MARSS for 18 metabolites[8]. Linear combination modeling was done sequentially in FiTAID[9]. The dependence of the estimated metabolite areas on the rotation-angles was fitted with a biophysical model emulating a powder averaged signal with 256 uniformly oriented diffusion tensors with a radial $D_{||}$ and axial $D_{\perp}$ diffusion-component[5]. The microscopic fractional anisotropy (μFA) was calculated from $D_{||}$ and $D_{\perp}$[5]. To assess the benefits of compensating for motion-induced signal loss, this analysis was performed twice, without and with MoCom.

Results and Discussion: Fig.2 shows the spectral quality as obtained after MoCom for the 3 subjects in the CR, PCC and CBM (windowed with 3Hz Gaussian for better visualization). Apart from the major singlets (tNAA, tCr, tCho) the contribution from J-coupled metabolites (mI, Glu) is also visible. The NAA metabolite peak exhibits a clear oscillation pattern characteristic for microscopic anisotropy.

Fig.3 shows the fitted S(θ), μFA, $D_{||}$ and $D_{\perp}$ for tNAA, tCr and tCho with and without MoCom. The oscillation patterns S(θ) are more consistent with MoCom (lower numbers of outliers) and the fitting uncertainties reduce substantially for the μFA (-24%), $D_{||}$(-40%) and for $D_{\perp}$(-47%). The measurement in PCC was found to be most affected by motion (highest variance in the water reference) and documents the improvement possible with the use of MC and MoCom.

Moreover, fitting uncertainties were highest for $D_{\perp}$ while μFA and $D_{\parallel}$ could be fitted more robustly. The oscillation amplitudes for tNAA, tCr and tCho are highest in the WM rich CR and lowest in the CBM. This is supported by similar oscillation patterns of the water signal (Fig.4).

The fitted water signal presented in Fig. 4 is well in line with results reported by Lundell et al.[5]. Only for the acquisition in the PCC, with stronger motion aritifacts, yield differences in μFA, $D_{\parallel}$ and $D_{\perp}$ between data processed without and with MoCom (potentially due to higher water SNR).

Conclusion: We have shown that MC improves DDES and can be used to obtain more robust results and to shorten measurement time by determining metabolite and water diffusion simultaneously.

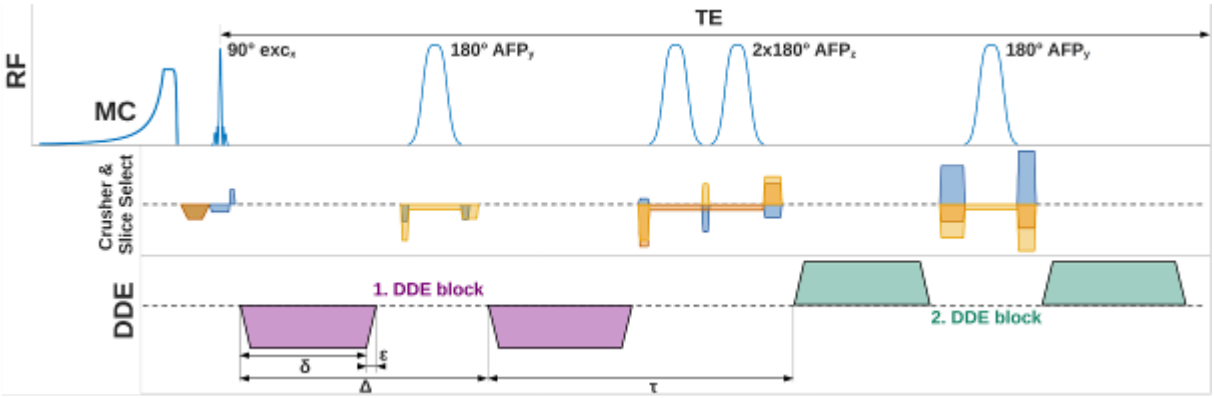

Figure 1: Sequence chronogram of the DDES semiLASER sequence with two monopolar DDE blocks. The crushing scheme was optimized to a minimum spurious diffusion-weighting of 9s/mm².

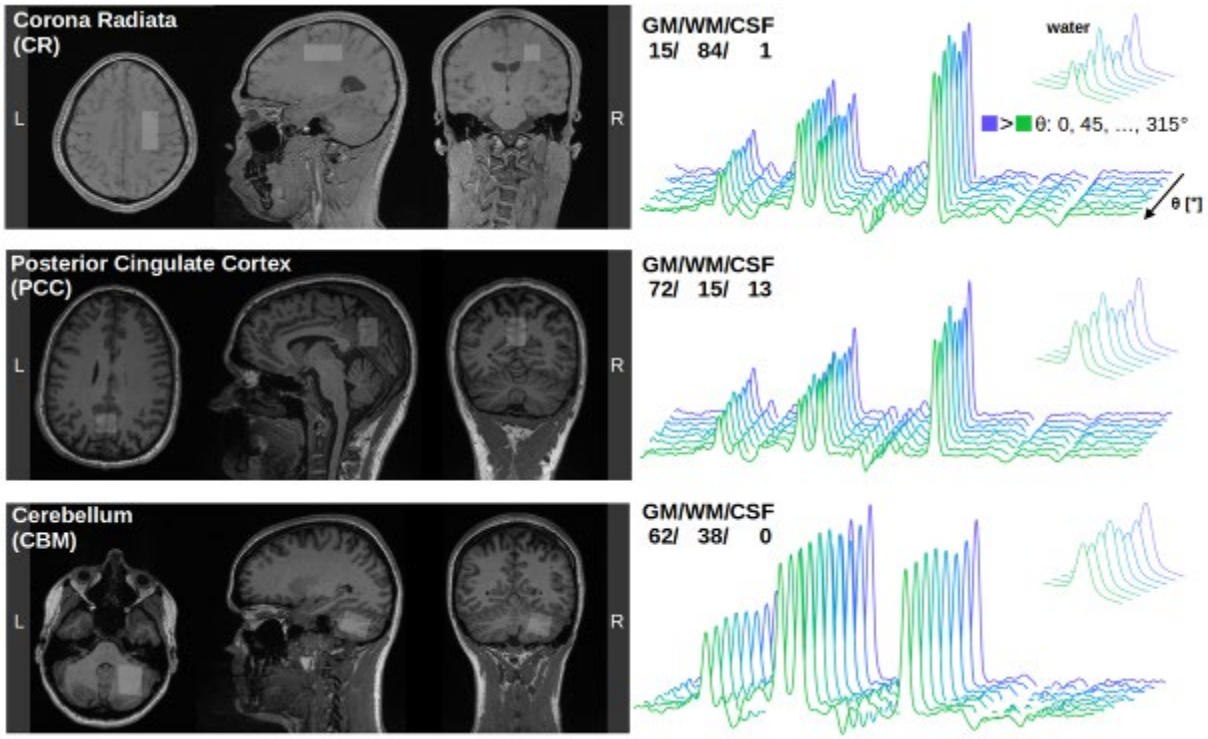

Figure 2: Left: Voxel position in the three subjects (tissue segmentation reported in %). Right: DDE Spectra for metabolites and water at different rotation-angles (θ).

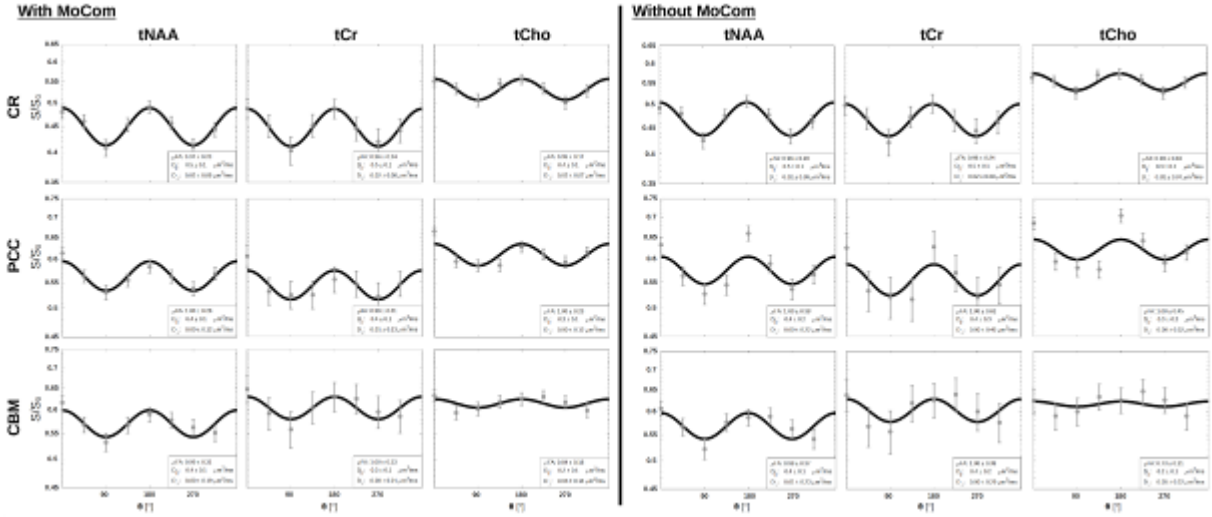

Figure 3: Fitting of the modulation of the diffusion signal with changing DDE angle for the three major metabolites tNAA, tCr and tCho with and without motion compensation (MoCom). Fitting parameters and uncertainties are reported in the lower right corner for each metabolite and condition.

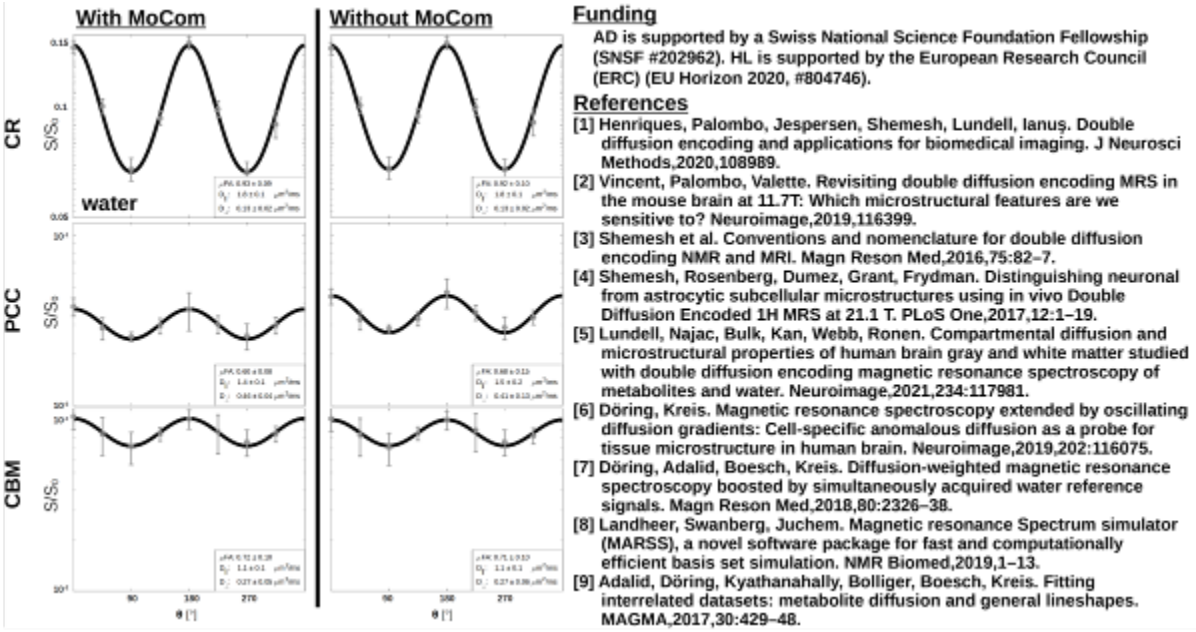

Funding

AD is supported by a Swiss National Science Foundation Fellowship (SNSF #202962). HL is supported by the European Research Council (ERC) (EU Horizon 2020, #804746).

References

[1] Henriques, Palombo, Jespersen, Shemesh, Lundell, Ianuș. Double diffusion encoding and applications for biomedical imaging. J Neurosci Methods,2020,108989.

[2] Vincent, Palombo, Valette. Revisiting double diffusion encoding MRS in the mouse brain at 11.7T: Which microstructural features are we sensitive to? Neuroimage,2019,116399.

[3] Shemesh et al. Conventions and nomenclature for double diffusion encoding NMR and MRI. Magn Reson Med,2016,75:82–7.

[4] Shemesh, Rosenberg, Dumez, Grant, Frydman. Distinguishing neuronal from astrocytic subcellular microstructures using in vivo Double Diffusion Encoded 1H MRS at 21.1 T. PLoS One,2017,12:1–19.

[5] Lundell, Najac, Bulk, Kan, Webb, Ronen. Compartmental diffusion and microstructural properties of human brain gray and white matter studied with double diffusion encoding magnetic resonance spectroscopy of metabolites and water. Neuroimage,2021,234:117981.

[6] Döring, Kreis. Magnetic resonance spectroscopy extended by oscillating diffusion gradients: Cell-specific anomalous diffusion as a probe for tissue microstructure in human brain. Neuroimage,2019,202:116075.

[7] Döring, Adalid, Boesch, Kreis. Diffusion-weighted magnetic resonance spectroscopy boosted by simultaneously acquired water reference signals. Magn Reson Med,2018,80:2326–38.

[8] Landheer, Swanberg, Juchem. Magnetic resonance Spectrum simulator (MARSS), a novel software package for fast and computationally efficient basis set simulation. NMR Biomed,2019,1–13.

[9] Adalid, Döring, Kyathanahally, Bolliger, Boesch, Kreis. Fitting interrelated datasets: metabolite diffusion and general lineshapes. MAGMA,2017,30:429–48.

Figure 4: Modulation and fitting result of the simultaneously acquired water signal with and without MoCom.

LB284.

Deep-learning enabled Comprehensive 7T CEST imaging in cerebral tumors

M. S. Fabian[1], J. R. Rajput[1], T. A. Möhle[1], S. Rampp[1,2], M. A. Schmidt[1], G. Lahmer[3], F. Putz[3], A. Dörfler[1], M. Zaiss[1,4,5]

[1]University Hospital Erlangen, Institute of Neuroradiology, Erlangen, Germany
[2]University Hospital Erlangen, Department of Neurosurgery, Erlangen, Germany
[3]University Hospital Erlangen, Department of Radiation Therapy, Erlangen, Germany
[4]Max Planck Institute for Biological Cybernetics, High-field Magnetic Resonance Center, Tübingen, Germany
[5]Friedrich-Alexander-Universität Erlangen-Nürnberg, Department of Artifical Intelligence in Biomedical Engineering, Erlangen, Germany

Introduction: Chemical exchange saturation transfer (CEST) MRI detects the signal of low concentrated molecules utilizing proton exchange and selective RF saturation. This study aims to combine multiple saturation schemes into one comprehensive protocol covering three prominent CEST exchange regimes.

Methods: Measurements are conducted at a MAGNETOM Terra.X 7T scanner (Siemens Healthineers AG, Erlangen, Germany) with a 32Rx/8Tx-channel head coil (Nova Medical, Wilmington, MA) after written informed consent by the subjects and approval of the local ethics committee.

The CEST image readout was the 3D snapshot GRE MIMOSA CEST.[1], [2] Low B1 CEST measurements for detection of amide, rNOE, Guanidine and ssMT pool were done according to [3] and evaluated by deepCEST[4]. Intermediate B1 CEST (GluCEST) is measured according to [5]. High B1 CEST is realized as in [6]. An overview of the measurement and post-processing is given in Figure 1.

Results: We were able to reduce the scan time of our protocol from initially 40 minutes to 15 minutes by post-processing optimization and neural network employment. This makes the protocol feasible to be scanned in clinical studies. Three patients with high grade tumors (Glioblastoma WHO grade 4) have been enrolled so far in this study. A representative slice of a female patient is shown in Figure 2. The Gadolinium enhanced suspected metastasis (Fig. 2I) is hyperperfused (Fig. 2H) and shows correlations with the amide (Fig. 2A), amine (Fig. 2E) and hydroxyl (Fig. 2F) CEST maps. The hyperintensity in these CEST maps shows substructures and extends even beyond the tumorous area outlined by clinical imaging. These findings apply to the other patients as well. After the CEST measurement, a biopsy was performed to identify this suspected metastasis as a glioblastoma WHO CNS grade 4, IDH wildtype.

Discussion: So far, amide, amine and hydroxy comprehensive CEST maps showed correlation with contrast enhanced clinical imaging.[7]–[11] We also spot decreased ssMT and rNOE signal in tumorous areas.[12], [13] The data from this combined MRI protocol aligns well with the findings of previous literature. Additionally, we are able to see features in several B1 amplitude regimes, that are not apparent in clinical imaging. Future subject recruitment is estimated to solidify these statements. Comprehensive CEST maximizes the number CEST features per dataset, which will help to improve diagnostic performance, but also to identify the importance of each feature in the same patient.

Conclusion: We approach the goal to produce a protocol covering "all" CEST effects by a further step with the comprehensive CEST protocol of 15 minutes scan time. Comprehensive CEST is planned to be applied to more tumor patients and in larger clinical studies in order to reveal which combination of contrasts has the strongest clinical performance regarding tumor characterization or therapy response.

References

1. Zaiss, M., Ehses, P. & Scheffler, K. *NMR Biomed.* **31**, e3879 (2018).
2. Liebert, A. *et al. Magn. Reson. Med.* **82**, 693–705 (2019).
3. Mennecke, A. *et al. NMR Biomed.* e4717 (2022).
4. Hunger. Leonie & Rajput, Junaid. *Magn. Reson. Med.* (2022).
5. O"Grady, K. P. *et al. Front. Neurol.* **13**, (2022).
6. Zaiss, M. *et al. NMR Biomed.* **32**, e4113 (2019).
7. Cai, K. *et al. NMR Biomed.* **28**, 1–8 (2015).
8. Jones, K. M., *J. Magn. Reson. Imaging* **47**, 11–27 (2018).
9. Schuenke, P. *et al. Magn. Reson. Med.* **77**, 571–580 (2017).
10. Paech, D. *et al.* **20**, 1661–1671 (2018).
11. Xu, X. *et al. Tomography* **1**, 105–114 (2015).
12. Paech, D. *et al. PLoS One* **10**, e0121220 (2015).
13. Meissner, J.-E. *et al. J. Magn. Reson. Imaging* **50**, 1268–1277 (2019).

14. Breitling, J. *et al.* **32**, e4133 (2019).

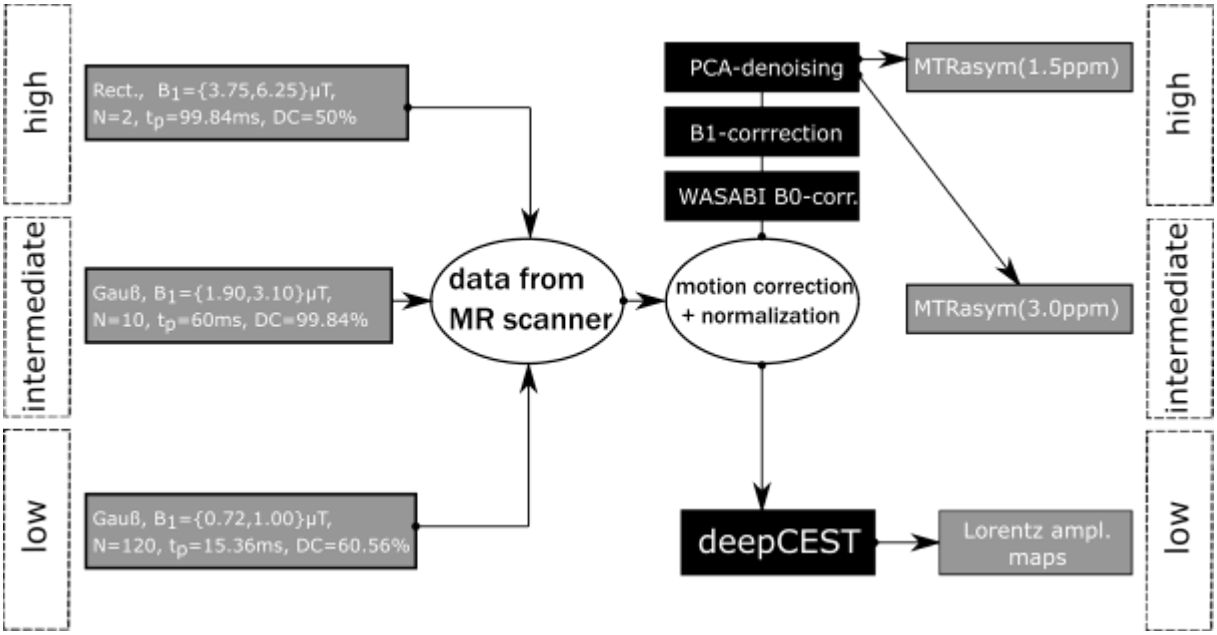

Figure 1: Overview of the comprehensive CEST protocol regarding the different B1 amplitude regimes. Low B1 regime data is evaluated by the deepCEST network.[4] Intermediate and high B1 regime data are B0 corrected using the WASABI[9] method. They are B1 corrected and denoised using a Principal Component Analysis.[3], [14]

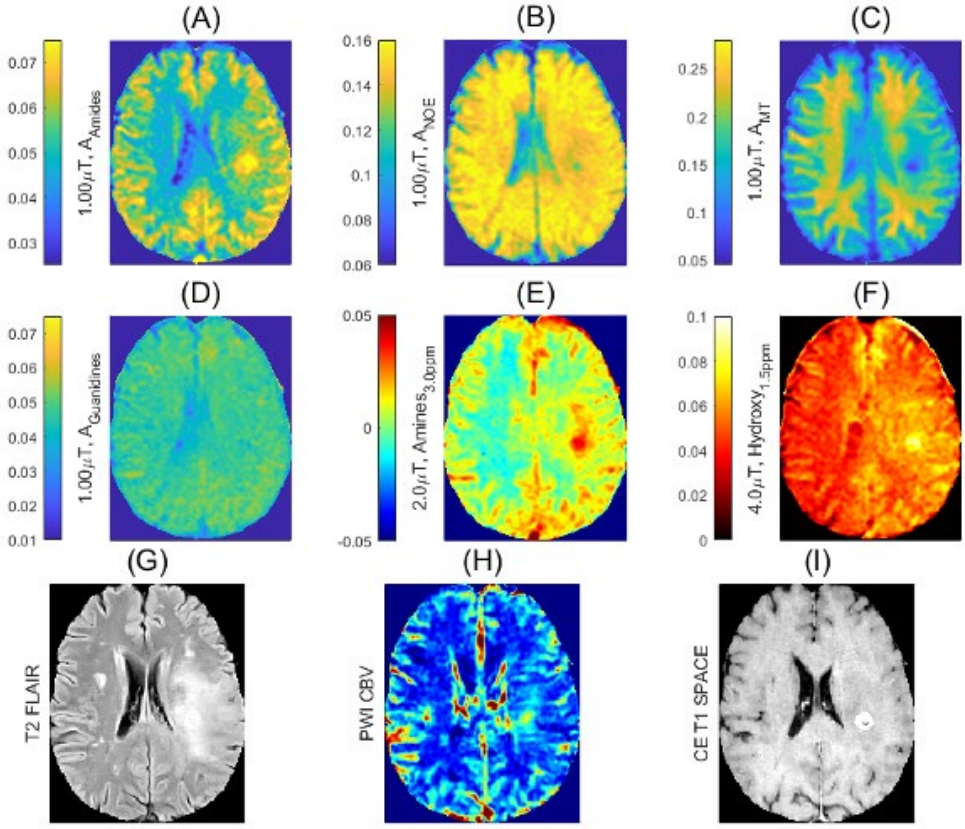

Figure 2: Comprehensive CEST maps of a female patient after breast surgery due to breast cancer. The Gadolinium enhancement is either a suspected metastasis or glioma, as suggested by the radiologists. Low (A)-(D), intermediate (E) and high (F) B1 regime maps show correlation to Gadolinium enhancement as well as interesting new features not visible in clinical imaging at 1.5T (G)-(I). Suspected metastasis hyperintensity correlates with Amide (A), Amine (E) and Hydroxyl (F) maps, but also shows structures similar to the perifocal edema (G). After biopsy the suspected metastasis was identified as glioblastoma WHO CNS grade 4, IDH wildtype.

LB285.

Measurement of NAD+(H) Dynamics Using 31P Functional MRS in the Occipital Lobe: Insights into Energy Metabolism Mechanisms during Visual Stimulation

A. Kaiser[1], F. Anvari Vind[1], M. Widmaier[1], D. Wenz[1], L. Xin[1]

[1]CIBM, Center for Biomedical Imaging, École Polytechnique Fédérale de Lausanne (EPFL), Animal Imaging and Technology, Lausanne, Switzerland

Introduction: Nicotinamide adenine dinucleotide (NAD+) and its reduced form (NADH) are important coenzymes orchestrating a variety of physiological processes within the human brain. These molecules serve as indispensably dynamic redox regulators, closely intertwined with energy metabolism, cellular signaling cascades, and the maintenance of cellular redox homeostasis. NAD+ functions as a central participant in an assortment of enzymatic reactions, including those underpinning glycolysis, the tricarboxylic acid cycle, and oxidative phosphorylation. It is involved in the conversion of substrates into bioenergetic currency, like adenosine triphosphate (ATP), while NADH acts as a reservoir of energy accumulated through these metabolic pathways.

Furthermore, NADH and NAD+ have been implicated in various signaling pathways and neurotransmitter dynamics. Deficits of NAD content have been reported in aging, neurodegenerative and psychiatric disorders. Monitoring their functional dynamics could reveal how these coenzymes contribute to neural communication, synaptic plasticity, and the modulation of neurotransmitter release, thereby unraveling the underpinnings of cognitive processes.

The non-invasive measurement of NAD content in vivo has been demonstrated using 31P MRS at high magnetic fields. Dynamic measurements of NAD+(H) fluctuations in the human brain, especially during functional activation, have remained challenging due to low sensitivity. This study therefore aims to investigate the feasibility of using 31P functional MRS (fMRS) to measure NAD+(H) dynamics in the occipital lobe during a visual stimulation task at 7T.

Methods: Fourteen young, healthy participants (mean age: 23.3±3.1 years, 6 female) were recruited for this study. Dynamic 31P MRS data were acquired using a 7T MRI scanner (Siemens Medical Solutions, Erlangen, Germany) with a custom-built 31P (7 cm diameter) surface coil and a quadrature 1H surface coil, using an ISIS 3D localization sequence (TR/TE=3/0.35s, voxel-size=55x20x25mm3, averages/block=16). Before spectroscopy data acquisition, an anatomical image (M2PRAGE) and a short fMRI scan (3D-EPI) were obtained for accurate MRS voxel placement in the activated occipital area (Figure 1A). Participants were exposed to a visual stimulation task (24 min) consisting of alternating blocks of rest (4.8 min) and flashing checkerboard stimuli (4.8 min)3(Figure 1B), while fMRS spectra were collected from the visual cortex (Figure 2). In the rest condition, a black screen with a colored fixation dot was used. In both conditions, the fixation dot changed color 4x a block. The participants were asked to respond to the color change with a button press (response rate). FMRS data preprocessing was performed using in-house MATLAB scripts. A concentration quantification analysis was performed using LCModel software to estimate NAD+(H) and other 31P metabolites levels1.

Results: Two participants had to be excluded based on button presses during the experiment (<18 out of 20), one because of excessive motion, resulting in eleven datasets. The preliminary results indicate that, even though not significant, the fMRS measurements successfully captured dynamic changes in PCr, Pi, and NAD+ levels during the visual stimulation task (Figure 2A). The spectra were of good quality (mean FWHM=0.06ppm, SNR=7.3 for a measurement block of 6 transients). So far, results demonstrated no significant main effect of stimulation vs. rest blocks in PCr, Pi, NAD+ and PCr/Pi concentrations ($p>0.05$)(Figure 2A). Analysis of the average concentration over all rest blocks and stimulation blocks also did not show significant differences for PCr, Pi NAD+ and PCr/Pi ($p>0.05$).

Discussion/Conclusion: The present study provides evidence for the feasibility of measuring NAD+ dynamics in the occipital lobe using 31P functional MRS during a visual stimulation task. Even though non-significant, changes between stimulation and rest blocks were visible in the current piloting phase. The results should be confirmed with bigger sample sizes. Changes in the investigated metabolite concentrations would indicate enhanced energy production and utilization in response to visual stimulation, supporting the notion of a task-related metabolic demand.

References:

1) Cuenoud, B., Ipek, Ö., Shevlyakova, M., Beaumont, M., Cunnane, S. C., Gruetter, R., & Xin, L. (2020). Brain NAD Is Associated With ATP Energy Production and Membrane Phospholipid Turnover in Humans. Front Aging, 12.
2) Xin, L., Ipek, Ö., Beaumont, M., Shevlyakova, M., Christinat, N., Masoodi, M., Greenberg, N., Gruetter, R., & Cuenoud, B. (2018). Nutritional Ketosis Increases NAD+/NADH Ratio in Healthy Human Brain: An in Vivo Study by 31P-MRS. Front Nutrition, 5.
3) Barreto, F. R., Costa, T. B. S., Landim, R. C. G., Castellano, G., & Salmon, C. E. G. (2014). 31P-MRS Using Visual Stimulation Protocols with Different Durations in Healthy Young Adult Subjects. Neurochem. Research, 39(12)

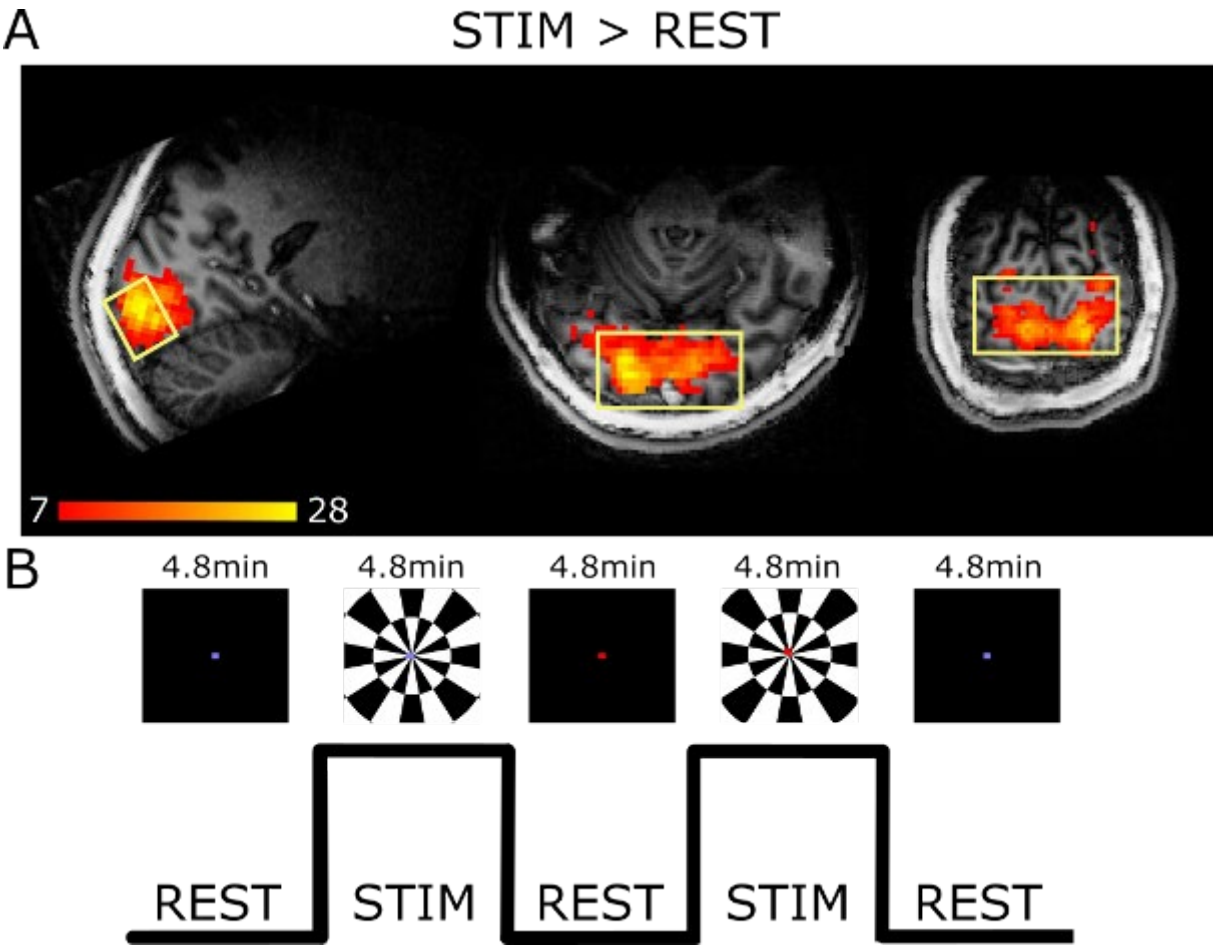

Figure 1: Study design. A) A representative activation-map of the stimulation>rest contrast (red/yellow) and a representative voxel (yellow) are overlaid on a representative anatomical image. B) The schematic representation of the experiment. As visual stimulation checkerboards were used, in the rest condition a black screen with a fixation dot was used. In both conditions, the fixation dot changed color four times a block. The participant was asked to respond to the color change with a button press.

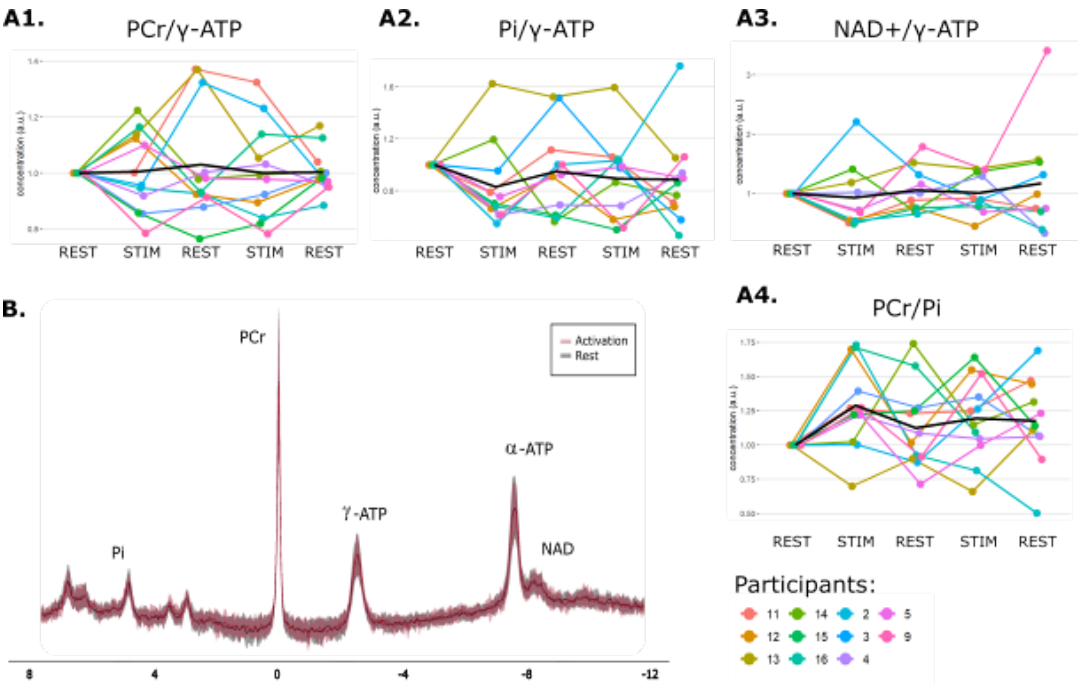

Figure 2: A) Individual concentration changes per rest and activation block of: 1) PCr 2) Pi and 3) NAD+ 4) PCr/Pi. B) Mean spectrum across subjects averaged across transients and blocks (line) with standard deviation (shading), during the stimulation (red) and rest (black).

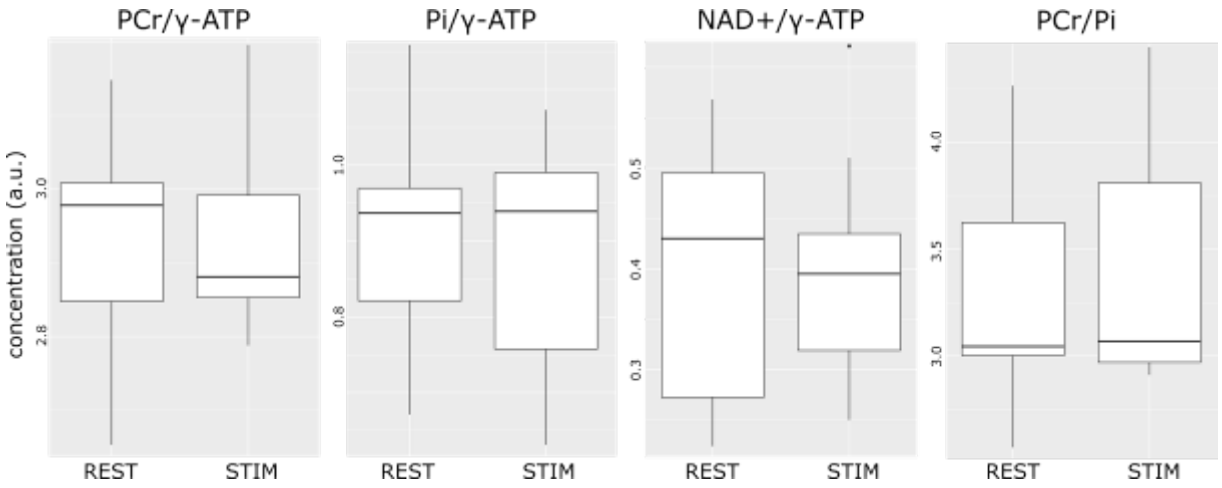

Figure 3: Barplot of the concentrations of PCr, Pi, NAD+, and PCr/Pi averaged over all rest and activation blocks.

LB286.

Evaluating the performance of fully endogenous molecular probes for imaging cerebral metabolism

F. Anvari Vind[1], T. P. Lê[1], A. Capozzi[1,2], M. Mishkovsky[1]

[1]EPFL, Laboratory for Functional and Metabolic Imaging (LIFMET), Lausanne, Switzerland
[2]Technical University of Denmark, Health Technology Department, Kgs Lyngby, Denmark

Introduction: Recent developments in photo-induced non-persistent radicals for dDNP have opened opportunities to reduce the delay between the preparation and injection of hyperpolarized (HP) substrates by avoiding the need to filter filtering of potentially toxic radicals[1–3]. Moreover, the non-persistent nature of the DNP polarizing agent combined with careful control of the magnetic field and temperature at which the sample is exposed represents, as of today, the most efficient approach to transport HP contrast agents [4–6]. Those steps are critical for allowing the translation of HP probes from mice to men. In particular, this technology will ease the employment of compounds with short hyperpolarization lifetime such as ^{13}C-glucose[7–9]. The present abstract is related to the in vivo implementation of probes hyperpolarized with endogenous non-persistent polarizing agents.

Methods:

Hyperpolarizing glucose with UV induced radicals:

Frozen beads prepared by pouring in liquid nitrogen 6 uL droplets taken from a stock solution of 64 mg [$^{2}H_7$, U-$^{13}C_6$]glucose, 16.5 mg alpha-ketoglutarate (aKG), and 128 mg 1:1 water glycerol (w/w) solution were exposed to UV light (deuterium lamp working at 40 W/cm^2) for 300 s to generate enough radical concentration to perform efficient DNP at 7 T and 1 K [1,5]. The irradiated sample was then loaded into a home-built DNP polarizer[10,11]. Microwave frequency sweeps were performed, with and without frequency modulation, to find optimal DNP conditions. Polarization levels were calculated, after dissolution in 4.5 mL superheated D_2O of a sample of 12 beads (approx. 72 uL), at a 9.4T MR scanner by comparing the HP solution carbon signal to its thermal equilibrium one, after complete relaxation.

In vivo MR measurements:

Spectra were acquired in a 9.4T MRI system (Varian/Magnex) using a home-built quadrature ^{1}H-coil/^{13}C surface coil that was placed on top of the mouse head. Brain metabolism of HP glucose was monitored in a group of 12h-fasted male C57BL6/J mice (n=3). Mice were kept under isoflurane 1.3-1.6% during a surgical procedure to place a femoral catheter for the bolus injection. Then, the anesthesia was switched to a combination of medetomidine (0.3 mg/kg bolus followed by 0.03 mg/kg/h i.v.) and isoflurane (0.25-0.5%) one hour before injection of HP [$^{2}H_7$, U-$^{13}C_6$]D-glucose. To monitor real-time de novo synthesis of [1-^{13}C]lactate, a 540 uL of HP solution, generated as previously described using 25 beads (approx. 150 uL), was injected through the femoral vein. A sequence of pulse-acquire was triggered 5.5s post-injection with 25° frequency selective Gaussian pulse (250µs) centered at 182 ppm every 1s for 70s. Lactate-to-glucose ratio (LGR) was calculated from the summed spectra and compared to previously reported values[8] (Figure 2).

Results and Discussion: UV irradiation generated a radical concentration of 55±5 mM of radicals (Figure 1A). The optimal microwave parameters were found for an irradiation frequency of 196.7 GHz with frequency amplitude modulation of 50 MHz (Figure 1B). At these experimental conditions, the obtained liquid state polarization was 21.3±0.7% (integrating the signal around C2-C5 carbons) (Figure 1C). The production of lactate from the HP glucose could be detected in all spectra acquired in the mouse brains (Figure 2A). The LGR that were calculated were found similar to previously reported values with a trend of higher LGR when glucose was hyperpolarized with aKG radicals than Trityl (0.23±0.11 and 0.14±0.06 mean±SD respectively) (Figure 2B). Further investigation is needed to confirm this observation.

To conclude, here we show the first in vivo spectra of cerebral metabolism in the mouse brain following the injection of radical-free HP glucose solution. This preparation leads to a similar metabolic response that was reported for HP glucose that was polarized with stable persistent radicals.

References

(1) Capozzi, A.; et al. *Angewandte Chemie International Edition* **2019**, *58* (5)
(2) Eichhorn, T. R.; et al. *Proc Natl Acad Sci U S A* **2013**, *110* (45)
(3) Gaunt, A. P.; et al, *Angewandte Chemie* **2022**, *134* (2)
(4) Capozzi, A.; et al, *Nat Commun* **2017**, *8* (1), 15757
(5) Capozzi, A.; et al, *Commun Chem* **2021**, *4* (1), 1–11.
(6) Capozzi, A. *Sci Rep* **2022**, *12* (1), 19260
(7) Mishkovsky, M.; et al *Sci Rep* **2017**, *7*, 11719
(8) Flatt, E.; et al, *Metabolites* **2021**, *11* (7)

(9) Mishkovsky, M.; et al, *Sci Rep* **2021**, *11*, 5771.
(10) Cheng, T.; et al, *Physical Chemistry Chemical Physics* **2013**, *15* (48), 20819–20822
(11) Comment, A.; et al, *Concepts in Magnetic Resonance Part B: Magnetic Resonance Engineering* **2007**, *31B* (4), 255–269

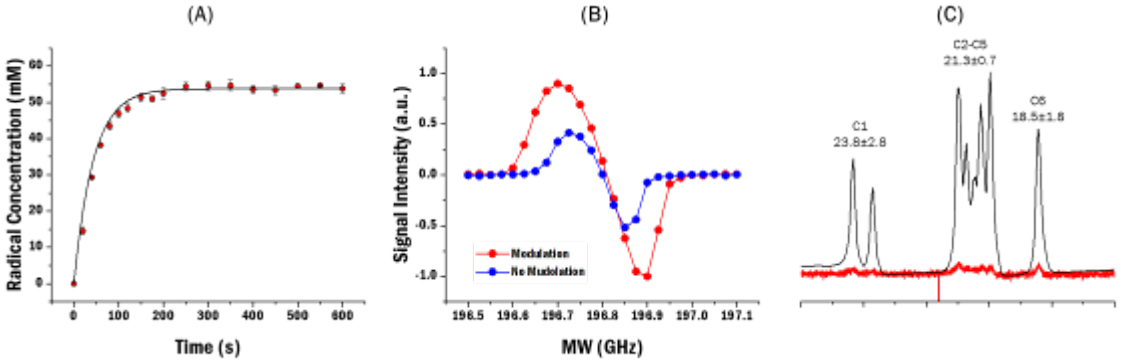

Fig 1. Hyperpolarizing glucose with UV-induced radicals from aKG in a 7T/1K polarizer. (A) Radical Concentration of one 6 uL bead as a function of UV irradiation time at 77K. The Radical Concentration is computed using the calibration coefficient found in TEMPOL calibration (n = 3). (B) Microwave sweep at 1K with (red) and without (blue) microwave modulation to define to optimal frequency for hyperpolarization. (C)HP signal (black) and thermal signal magnified by a factor of 20 (red) from the same sample and the corresponding polarization levels at the carbon position (n =3).

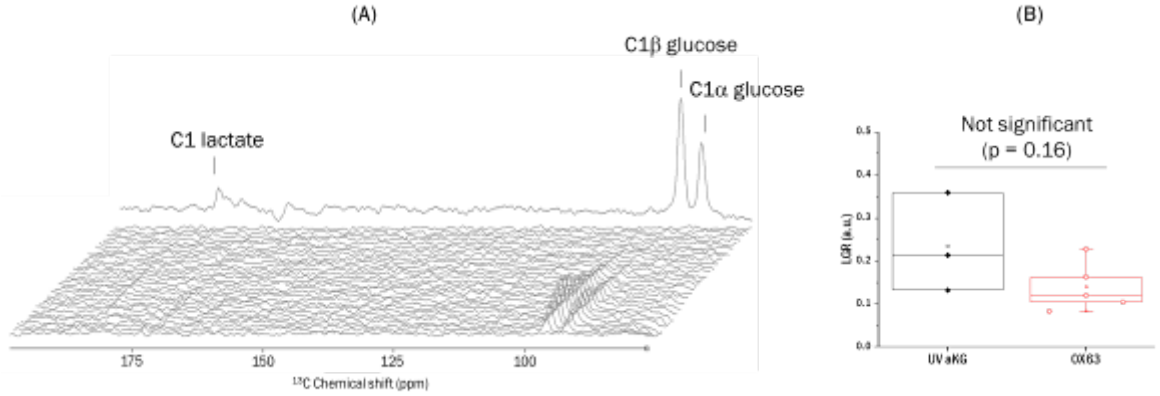

Fig 2. Cerebral metabolism glucose polarized with UV-induced polarizing agents: (A) Typical time course and summed spectra (top). (B) The lactate-to-glucose (LGR) ratios that were calculated in mice receiving HP glucose by aKG radicals (black full diamonds) and previously reported LGR forref 8 (red circles).

LB287.

In vivo CEST MRI with natural D-glucose as a contrast agent to evaluate and detect myocardial infarction in comparesion to late Gd-enhancement

A. Peddi[1], D. Schache[1], A. Nahardani[2], M. Kuhlmann[3], M. Wildgruber[4,1], C. Faber[1], V. Hörr[2,1]

[1]Universitätsklinikum Münster, Translational Research Imaging Center, Clinic of Radiology, Münster, Germany
[2]University Hospital Bonn, Heart Center Bonn, Department of Internal Medicine II, Bonn, Germany
[3]University of Münster, European Institute for Molecular Imaging, Münster, Germany
[4]University hospital of München, Clinic and Polyclinic for Radiology, Munich, Germany

Introduction: Myocardial infarction (MI), a major cause of mortality in affluent countries, underscores the imperative for advancing non-invasive imaging techniques to improve the accuracy of diagnosis and particularly prognoses[1]. However, sophisticated MRI techniques frequently require chemical contrast agents to visualize the structural and morphological changes of the heart[2]. Thereby the commonly applied contrast agent of gadolinium (Gd) chelates may show toxic properties, especially in patients with kidney impairment[3].

Thus, the goal of this study was to explore the application of natural D-glucose as an infusible biodegradable MRI contrast agent for imaging of MI region by glucose-weighted CEST MRI (glucoCEST).

Method:

Animal study: The study used two groups of 8-week-old C57BL/6 male mice: healthy mice (n = 9) and mice with MI (n = 5). Through the procedure of a left thoracotomy followed by the permanent ligation of the left coronary artery, MI was induced[4]. In vivo MRI and ex vivo examination (TTC; triphenyl tetrazolium chloride and H&E; hematoxylin and eosin staining)[5] were carried out on day 7 post surgery.

In-vivo MRI: MRI experiments were conducted on a 9.4 T Bruker BioSpec 94/20 system (Ettlingen, Germany), equipped with a 1 T/m gradient system, a 35-mm volume resonator coil and ParaVision 6.0.1 operating software. Animals were anesthetized with isoflurane (1.5% - 2.5% isoflurane and 0.7/0.3 air/O2 mixture). CEST experiments were carried out using a modified cardiac and respiratory triggered FLASH sequence containing a CEST saturation module (Figure 1). Right before glucoCEST MRI, animals received two intraperitoneal injections of glucose/PBS solutions (1.0 M and 1.5 M) with a 25-minute interval.

For T1 mapping, T1-weighted images at variable flip angles were acquired by an IntraGate (IG)-FLASH sequence and data were fitted according to Figure 2C. Late Gd-enhanced (LGE) MRI was performed 8 minutes after intravenous injection of 0.1 M Gadovist.

CEST MRI data analysis: For each voxel a z-spectrum was plotted, smoothened, and corrected for B0 inhomogeneities and the asymmetric magnetization transfer ratio (MTRasym) was computed. The glucoCEST MTRasym contrast was quantified by integration over the offset range from 0.5 to 2.0 ppm and was averaged for each ROI.

Statistical analysis: All statistical calculations were performed by Mann-Whitney-U-Test.

Results: In animals with MI, the MI region was identified by late Gd-enhanced MRI through significantly shortened T_1 relaxation times (Fig. 2A-D), and was further corroborated via macroscopic (Fig. 2EI-2EII) and microscopic evaluation (Fig. 2EIII-EIV). In pixelwise calculated glucoCEST MTR_{asym} maps, healthy and MI animals exhibited marked differences of the heart across the three distinct myocardial regions of healthy myocardium (healthy animals), MI region, and remote myocardium (MI animals) before and after glucose infusion (Fig. 3A-C). In healthy animals, the corresponding glucoCEST MTR_{asym} spectra of the myocardium showed reduced values after glucose infusion (Figure 3A). In contrast, in MI animals, the glucoCEST MTR_{asym} values of MI regions were increased substantially (Figure 3B) while no notable changes were observed in the remote myocardium (Figure 3C). Statistical analysis by Mann-Whitney-U-Test confirmed the differentiation between MI region, remote myocardium, as well as healthy myocardium based on the glucoCEST contrast changes before and after glucose infusion (Fig. 4).

Discussion: Our study found a notable increase in glucoCEST contrast inside the MI area after glucose infusion, although ^{18}F-FDG-PET experiments commonly show reduced signal intensities within infarct zones relative to remote myocardium[6]. Unlike ^{18}F-FDG-PET, which detects the metabolic turnover of glucose, the observed glucoCEST contrast predominantly originates from unaltered glucose which accumulates after the glucose infusion in tissues with diminished or altered glucose utilization, such as MI, similar to LGE MRI. However, in contrast to ^{18}F-FDG-PET,

glucoCEST contrast does not only represent metabolic activity but also detects perfusion-related aspects such as blood volume, vascular leakage, and extracellular space[7] and thus reflects a combination of glucose utilization and circulatory function with glucose washout.

Conclusion: GlucoCEST MRI using D-glucose as a biodegradable contrast agent, could clearly differentiate between infarct regions and remote myocardium in animals with MI.

Refences:

1) Li, H. et. al. Front Physics. 8, 1–26, 2020.
2) Danad, I. et. al. JAMA Cardiol. 2(10):1100-1107, 2017.
3) Vandsburger, M. et. al. Circ Cardiovascular Imaging. 8(1), 1–8, 2014.
4)Kuhlmann, M. T. et. al. J Exp Med. 203(1), 87–97, 2006.
5)Protti, A. et. al. J Am Heart Assoc. 4(8), e001851, 2015.
6) Vasudevan, P. et. al. Int J Mol Sci. 21(9):3340, 2020.
7) Masoud, W. G. T. et. al. Cardiovasc Res. 101(1), 30–38, 2014.

Parameters	FLASH (glucoCEST)	Ig FLASH (LGE MRI)
Filp angle	15°	14°, 11°, 8°, 5°, 2°
TE/TR	2.3/398 ms	1.7/5.8 ms
FOV	30x30 mm^2	30x30 mm^2
Slice thickness	1 mm	1 mm
Matrix	96 x 96	128 x 128
Averages	2	1
Magnetization transfer module	Block pulse, T_{sat} =140 ms, B_1=2 μT	-
Saturation offset range	±5 ppm	-
Saturation steps	200 Hz (21 steps in total)	-
S_0 offset	+15 ppm	-
Approximate scan time	20 min	3 min

Fig.1: MRI sequences and parameters.

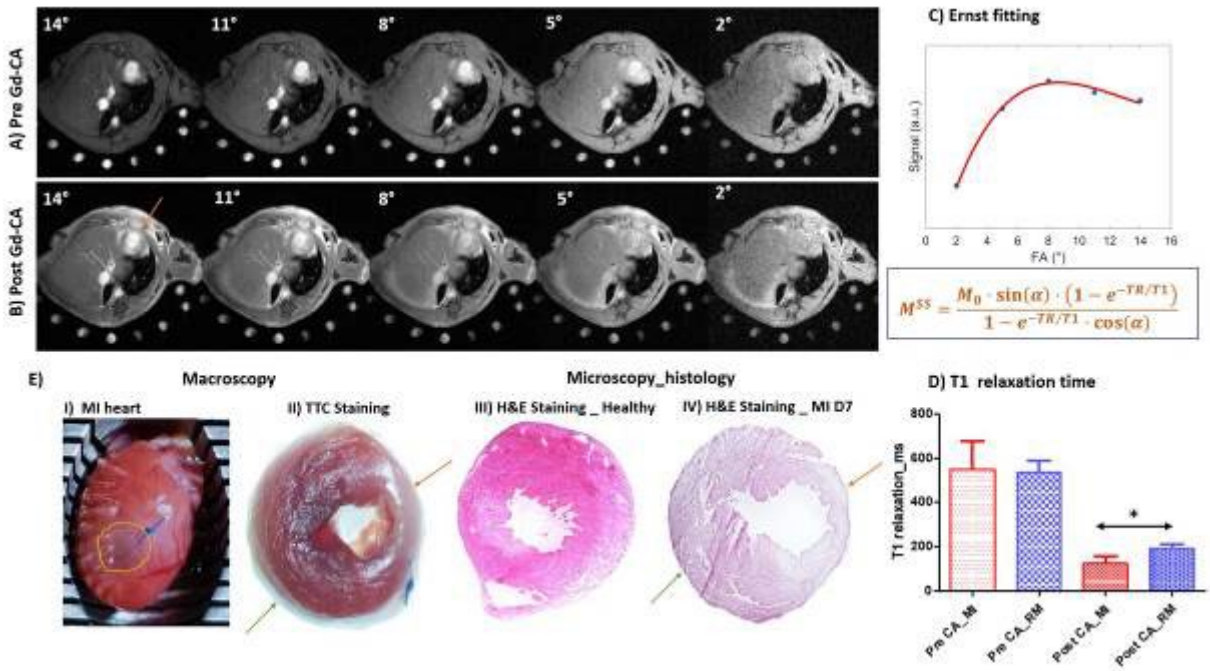

Fig.2: A) + B) T_1 weighted MRI series with variable flip angles A) pre and B) post contrast agent (Gd-CA) in a representative healthy animal and animal with MI on day 7 (D7) post surgery. C) Fitting of the signal intensity to the Ernst equation to calculate T_1 relaxation times. D) T_1 relaxation times in MI region and remote myocardium (RM) pre and post contrast agent (Gd-CA). E) Macroscopic (I-II) and microscopic (III-IV) illustration of MI region using TTC and H&E staining, respectively. MI region:red, RM:green.

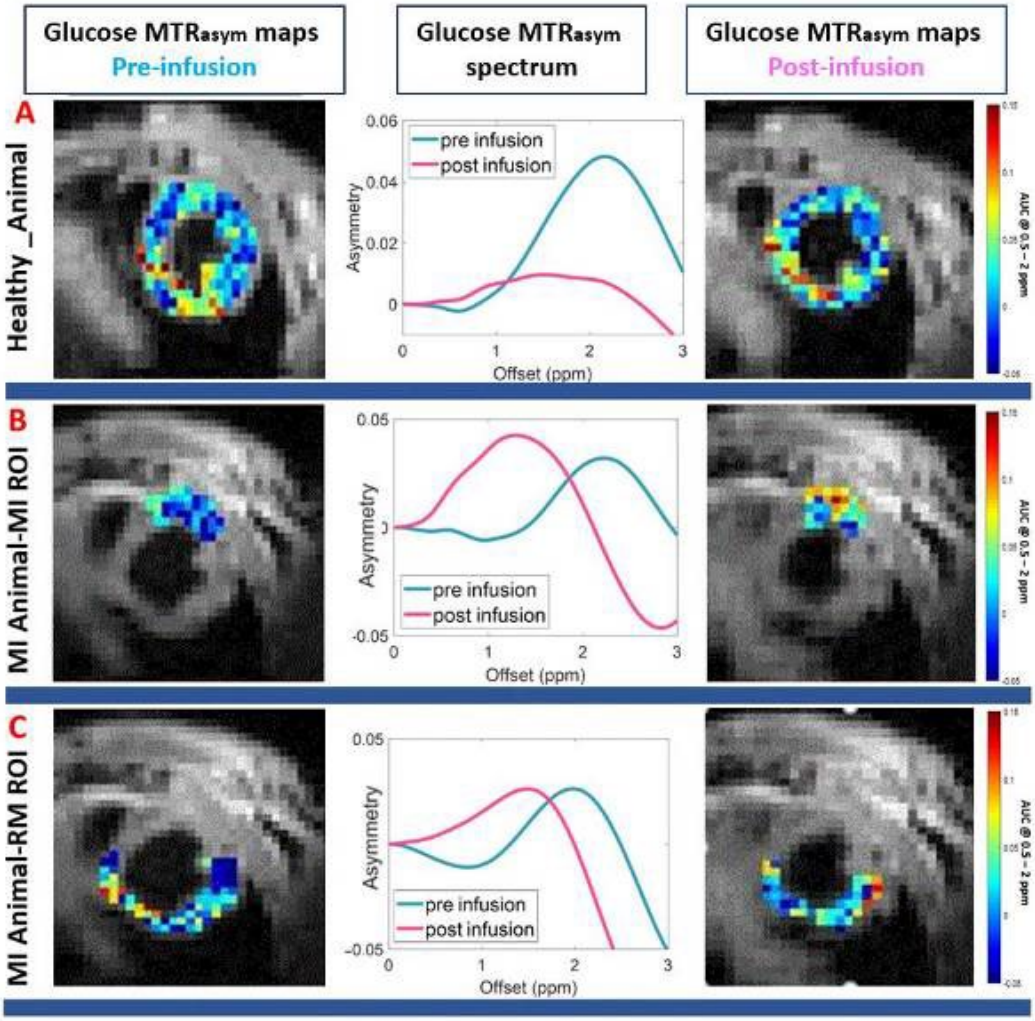

Fig.3: Representative in vivo glucoCEST MTR_{asym} spectra and contrast in A) healthy myocardium, B) MI region and C) remote myocardium (RM) pre and post glucose infusion.

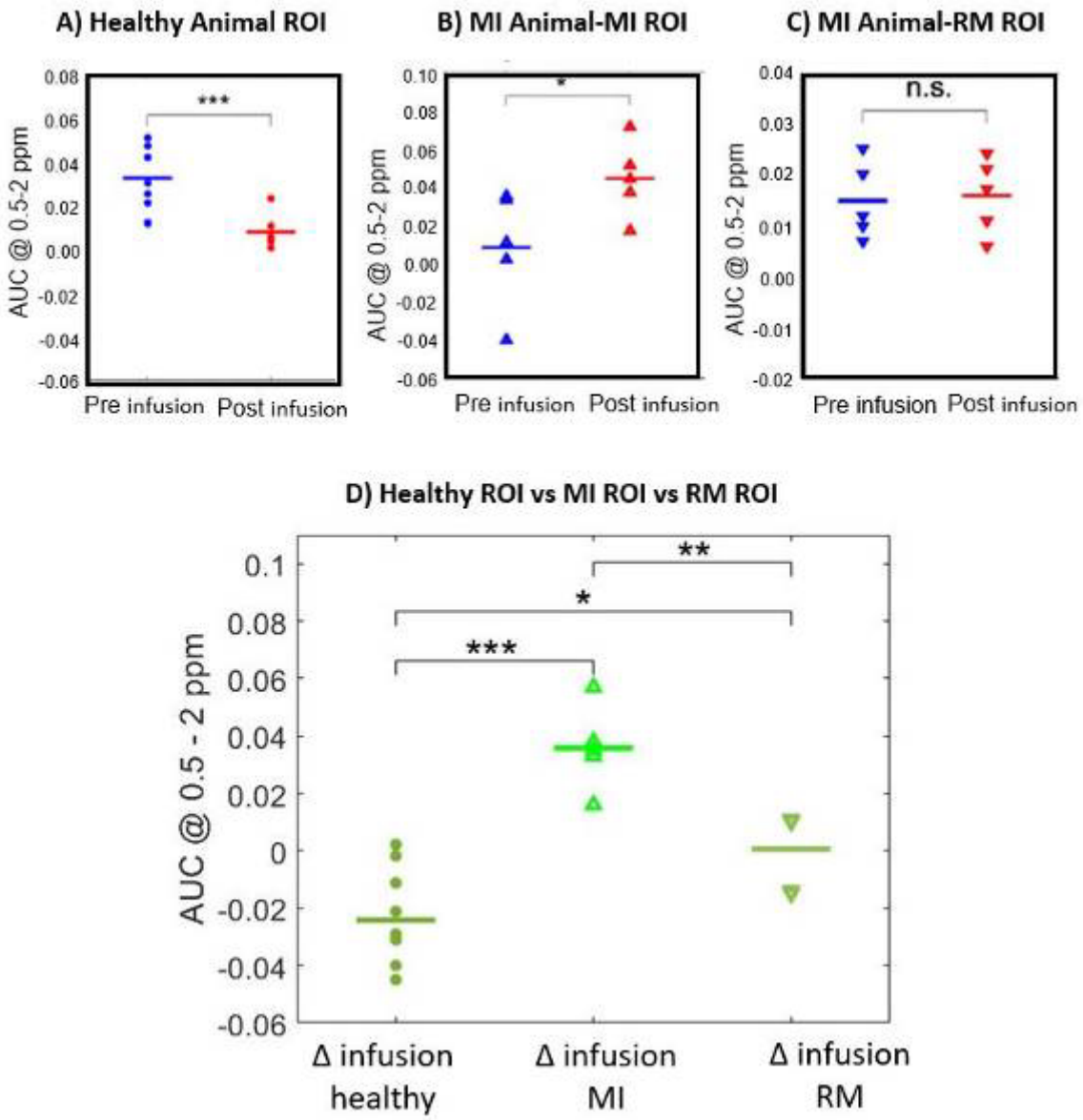

Fig.4: Mann-Whitney U-Test of glucoCEST MTR_{asym} contrast pre and post glucose infusion in A) healthy myocardium, B) MI region and C) remote myocardium (RM) as well as D) significant differences in glucoCEST contrast between all three ROIs. *p<0.05,**p<0.01, ***p<0.001.

LB288.

Simultanous DCE- and DSC-MRI with blind deconvolution - comparison of gradient-correction and pharmacokinetic models

R. Jirik[1], O. Macicek[1], J. Vitous[1], L. Kratka[1], E. Drazanova[1], M. Vojnikova[2,3], L. Sivak[3], A. D. Miller[3], Z. Heger[3], Z. Starcuk[1]

[1]Czech Academy of Sciences, Institute of Scientific Instruments, Brno, Czech Republic
[2]Brno University of Technology, Central European Institute of Technology, Brno, Czech Republic
[3]Mendel University in Brno, Department of Chemistry and Biochemistry, Brno, Czech Republic

Introduction: Combination of DCE- and DSC-MRI might be a way to improve the diagnostic value of these techniques. Using multi-gradient-echo (MGE) acquisition, DCE and DSC data can be acquired simultaneously. After fitting the DCE data with a pharmacokinetic (PK) model, contrast-agent (CA) concentration curves for the intra- and extra-vascular space can be estimated for each region of interest. A gradient-correction (GC) model is then formulated using these curves and r2*-relaxivity-related parameters. The GC model is then fitted to the DSC data. The r2*-related parameters can be treated as additional perfusion parameters reflecting the microvascular structure [1].

Alternatively, the sequential approach can be replaced by a simultaneous approach, where the PK and GC models are fitted to the DCE and DSC data simultaneously, so that the PK-model fitting is better posed (the DSC data linked with the DCE data through the GC model constrain the possible solutions), as shown in [2] on simulated data.

The additional information included in the DSC signal can also be used to estimate the arterial input function (AIF, part of the PK model) using blind deconvolution more accurately than from DCE alone, as shown in [3] on synthetic and phantom data.

So far, the above mentioned advantages of simultaneous DCE-DSC have not been shown on real data. Also, different versions of PK and GC models have not been compared on real data to show how realistic they are.

Methods: Five tumor-bearing mice (subcutaneously implanted 4T1 tumor cells) imaged with a 9.4T Bruker Biospin scanner (Ettlingen, Germany) using a 2D golden-angle (GA) MGE sequence (TR/TE=23/1.4, 3.4, 5.4, 7.4, 9.4, 11.5, 13.5, 15.5 ms, FA = 30°, 1 axial slice, 128 samples/projection, acquisition time 15 min) and a 2D IR GA precontrast sequence for T10 estimation [4] for conversion of DCE images to CA-concentration images. Gadovist (Bayer HealthCare, Germany) was administered into the tail vein, dose 0.2 mmol/kg. Experiments were approved by the National Animal Research Authority.

The precontrast and MGE images were reconstructed using the BART toolbox [5]. A tumor region was drawn manually and its voxels were K-means clustered into 10-20 clusters (according to the tumor size) based on their curves for all TEs. Upon manual removal of clusters with corrupted centroid curves, each cluster's centroid curve was converted to DCE and DSC signals $\Delta R1(t)$, $\Delta R2^*(t)$ using exponential fitting of the multi-echo samples and conversion of the DCE part from the signal-intensity domain to CA concentration.

To provide an accurate AIF, simultaneous fitting of the PK and CG models to the DCE and DSC signals of the clusters was incorporated in blind deconvolution in an alternating optimization, switching between updating the PK+GC model parameters and the parameters of the AIF [3]. This was repeated for all combinations of the PK models (2CX, ATH, DCATH) and GC models (GC1 [1], GC2 [6], GC3 [7]; GC1 and GC2 are parametrized by two, GC3 by three r2*-related parameters). The Akaike information criterion (AIC) was then calculated.

Results: The AICs (Fig.1) suggest that the 2CX model is the most appropriate PK model in this case. For animals 1 and 2, GC1 was the best CG model, while in other animals the AICs were comparable suggesting similar performance for all tested GC models. The most relevant dataset was from animal 1 because of higher signal-to-noise ratio (SNR), larger tumor size and higher heterogeneity, compared to the other animals. Example curves from this animal (Figs. 2, 3) show clear superiority of 2CX and comparable fits for the different GC models. In addition, Fig. 4 shows examples where sequential DCE-DSC analysis fits the DCE signal well but with wrong PK-model parameters (due to the ill-posedness of the DCE fitting problem), revealed by the bad fit of the corresponding DSC signal. On the other hand, simultaneous analysis fits both signals well, indicating the correct solution.

Discussion: To draw stronger conclusions, a larger set of high-SNR recordings needs to be analyzed. The model comparison was limited to the 4T1 tumor. The AIC criterion reflects not only the realism of the models but also the difficulty of the fitting problem - this was minimized by fitting from several starting points.

Conclusion: We have shown that simultaneous DCE-DSC analysis within blind deconvolution can model the DCE and DSC curves accurately. We have shown cases where this method can resolve the ill-posedness of the DCE model-fitting problem. Out of the tested models 2CX seems to be the most realistic. The GC were comparable, with slight preference for GC1.

References

[1] S Sourbron et al 2013 MRM 69 1430
[2] M Macicek et al 2017 ISMRM Proc. 136
[3] M Macicek et al 2022 ISMRM Proc. 1583
[4] J Vitous et al accepted in MRM 2023
[5] https://doi.org/10.5281/zenodo.7110562
[6] S Sourbron et al 2009 MRM 62 672
[7] C C Quarles et al 2009 Phys. Med. Biol. 54 5749

Animal 1

	PK model		
GC model	2CX	ATH	DCATH
GC1	1195,6	1678,9	1681,3
GC2	1207,9	1692,9	1714,5
GC3	1351,5	1607,1	1718,7

Animal 2

	PK model		
GC model	2CX	ATH	DCATH
GC1	696,8	809,4	753,9
GC2	741,2	814,5	830,7
GC3	726,8	792,1	767,4

Animal 3

	PK model		
GC model	2CX	ATH	DCATH
GC1	599,3	678,8	627,7
GC2	599,6	687,7	630,0
GC3	598,7	671,5	629,1

Animal 4

	PK model		
GC model	2CX	ATH	DCATH
GC1	746,5	792,8	791,5
GC2	746,6	794,7	790,3
GC3	748,3	794,1	784,4

Animal 5

	PK model		
GC model	2CX	ATH	DCATH
GC1	657,4	641,9	662,7
GC2	644,1	643,1	665,8
GC3	642,8	636,4	666,3

Fig. 1. Table of Akaike information criterions for all model combinations and all animals. Red - lowest AIC (best model), orange - second lowest AIC (second best model), blue - third lowest AIC (third best model).

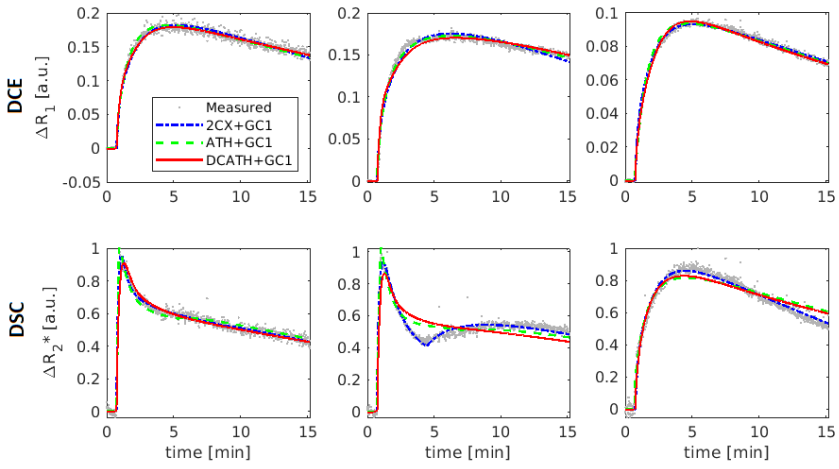

Fig. 2. Selected DCE and DSC curves (converted mean curves of three clusters of animal 1). Comparison of PK models.

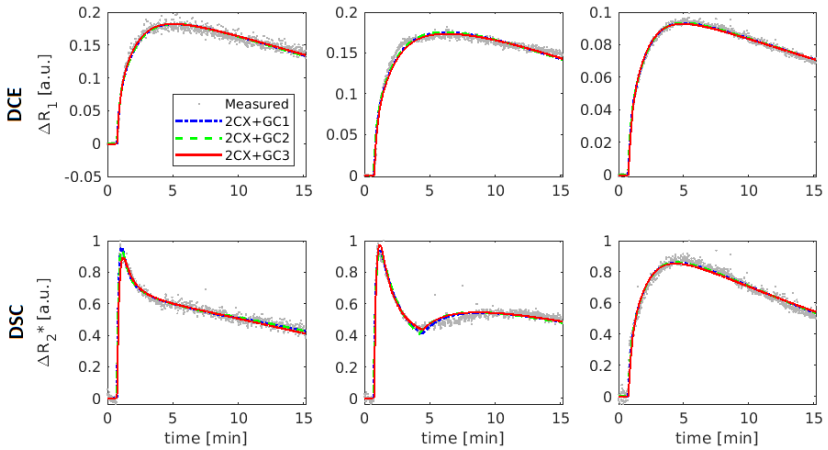

Fig. 3. Selected DCE and DSC curves (converted mean curves of three clusters of animal 1). Comparison of GC models for the 2CX PK model.

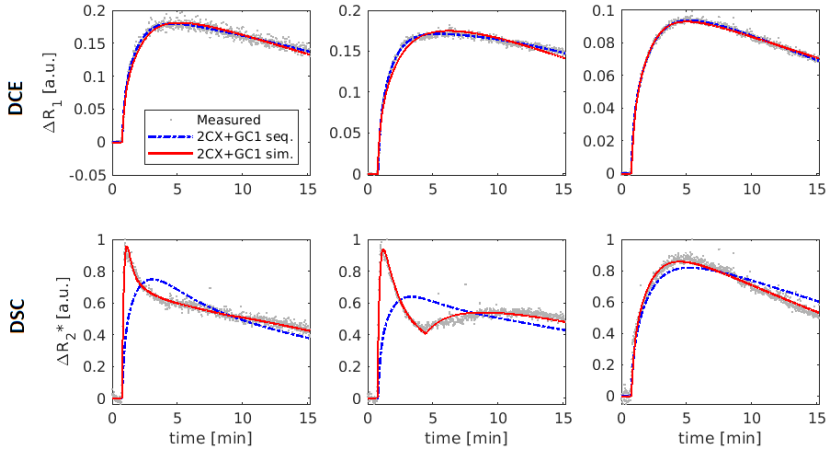

Fig. 4. Selected DCE and DSC curves (converted mean curves of three clusters of animal 1). Comparison of the sequential (seq.) and simultaneous (sim.) DCE-DSC analysis. Both seq. and sim. fit the DCE curves well (both model curves overlapping; however with very different PK parameters). Only sim. fits also the DSC curves well, i.e. only the PK parameters of the sim. approach are correct.

LB289.

Optimization of magnetic susceptibility quantification in the context of Parkinson's disease: validation on test-objects and healthy volunteers

A. Hervouin[1], J. Bezy-Wendling[1], F. Noury[1]

[1]University of Rennes, LTSI -Inserm UMR1099, Rennes, France

INTRODUCTION: *In vivo* quantification of iron in deep gray nuclei (DGN) represents a new neuromarker to understand the mechanisms of the Parkinson's disease (PD). To this end it is possible to exploit the magnetic susceptibility (MS) of DGN, by reconstructing MS maps using quantitative susceptibility mapping (QSM) methods. The aim of our study was to compare the accuracy of QSM pipelines (pip). We worked with a standard multi-gradient-recalled-echo (MGRE) sequence with eight echoes, widely used at 3 T in clinical research. Since there is great variability in DGN MS quantification in the literature, our strategy was to work first with test-objects (TO) that we can control, then on data acquired in healthy volunteers (HV).

METHODS: Two TO were created from solutions of Dotarem® (Gadoterate Meglumine; 0.5 mmoL.ml-1; Guerbet; France): TO-DGN (0.003<MS<0.196 ppm) and TO-HMS (0.033<MS<3.260 ppm). Sixteen HV with no history of neurological disorder were recruited from 2021 to 2023 (Clinical trial NCT05107232; Univ. hospital of Rennes) and the written informed consent from all participants was obtained. Two groups were constituted: the senior-adults group (SAG; n=8; sex ratio=1; age=46,8±4,5 years) and the young-adults group (YAG; n=8; sex ratio=1; age=23,6±1,3 years).

MRI data acquisition: For TO, susceptibility-weighted images (SWI) were acquired at 1.5 T (Magnetom; Avanto; Siemens; Erlangen; Germany) using an ankle coil. A 3D monopolar MGRE sequence was used (Voxel=(1.64 mm)^3; Bandwidth=200 Hz/pixel; 8 echoes; TR=72 ms; TEmin/ΔTE=7/6 ms; FA=20°; Tacq=4"12"). Acquisitions were repeated five times for each TO, during different MRI sessions. For HV, images were acquired at 3 T (Magnetom Prisma VE11C; Siemens Healthineers; Erlangen; Germany) using a 64-channels head coil. The protocol included 3D anatomical T1 and T2-weighted images (T1w and T2w) with a spatial resolution of (1 mm)^3 to segment the DGN of interest. SWI were acquired using a 3D monopolar MGRE sequence (Voxel=(1.5 mm)^3; Bandwidth=200 Hz/pixel; TR=55 ms; TEmin/ΔTE=3.6/5.9 ms; FA=15°; Tacq=6"31"").

Image Processing: Reconstructions of MS maps from SWI were computed on Matlab (v2017Rb) using Sepia[1] (v1.1.1). Nine combinations of algorithms were compared for the phase unwrapping, background field removal and field to susceptibility inversion (Table 1). For TO, the FSL brain extraction tool[2] was manually settled to adapt it. The ImageJ (v1.53g; National Institute of Health) software was used to quantify the mean MS values and standard deviation (SD) of each manually traced ROI on MS maps. For HV, six regions per hemisphere were segmented from the T1w image using the *recon-all* process of FreeSurfer[3] (v7.2.0) (caudate nucleus (CN), putamen (Put), globulus pallidus (GP)), and from the T2w image using pBrain[4] (substantia nigra, red nucleus and subthalamic nucleus (STN)). The mean MS values and SD of each DGN were quantified using 3D Slicer (v4.11). A statistical analysis using a non-parametric U-test of Mann-Whitney was performed to compare the MS values in each DGN between the YAG and SAG.

RESULTS: Fig. 1-left shows the MS maps for TO-DGN. Pip 6 and 8 generated mistaken MS maps. Fig. 1-right shows linear regressions for the seven other pipelines. Based on calculations of relative error to theory[5] (slope=0.33), pip 1 is the most adapted to quantify this MS range (R^2=0.98, slope=0.27). For TO-HMS, pip 2 is the most adequate (R^2=0.89, slope=0.33) for this MS range and has lower relative errors than the others pipelines. For HV data, the pip 7 was excluded because of its blurry aspect (Fig. 2-left). Reliable MS maps were obtained for pip 1 and 4 to 9. For these pipelines, an increase of MS values with age was observed. The most accurate MS quantification was obtained with pip 4 (Fig. 2-right). A strong statistical difference between YAG and SAG was obtained for Put ($p<0.01$). CN, STN and GP displayed also significant differences ($p<0.05$).

DISCUSSION: The pipelines selected after comparing the different algorithms enabled us to obtain the expected theoretical MS values in TO-DGN and to quantify *in vivo* MS values in the DGN that are consistent with the literature. An increase of MS with age in all DNG was observed, as expected[6]. These preliminary results obtained in HV (n=16) need to be confirmed on a larger number of subjects.

CONCLUSION

This study shows the importance to optimize the image processing according to the application and the MS range targeted, in order to achieve accurate quantification. The perspective of this work will be to apply our methodology for

in vivo quantification of MS in DGN for PD patients, to explore the potential of this new neuromarker for monitoring PD progression and identifying various profiles of patients.

REFERENCES

[1]Chan KS, *NeuroImage* 227, 2021
[2]Smith SM, *Hum. Brain Mapp*. 17, 2002
[3]Fischl B, *NeuroImage* 62, 2012
[4]Manjón JV, *NeuroImage Clin*, 25, 2020
[5]Olsson E, *Radiol. Res.* Pract, 2018
[6]Guan X, NeuroImage 264, 2022

Pipeline	1	2	3	4	5[6]	6[7]	7[7]	8[7]	9[8]
Phase unwrapping	Laplacian MEDI[9]	Region Growing	SEGUE[10]	ROMEO[11]	Laplacian MEDI				Laplacian STI
Background field removal	PDF[12]		LBV[13]		V-SHARP	LBV		SHARP	V-SHARP
Field-to-susceptibility inversion	MEDI[9]				Star-QSM	MEDI	TKD	MEDI	iLSQR

Table 1: algorithms combinations used in the nine pipelines tested to reconstruct MS cartographies for both TO and HV. [6]Guan X, NeuroImage 264, 2022. [7]Santin MD, NMR Biomed. 30, 2017. [8]Wang C, Nat. Neurosci. 25, 2022. [9]Liu T, Magn. Reson. Med, 66, 2011. [10]Karsa A, IEEE Trans. Med. Imaging, 38, 2019. [11]Dymerska B, Magn. Reson. Med, 85, 2021. [12]Liu T, NMR Biomed, 24, 2011. [13]Zhou D, NMR Biomed, 27, 2014.

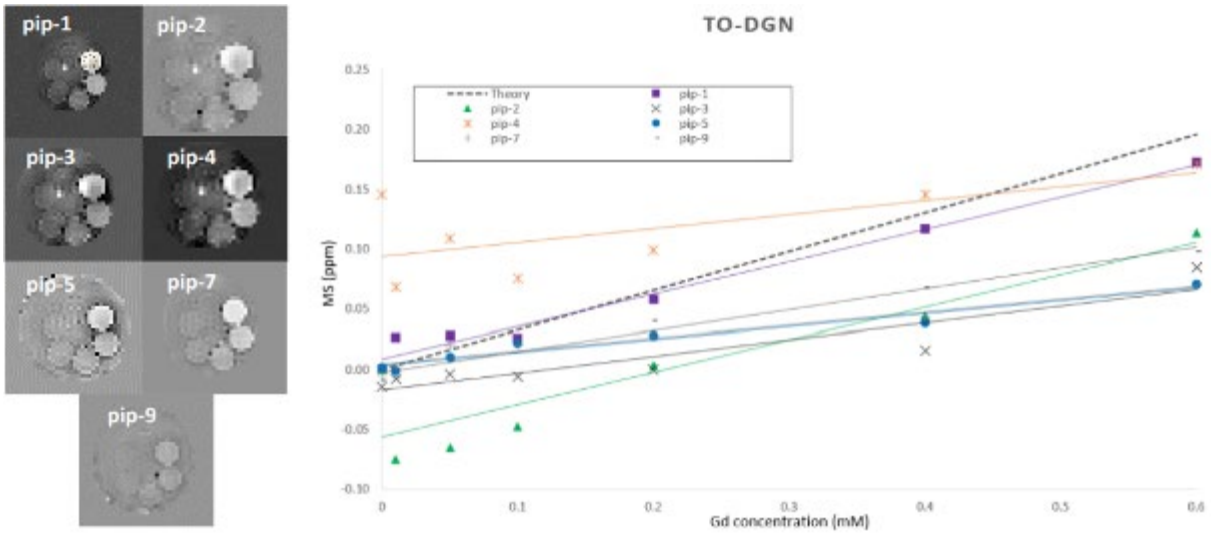

Fig. 1: MS maps (left) and linear regressions obtained on TO-DGN compared with theory (right).

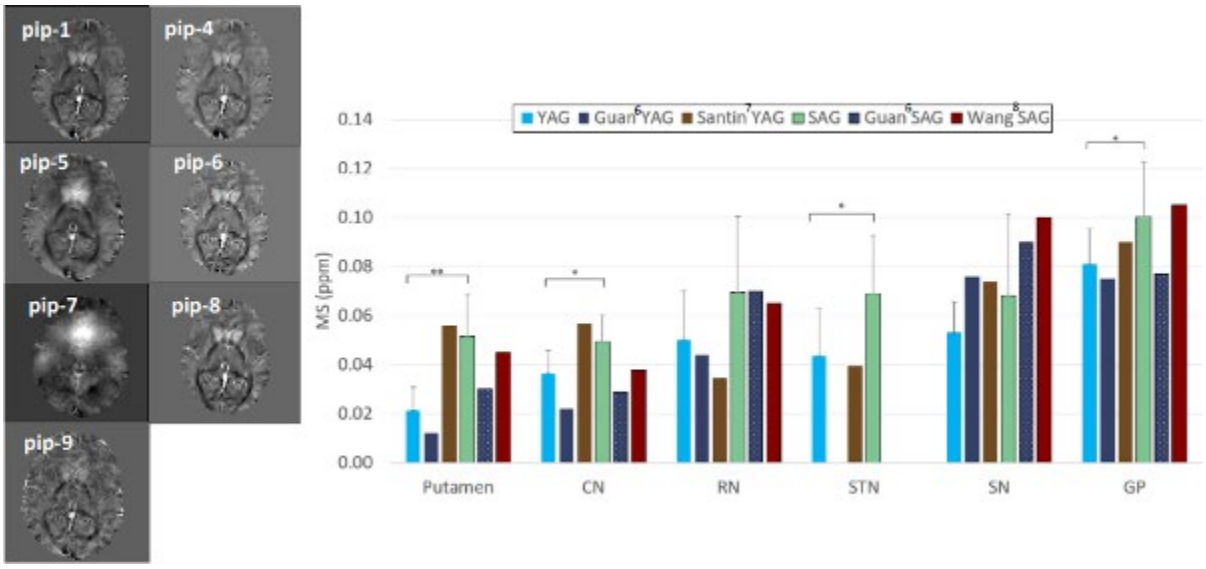

Fig. 2: example of MS maps reconstructed for one HV of the YAG (left) and MS quantification (mean, SD) on YAG and SAG for pipeline 4 (right). Our MS values are compared with literature ([6]Guan X, NeuroImage 264, 2022. [7]Santin MD, NMR Biomed. 30, 2017. [8]Wang C, Nat. Neurosci. 25, 2022). CN = Caudate Nuclei; RN = Red Nuclei; STN = Subthalamic Nuclei; SN = Substantia Nigra; GP = Globus Pallidus. *p<0.05, **p<0.01.

LB290.

Segmentation made simple: a three-click user interface for automated model (pre-) training and deployment

F. Santini[1,2,3], A. Agosti[4], K. Sharma[2], J. Periquito[2], K. K. Soe[2], K. M. Gooding[5], A. Forbes Brown[5], M. Gilchrist[5], M. F. Gomez[6], S. Sourbron[2]

[1]University of Basel, Basel Muscle MRI, Department of Biomedical Engineering, Basel, Switzerland
[2]The University of Sheffield, Division of Clinical Medicine, School of Medicine and Population Health, Sheffield, United Kingdom
[3]University Hospital Basel, Department of Radiology, Basel, Switzerland
[4]University of Pavia, Department of Mathematics, Pavia, Italy
[5]University of Exeter Medical School and NIHR Exeter Clinical Research Facility, Exeter, United Kingdom
[6]Lund University Diabetes Centre, Lund University, Department of Clinical Sciences, Malmö, Sweden

Introduction: Deep learning is considered the gold standard for automated or semi-automated semantic segmentation of medical images. However, the current workflow usually requires a considerable amount of curated initial training data and programming knowledge to make the model usable by the end user. Our free and open-source application Dafne (https://dafne.network) (1) alleviates these requirements by providing an interface for deep-learning-assisted segmentation which includes federated lifelong learning, allowing the models to learn from the usage. In this work, we are presenting a companion application, which, based on a limited number of training datasets, prepares and pretrains a model for a new segmentation task, and can easily be plugged into the Dafne federated ecosystem. The model trainer is available in source form at https://github.com/dafne-imaging/dafne-models and will also be released shortly as a stand-alone executable.

Methods: We generalized the existing 2D V-Net-based architecture of the current Dafne models (2) to become a generic model template with customizable hyperparameters, accepting arbitrary input resolutions and output classes, while keeping the integration with the user interface and the incremental and federated learning features. The developed model training application reads the training data packages (which can be generated from within Dafne), configures the model template accordingly, performs the necessary preprocessing steps (2), and fits the model. All the steps are automated, and the interface shows feedback on the progress to the user (Fig. 1). The fitting is stopped automatically when overfitting is detected. The fitted model is saved into a single file which can be imported into Dafne directly or installed onto a Dafne server.

The software was tested on coronal abdominal out-of-phase Dixon MR datasets with the kidneys segmented bilaterally, acquired as part of the iBEAt study (4). Approximately 50 to 60 slices of each dataset included the kidneys and were therefore used for the training. Three models were pretrained on 20, 30, or 40 datasets respectively (total number of datasets with a 10% training/validation split) on a standard Linux PC with 32GB of RAM and an NVIDIA GTX 1660 Ti GPU. The performance of each trained model was evaluated by calculating the average Dice coefficient between the automated segmentation and all the slices of four separate datasets used for testing.

Results: The training converged after 20 to 40 epochs for all three models. The most time-consuming step was the preprocessing of the images, which took 107 minutes for 40 datasets (2m40s per dataset on average, depending on the actual number of slices). The fitting took up to 38 minutes (40-dataset model). The testing resulted in an average Dice coefficient of 0.76 for both the 20 and 30-datasets models, and a Dice coefficient of 0.80 for the 40-dataset model (Fig. 2). The 40-dataset model will be released through the Dafne segmentation tool.

Discussion: The free and open-source application presented in this work makes generating and pretraining deep learning models for image segmentation possible without any programming knowledge. The models can be directly inserted into Dafne, which provides a convenient interface for performing, checking, and refining the segmentation. Dafne"s characteristic functionality is the continuous improvement of the models with usage, thus allowing initial training on a reduced number of datasets. The models produced are 2D, as the other Dafne models. While this might be suboptimal for some applications, it poses advantages in terms of incremental learning, as each dataset contains multiple slices which can be considered as separate data points.

Conclusion: The software presented here is a fully automated trainer for deep learning models capable of incremental learning, and can therefore be trained on a reduced number of datasets and subsequently refined during usage. The usage of this tool is very simple, requiring no programming knowledge, and thus enabling the creation of segmentation models for a wide range of applications.

Acknowledgment: Institutional and project funding: NIHR Exeter Clinical Research Facility (University of Exeter Medical School and Royal Devon University Healthcare NHS Foundation Trust). The iBEAt study has received funding from the Innovative Medicines Initiative 2 Joint Undertaking (JU) under grant agreement No 115974 (BEAt-DKD). The

JU receives support from the European Union"s Horizon 2020 research and innovation programme and EFPIA and JDRF. Any dissemination of results reflects only the author's view; the JU is not responsible for any use that may be made of the information it contains.

References

1. F. Santini et al., doi:10.48550/arXiv.2302.06352.
2. A. Agosti et al., Magma N. Y. N (2021), doi:10.1007/s10334-021-00967-4.
3. C. R. Harris et al., Nature. 585, 357–362 (2020).
4. 4. K. M. Gooding et al., BMC Nephrol. 21, 242 (2020).

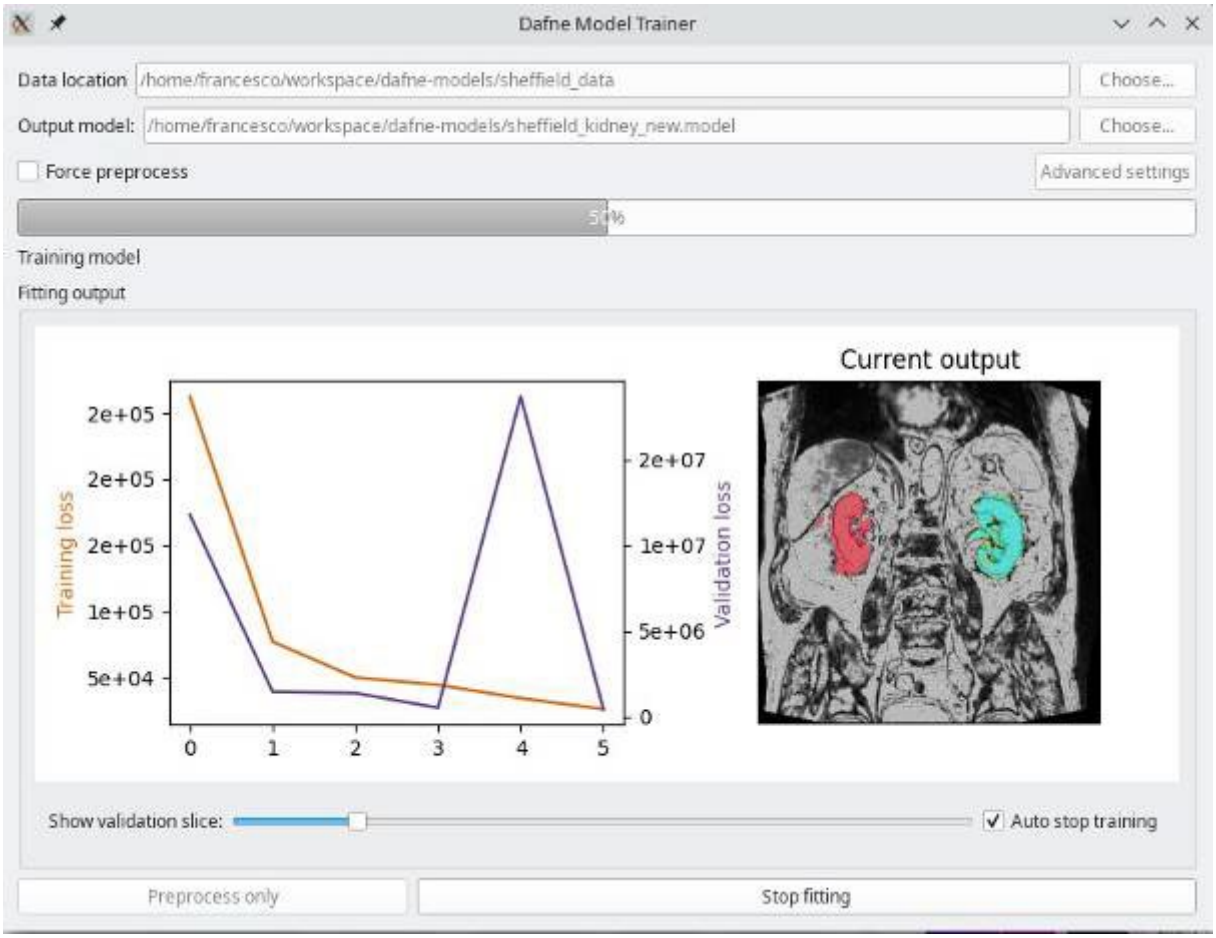

Fig. 1: Model trainer interface during fitting. Both training and validation loss are shown (with different scales), and the segmentation of one slice from the validation set.

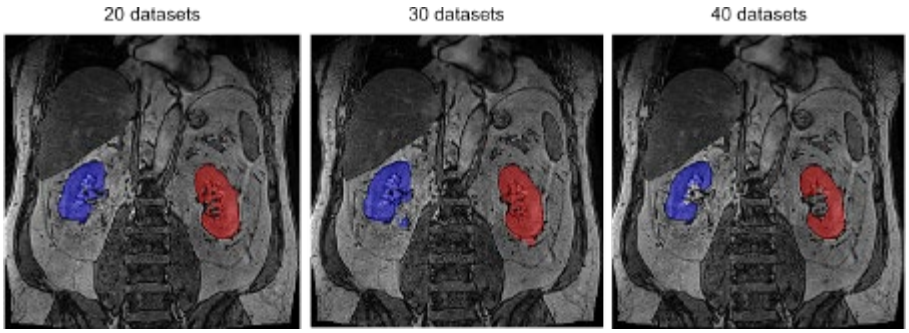

Fig. 2: Performance of the three models, pretrained on 20, 30, and 40 datasets respectively, on a test slice, as shown from within the Dafne segmentation interface.

LB291.

Real-Time MRI Power Tracking for Radiology Departments based on log file information

M. Zaiss[1], Y. Luo[1], S. Weinmüller[1], F. Heye[2]

[1]UK Erlangen, Neuroradiology, Erlangen, Germany
[2]University Hospital Basel, Department of Radiology, Basel, Switzerland

Introduction: Radiology Departments are one of the biggest energy consumers within clinical environments, with MR scanners leading the list of greedy devices. Recent analysis have shown that the energy demand can be reduced massively, when simple measures are taken for optimizing work flow and on/off/idle times [1,2], without affecting the patient car at all. This optimization can be justified, realized and advanced further when an energy consumption analysis would be available, as it was available for the authors of the studies [1,2]. However, the current installed MRI systems lack access to such detailed energy analysis, leaving radiology departments unaware of their energy demand.

Methods: A viable solution lies in utilizing the log files generated during scanning operations as shown in figure 1. These log files serve as a treasure trove of essential information regarding scans, such as on/off/idle times, as well as information about sequences and protocols. Extracting pertinent information from these log files and mapping it to the existing published energy consumption data, provides a coarse, but highly valuable energy consumption estimation and thus unlocks the ability to track the operational states of imaging systems for any Department with arbitrary scanner types as pictured by figure 2.

We used the data of Heye et al. [1] of a 3T Siemens scanner in clinical routine, and first generated LOGEVENT input data with 3 features: (i) the log ID indicating boot, shutdown, start and stop of a sequences, (ii) the sequence type (none if no sequence, but break or scanner off), and (iii) the duration of the event of the current log ID.

Secondly, we created the average measured POWER target data using the high time-resolution measured energy data from the same scanner [1].

The log2power network is then trained as follows: The LOGEVENT input data is mapped to the average POWER data using 4-layer fully connected network with 3-20-20-20-1 neurons and logsig activation and linear output layer. Training was performed on one month of scan data, and test data was used from a second month using the Matlab nntool.

Results´: The network took around 1000 iterations (10 min) to describe 85% of the data with a RMSE of about 9 kW (see Figure 2) before early stopping.

Figure 3 shows a training and test case scenario of the real, the average and the predicted powerby the log2power network, with some over and some undderestimations, but overall good performance to detect scanner off power demand, scanner on-idle power demand and scanner different active power demand of different sequences.

Discussion: Implementing a real-time energy tracking system based on log files offers several benefits and implications. Firstly, radiology departments can actively contribute to energy sustainability by reducing energy demand and lowering CO2 emissions. Secondly, this approach enables departments to make data-driven decisions, optimize energy usage, and achieve cost savings. Additionally, the ability to track energy consumption in real-time allows for proactive maintenance and identification of potential issues, ensuring optimal performance and prolonging the lifespan of scanner systems. We show that this is in principle possible with acceptable accuracy based on limited logfile information.

Conclusion: In summary, by incorporating the energy-saving options after harnessing the utility of scanner log files, an effective system for real-time energy tracking is proposed. By using such tools for reducing energy demand and subsequently lowering CO2 emissions, healthcare institutions actively contribute to the global efforts in combating climate change and promoting a greener future.

References

1. Heye T, Knoerl R, Wehrle T, Mangold D, Cerminara A, Loser M, Plumeyer M, Degen M, Lüthy R, Brodbeck D, Merkle E. The Energy Consumption of Radiology: Energy- and Cost-saving Opportunities for CT and MRI Operation. Radiology. 2020;295(3):593-605. doi:10.1148/radiol.2020192084
2. Heye T, Meyer MT, Merkle EM, Vosshenrich J. Turn It Off! A Simple Method to Save Energy and CO2 Emissions in a Hospital Setting with Focus on Radiology by Monitoring Nonproductive Energy-consuming Devices. Radiology. 2023;307(4):e230162.

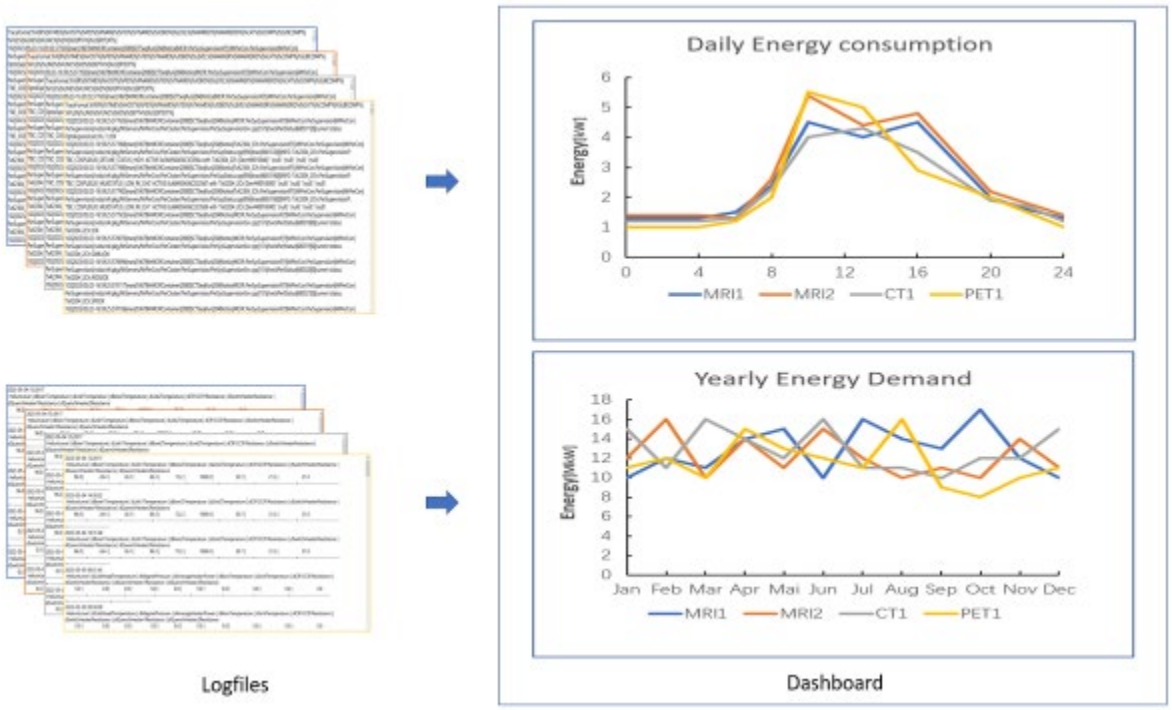

Figure 1: Schematic diagram of the log2power Tracking Dashboard for Radiology Departments.

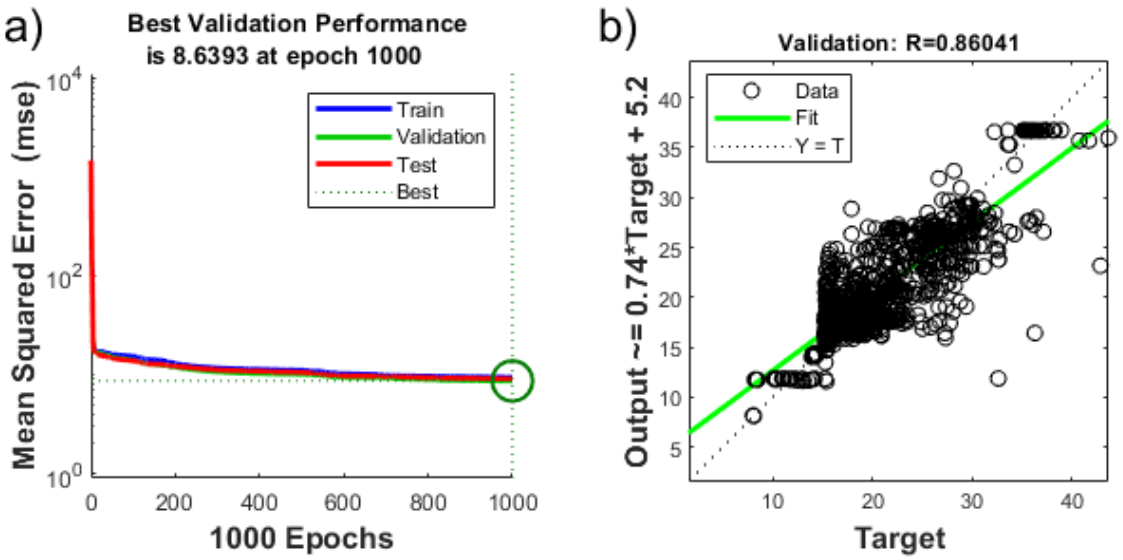

Figure 2: Training curve (a) and regression plot (b) of the log2power network.

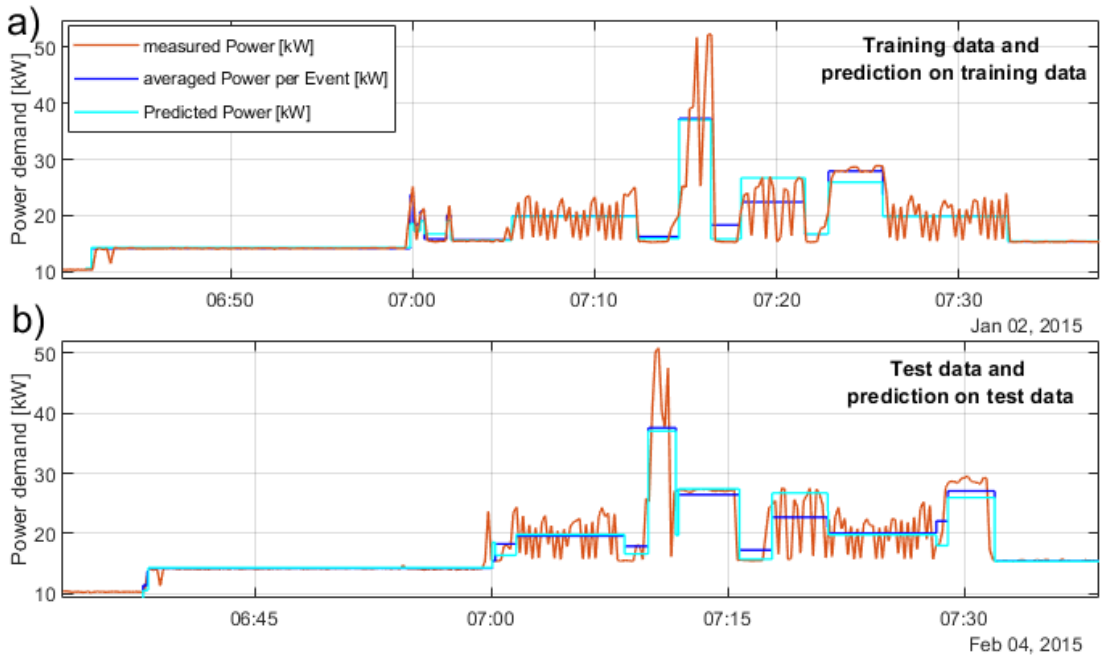

Figure 3: a) High time-resolution measured power demand of the MRI system (red solid line), this data is averaged over the log events (solid blue line), which forms the training data for the log2power network. The prediction of the log2power network is shown here for the training data sample (a, cyan solid line), as well as for an unseen test data sample (b, cyan solid line).

LB292.

Flexible and computationally efficient framework for diffusion MRI simulations in realistic neuron morphologies shows signal signature of soma-dendrite exchange

I. de Riedmatten[1], J. Nguyen-Duc[1], J. R. Patino Lopez[2,3], I. Jelescu[1]

[1]Université de Lausanne, Lausanne, Switzerland
[2]Centre hospitalier universitaire vaudois (CHUV), Lausanne, Switzerland
[3]Ecole Polytechnique Federale de Lausanne (EPFL), Lausanne, Switzerland

Diffusion MRI (dMRI) has potential to shed light onto brain microstructure. Given the limitation of diffusion models to render the complexity of brain tissue, numerical phantom have been used for the flexibility to tune their properties to any level of realism1. Most phantoms mimic white matter2 with triangular meshes. This involves a substantial computational expense for the substrate generation and the simulation of water diffusion using Monte-Carlo simulations (MCS), particularly for gray matter (GM). We propose an in-house software that generates realistic neurons using overlapping spheres at a reduced computational cost, as initially introduced in3. Using MCS, we investigate the impact of two neuron features on the dMRI signal from a conventional acquisition: water exchange between the soma and the dendrites, and dendritic branching. Our results show that, in our substrates, the branching is negligible while the exchange is not.

Neuron substrates were built using in-house software in C++ and MCS performed using a modified MCDC simulator4 to accommodate overlapping spheres. Substrates were leak-proof (data not shown). The convergence of the simulator propagators was benchmarked for different timesteps T and walkers N on an example motor neuron5(Fig. 1). Each (T,N) combination was evaluated over 5 repetitions for a Pulse-Gradient Spin Echo (PGSE) sequence with Δ=50ms, δ=16.5ms, TE=67ms, G=[0, 15, 34, 48, 59, 68, 76, 83, 90, 96, 102, 107]mT/m and 21 directions (Fig. 2). Using the optimal (T,N) combination, we ran the simulation on 5 neurons (Fig. 1) and probed diffusion in four environments: soma only, dendrites only, disconnected soma and dendrites and connected soma and dendrites. We compared the numerical powder-averaged dMRI signal to the analytical solutions for diffusion in a sphere6, in randomly-oriented infinite sticks7, and a linear combination of the two. We also compared the signals from 5 neurons with branched vs straight dendrites.

Convergence was ensured (σ=0.005) for T=5000 (step length= 0.448µm) and N=50000 (Fig. 2). The signals from soma only and dendrites only follow their respective analytical formulas, and the disconnected case follows the analytical weighted average of the two compartments (Fig. 3 a). In the connected case, the signal is dominated by dendrites contribution for $1 \leq b \leq 4$ ms/µm² and converges towards soma & dendrites solution for $b > 4$. However, for connected soma and dendrites, the final molecule density displayed an imbalance with 10% excess molecules in the dendrites vs soma (Fig.3 b). Finally, the difference between branching and non-branching becomes mostly significant for $b \geq 4$ ms/µm² (Fig. 4).

Exchange between soma and dendrites has so far been neglected8, though it was shown to have an effect in straight but not in branching neurons9. Our simulations show that with intermediate b-values (1-4 ms/µm²), the signals between disconnected and connected configurations also diverge in branched neurons. It remains to be established if this behavior is due to the neurons" geometry: we modeled the connected case without any hindrance or morphological "funnel" between the soma and dendrites, which may result in artifactual particle accumulation in the dendrites. A smaller step size may also be preferred. Finally, we show that a standard PGSE diffusion measurement on a clinical MRI system is not sensitive to branching, especially if considering realistic Rician noise, as shown in9. The effect of branching is however expected to be more pronounced as the diffusion length approaches the segment length. Future work will focus on optimizing the intracellular water transfer between soma and dendrites, and on determining the bias of branching on simple analytical model estimates8,10.

Diffusion simulations within neuronal substrates are a promising tool to non-invasively quantify GM microstructure in vivo. We use a flexible and computationally efficient framework to generate realistic neurons, where we show that intracellular water transit without any osmotic gradient between soma and dendrites has a detectable influence on the diffusion signal whereas branching has not. Further developments will consist in packing neurons to yield a realistic extracellular space, considering dendrite tortuosity (facilitated by the sphere building blocks) and membrane permeability10.

1. Jelescu, J Neurosci Meth 2020
2. Fieremans and Lee, NeuroImage 2018
3. Ginsburger, NeuroImage 2019
4. Rafael-Patino, Front Neuroinf 2020
5. Palombo, NeuroImage 2019

6. Murday and Cotts, 1968
7. Callaghan, Biophys J 1979
8. Palombo, NeuroImage 2020
9. Ianus, NeuroImage 2021
10. Jelescu, NeuroImage 2022

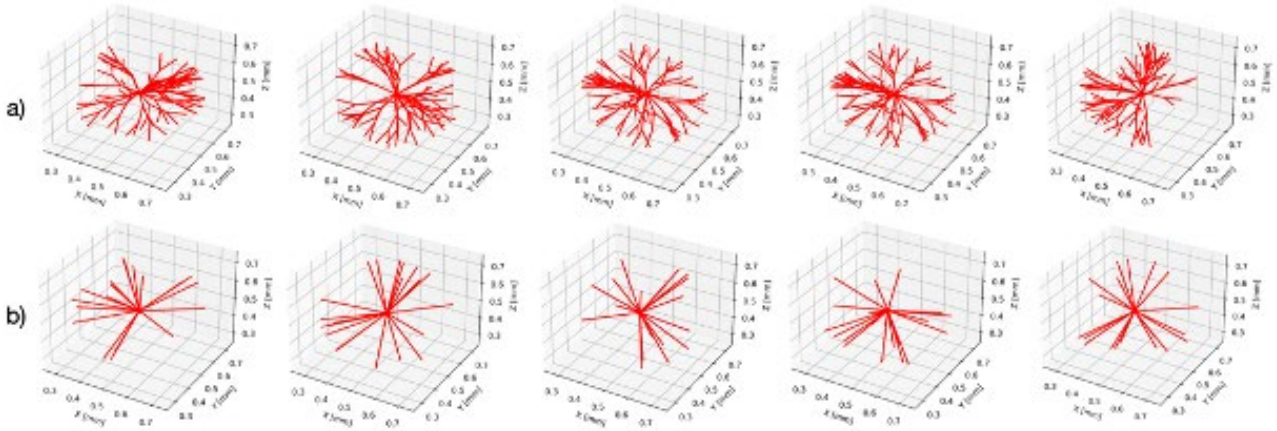

Fig.1 : Neurons with two (a) or no (b) branching. Rsoma=10µm, Rdendrites=0.5µm, 20 dendrites, cell span=~480µm. (a) Each dendrite branches twice, leading to seven 80µm-long segments. Branching angles are sampled from N(π/4,π/16). (b) 240µm-long segments. The soma and dendrite fractions are 32% & 68% (a), and 53% & 47% (b).

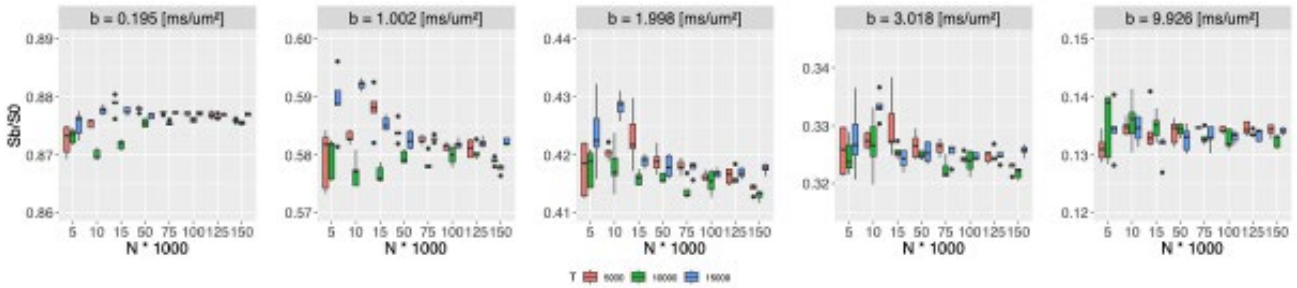

Fig.2 : Benchmark for (T,N) convergence, averaged across 5 repetitions on one neuron.

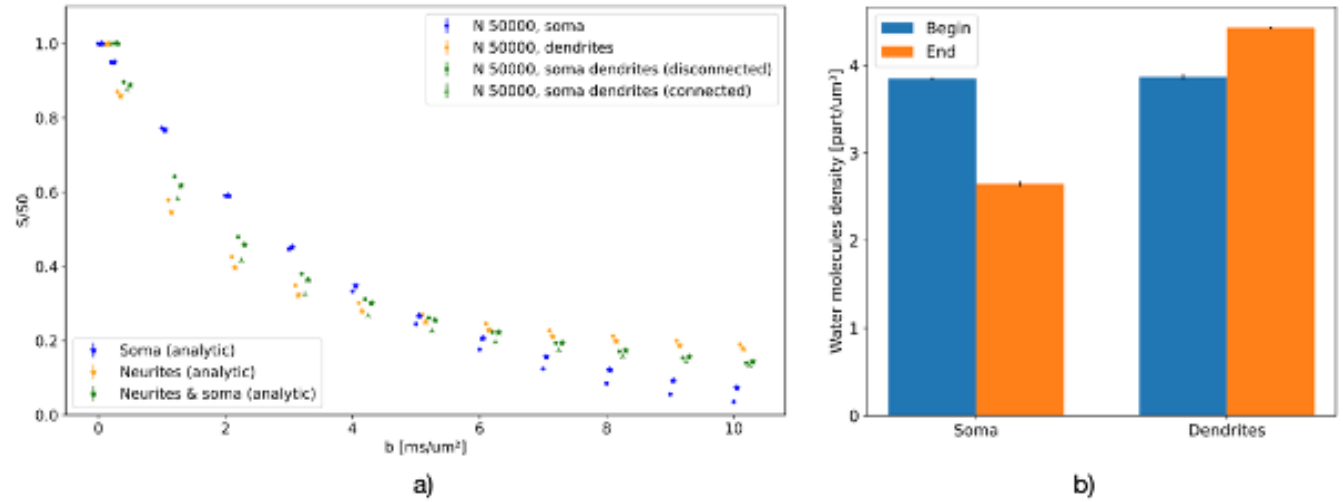

Fig.3 : (a) Numerical dMRI signal in 4 environments: soma, dendrites, disconnected soma and dendrites or connected soma and dendrites. Signals are averaged over 5 neurons, 5 repetitions each. σ<0.0038 across the 5 neurons. Star symbols: analytical solution for diffusion in sphere, randomly-oriented infinite sticks and a linear combination of the two. (b) Density of walkers starting and ending in the soma or dendritic compartment (connected case).

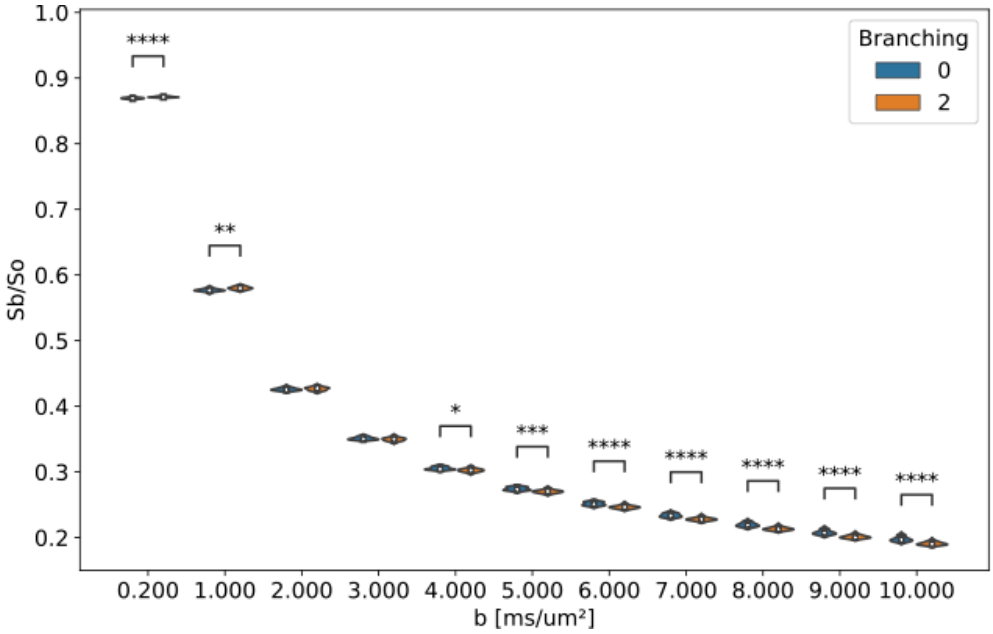

Fig.4 Effect of two branching (2) vs no branching (0) on the diffusion signal. Averaged over 5 neurons, 5 repetitions each. Mann-Whitney-Wilcoxon test two-sided with Bonferroni correction. ** : 1e-3 < p ≤ 1e-2, **** : p ≤ 1e-4

LB293.

Physics-Informed Neural Network for T2 and M0 Map Estimation

Z. Yang[1], L. Branca[2], R. Moreno[1]

[1]KTH royal institute of technology, Stockholm, Sweden
[2]Scuola Normale Superiore, Pisa, Italy

Introduction: Magnetic resonance imaging (MRI) is a widely used technique for disease diagnosis. One issue with many MRI sequences is that they are not quantitative. Instead, quantitative MRI (qMRI) sequences aim to provide objective measurements that can be used for a better characterization of diseases.

Generally, tissue parameters such as T1, T2 and can be extracted by fitting a set of images acquired with relaxation equations. The accuracy of the estimations increases with the number of images at the cost of longer acquisitions.

Physics-informed neural networks (PINNs) is a relatively new method that uses both physics knowledge and machine learning for performing estimations. In this paper, we explore the use of PINNs for T2 and M_0 using a reduced number of acquisitions. To the best of our knowledge, this is the first attempt to use PINNs in this application.

Methods: The Bloch equations can be used to estimate the nuclear magnetization. In particular, **Eq. 1 (In Fig. 4)** describes the relaxation process in the x direction, where M_x is the transverse magnetization in x, and the T_2 represents the transverse relaxation rate, respectively. **Eq. 2 (In Fig. 4)** can be solved as shown, where M_0 is the initial magnetization value. The T_2 and M_0 parameters are commonly estimated by least squares. Our goal is to estimate T_2 and M_0 with PINNs.

Fig. 1 is our proposed PINN. We designed a three-layered, fully connected neural network. The loss function comprises a physics loss L_{phys} and observation measurement L_{meas} loss.

Experimental Results: To validate the proposed method, simulated and real datasets are used to compare the results. The simulated data is generated by Eq. 2 with different percentages of added noise. The vivo dataset is taken from [1]. This dataset comprises images acquired by 3T Bruker BioSpec system using rapid acquisition with refocused echoes (RARE) variable TR (TR = 0.1 seconds, 0.3 seconds, 0.5 seconds, 0.8 seconds, 1.1 seconds, 1.6 seconds, 2.4 seconds, 3.0 seconds, and 4.0 seconds) and a multislice multi-echo sequence with TE varied from 12 ms to 360 ms (30 echoes in total). The estimations were performed slice by slice.

The deepXDE library[2] develops the PINN model with 3 multi-layer perceptron. Adam and L-BFGS are used to optimize the neural network model with 30000 iterations and an initial learning rate of 0.001.

Simulation Experiment: To compare the robustness of PINNs, the simulated data were compared with the least square method (LSM). We added 10% Gaussian noise to the simulated data and compared the mean and variance of the estimated parameters. We selected several typical T_2 and M_0 values to make the comparison more representative. We set TR=1s, TE=111-999ms, with nine uniformly sampled echoes. Table 1 ((Attachment 4)) shows that LSM and PINNs yield similar estimation results, with the PINNs having a lower standard deviation.

In vivo Experiment: We use the T2 weighted mouse brain data to compare the results. To demonstrate the accuracy of PINN, we compared the estimation accuracy between PINNs and LSM fitted map with 15 sampled T_2 weighted images. Fig. 2 illustrates the reconstructed T_2 mouse brain and error maps. Fig. 3 illustrates the reconstructed mouse brain map M_0 and error map. The error map is computed as the absolute error between the fully sampled fitted map (30 echoes) and the undersampled fitted map (15 echoes). From the error map, we can see a significant difference between LSM and PINNs. It demonstrates that the PINN-based method is more accurate compared with LSM at the same level of sampled data.

Discussion and Conclusions: We proposed a physics-informed neural network for T_2 and M_0 estimation. To the best of our knowledge, this is the first work to use PINNs to estimate these quantitative parameters. Compared with LSM, our proposed method is more robust to noise and more accurate with the same level of undersampled data. Compared to other deep learning-based methods, PINN has more interpretability since the solution must be close to the governing equations in the physics loss and require less data to train the network.

This work was supported by grants from Marie Skłodowska-Curie Doctoral Networks Actions (HORIZON-MSCA-2021-DN-01-01) with a grant number of 101073222 and Cancerfonden (Grants 22-2389 Pj)

1. Huang, Jianpan, et al. "Relayed nuclear Overhauser enhancement imaging with magnetization transfer contrast suppression at 3 T." Magnetic resonance in medicine 85.1 (2021): 254-267.
2. Lu, Lu, et al. "DeepXDE: A deep learning library for solving differential equations." SIAM review 63.1 (2021): 208-228.

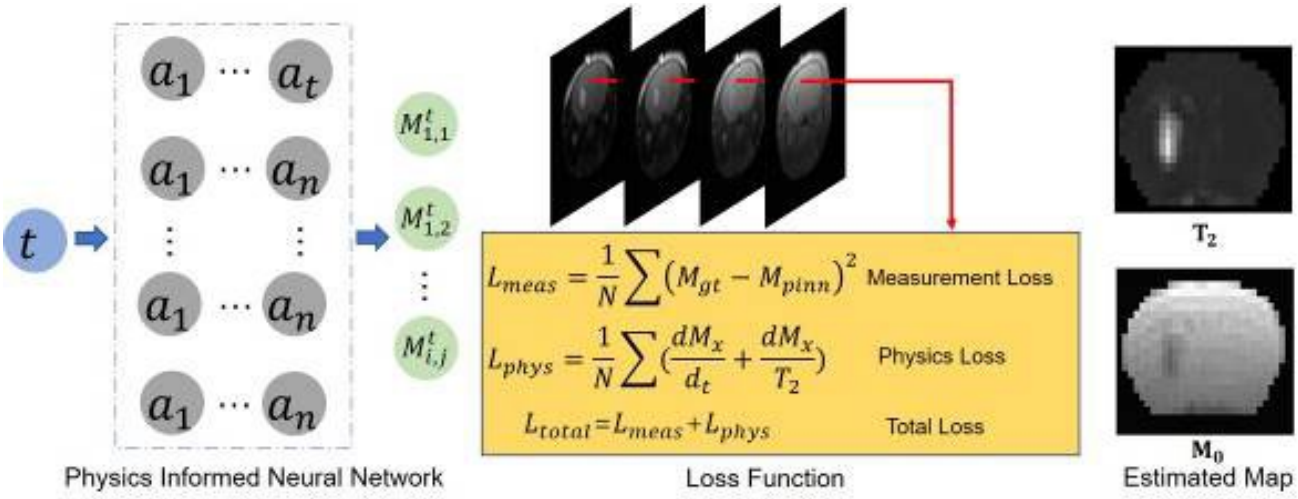

Figure 1. Overview of the proposed PINN for T_2 and M_0 estimation. The model input is the sampled time t, and the output is the transverse magnetization in x M_{ij}^t, with the subscript i,j being the location of the 2D image in pixels. The whole network structure comprises three fully connected layers, each with 50 neurons. The loss function L_{total} comprises a measurement loss and a physics constraint loss. T_2 is a parameter of the PINN that is updated during training to minimize the physics loss. M_0 is estimated by taking the output when PINN at t=0. The right part illustrates the estimated T_2 and M_0 map after training the network.

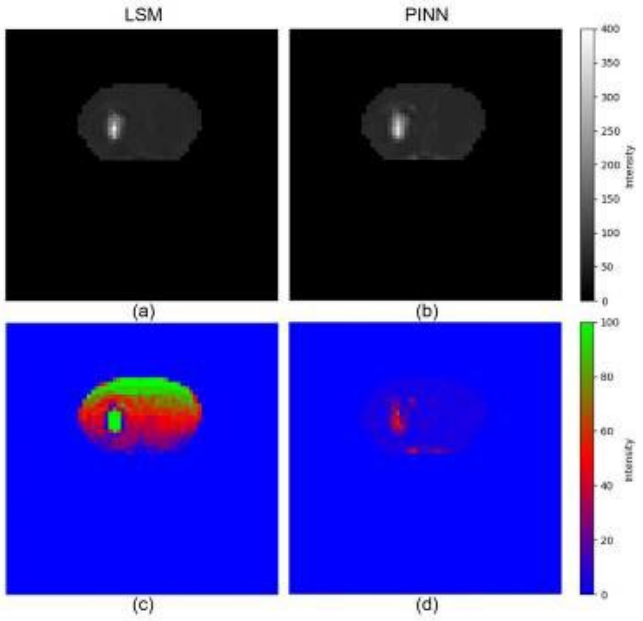

Figure 2. Comparison between LSM and PINN estimated T2 map.
Figures (a) and (b) are estimated maps. Figures (c) and (d) are error maps.

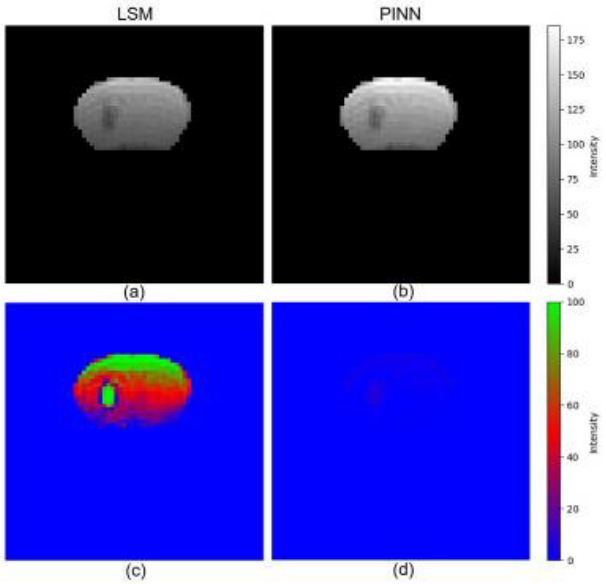

Figure 3. Comparison between LSM and PINN M_0 estimation.
Figures (a) and (b) are estimated maps. Figures (c) and (d) are error maps.

$$\frac{dM_x}{dt} = -\frac{M_x}{T_2} \quad (1)$$

$$M_x = M_0 e^{-\frac{t}{T_2}} \quad (2)$$

Table 1: Performance of the methods on simulated data

Methods	T2	M_0	T2	M_0
Simulated Param	75	100	75	80
PINN	75.05±0.07	100.02±0.02	75.02±0.06	80.02±0.01
LSM	74.99±0.16	100.00±0.01	75.00±0.21	79.99±0.01

Figure 4 is magnetization equation and simulation comparison.

LB294.

Main Category - Where?: Abdomen and Pelvis

A shortened MOLLI for renal T1 mapping: comparison of signal models

J. Periquito[1], K. Sharma[1], K. K. Soe[1], B. Alhummiany[2], J. Fulford[3], D. Shelley[2], K. M. Gooding[3], A. Shore[3], M. Mansfield[4], S. Sourbron[1]

[1]University of Sheffield, Sheffield, United Kingdom
[2]University of Leeds, Leeds, United Kingdom
[3]University of Exeter Medical School, Exeter, United Kingdom
[4]Leeds Teaching Hospitals NHS Trust, Leeds, United Kingdom

Introduction: Several studies have shown that T_1 mapping can be a useful tool to diagnose kidney disease [2, 3]. A recent consensus [3] recommends a MOLLI based pulse sequence [4] for T_1-mapping in the kidney, but MOLLI-sequences are slow due to the need of full relaxation between the 180° inversions. Acceleration can be easily achieved by repeating preparation pulses before complete relaxation, but this requires accurate signal modelling to account for incomplete recovery of the magnetization. The well-known "ShMOLLI" [5] approach for cardiac T_1-mapping uses conditional data analysis, but this may be difficult to generalise to other applications. Bloch modelling can correctly account for incomplete recovery in the propagation of magnetization through the pulses. The aim of this study is to compare the Bloch modelling approach against the recommended mono-exponential approach using numerical simulations, phantom data and a cohort of 50 patients with diabetic kidney disease (DKD).

Methods: T_1 mapping (MOLLI based sequence): three sets of TI [16,8,4] ranging from [100:7700]ms were immediately followed by a 2D-*FLASH* readout (TE=2.36ms, TR=2.6ms, Grappa=2, Partial Fourier acceleration=5/8) [6] without complete recovery. Using Python, a Bloch simulation-based model was created.

Numerical simulations: simulations with a T_1=1340ms were performed to compare the relative error (RE) of the Bloch and mono exponential in data with complete and incomplete recovery at different SNR. RE was calculated and displayed in a boxplot for the different SNR, the bias (median RE) and random error (interquartile range) were assessed.

Phantom experiments: NIST/ISMRM phantom [7] was scanned using a MAGNETOM Prisma 3.0T MRI (Siemens Healthcare GmbH, Erlangen, Germany). T_1 mapping data was acquired with the described MOLLI sequence. Three T_1 reference spheres: T2-5: (T_1=1340ms, T_2=134ms), T2-6: (T_1=1017ms, T_2=94ms,) and T2-7: (T_1=782ms, T_2=62ms,) were fitted using a standard mono exponential and the Bloch model.

Patient experiments: to test the systematic error in real world, 50 patients with a diagnosis of type 2 diabetes and eGFR greater or equal to 30 mL/min/1.73m^2, aged between 18 and 80 years were recruited [6]. The described MOLLI was used (with breath hold), using a coronal-oblique orientation and a 400x400mm FOV. T_1 from cortex and medulla were obtained.

Results

Numerical simulations: **Figure 1** shows the Bloch model produces the same results as the mono-exponential model when the pulse sequence allows a complete recovery. Bias for both models go towards 0% as SNR increases. The mono-exponential model produces large systematic errors in case of incomplete recovery (-19.7% at SNR 20) while the Bloch model has -1.5% bias and a random error of 7.3%.

Phantom data: **Figure 2** shows mono exponential fit fails to accurately quantify the T_1 showing a bias of -17.0%, -11.4%, -6.7% in the spheres T2-5, T2-6, T2-7. The Bloch model showed a higher accuracy by reducing these biases to 5.7%, -0.5% and -1.5% respectively.

Patient data: **Figure 3** shows the median calculated T_1 values using the Bloch model are in the range reported in the literature [4, 5] while T_1 values calculated from mono exponential fit are below the reference range. **Figure 4** shows two examples of the T_1 maps generated by the scanner ("Standard") and by the Bloch model ("Corrected").

Discussion: This work shows that the consensus [1] recommended T_1 mapping MOLLI [4] sequence can be shortened and still provide accurately T_1 values when coupled with Bloch-simulation signal modelling. Numerical simulations (T_1 = 1340ms) show the error of using mono-exponential with incomplete recovery can be as high as -18.9%. A similar error was found in the NIST phantom for the sphere with the same T_1 -17.0%. While the use of Bloch model showed errors in the order of 1.5% in the numerical simulations and less than 6% for phantom experiments.

Renal T_1 values from 50 DKD patients the showed a good agreement with the literature. The data show that accurate signal modelling is critical. Standard signal modelling as recommended in the current consensus would produce a T_1 underestimation, which would lead to an inaccurate classification of pathological kidneys.

Conclusion: The proposed shortened MOLLI sequence with signal analysis based on Bloch simulations produces accurate and consistent measurements of renal T_1. Standard mono-exponential models are very sensitive to incomplete recovery and should be used only when a sufficient waiting time between pulses is foreseen.

References

[1] - Dekkers, IA et al. Magma 33,1 (2020)
[2] - Cox EF, et al Front Physiol 2017; 8: 696
[3] - Gillis KA, et al. Nephron 2016; 133: 183–192
[4] - Messroghli, D R et al. MRM vol. 52,1 (2004): 141-6
[5] - Stefan K, P., et al. (2010). JCMR, 12, 69.
[6] - Gooding, K M et al. BMC nephrology vol. 21,1 242. 29 Jun. 2020
[7] - Russek, S. E., et al. Proceedings of the 2020 ISMRM, Melbourne, Australia. 2012.

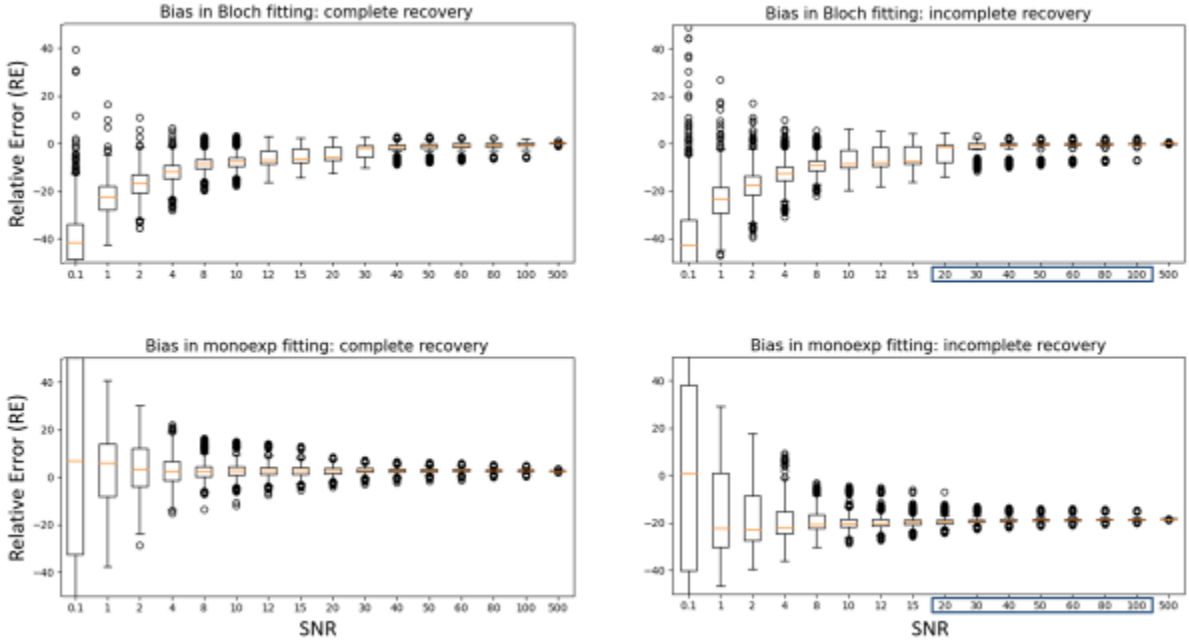

Figure 1: Box plot of the numerical simulations. The box plots compare the relative error (RE) between the standard model: mono-exponential (top row) and the Bloch model (bottom row) for a pulse sequence that allows a complete T_1 recovery (left column) and for a pulse sequence that does not allow complete recovery (right column). The highlighted SNR values [20 100] correspond to the SNR of our patient dataset.

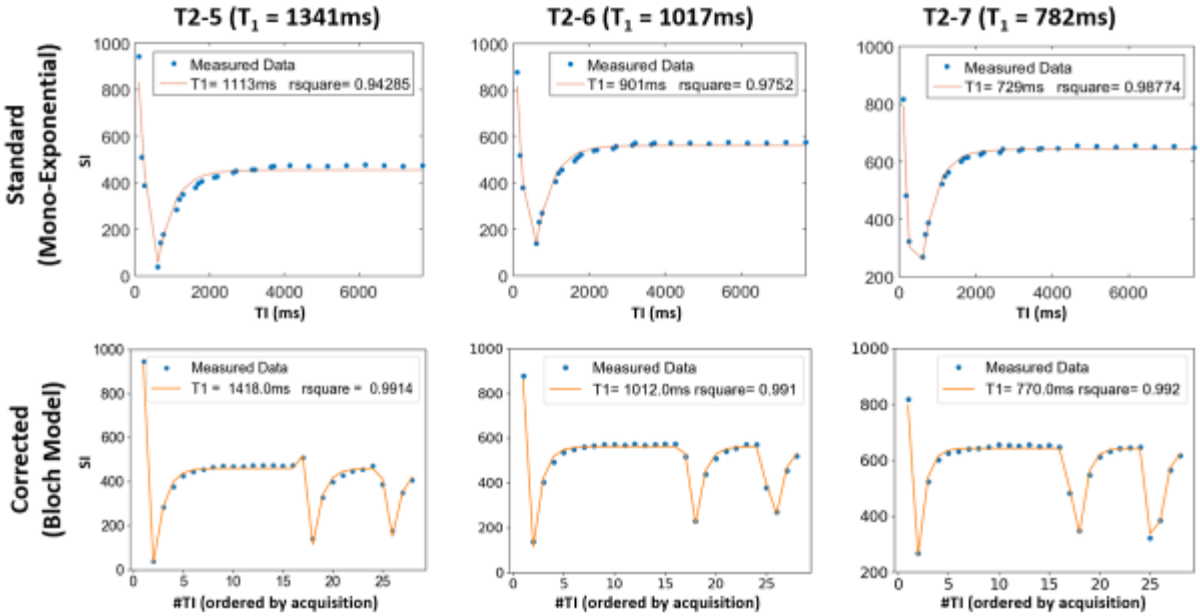

Figure 2: T_1 curve fits of the NIST/ISMRM phantom MR experiments. T_1 fits are displayed for each NIST/ISMRM T_1 reference spheres: T2-5 (left column), T2-6 (middle column), T2-7 (right column) using mono-exponential fit (top row), Bloch model (bottom row).

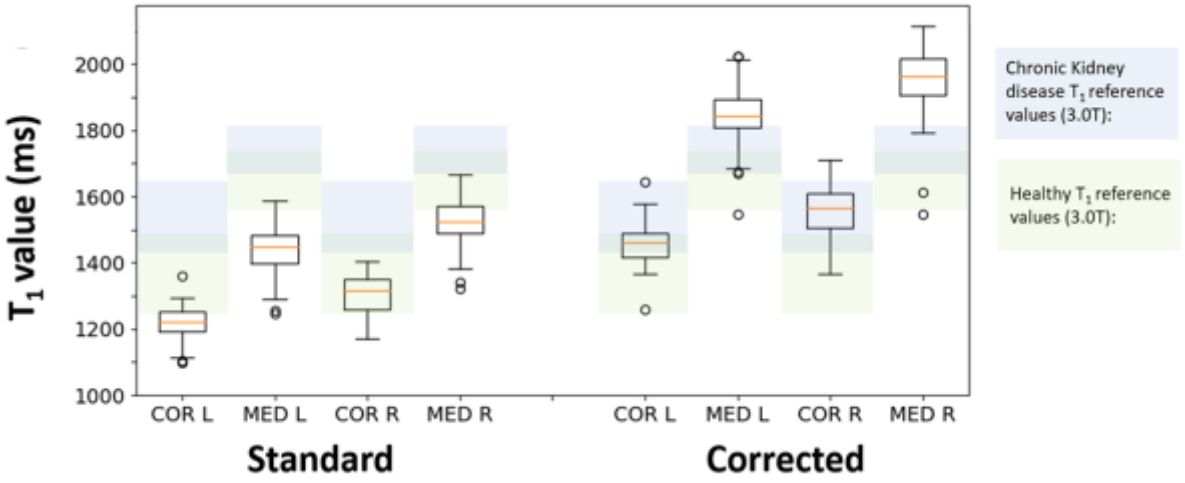

Figure 3: Summary of patient data. On the left, the plot shows the boxplot of the calculated T_1 values using the mono-exponential maps generated by the scanner software, and on the right the T_1 values calculated using the Bloch model fit for all the patients (N=50).

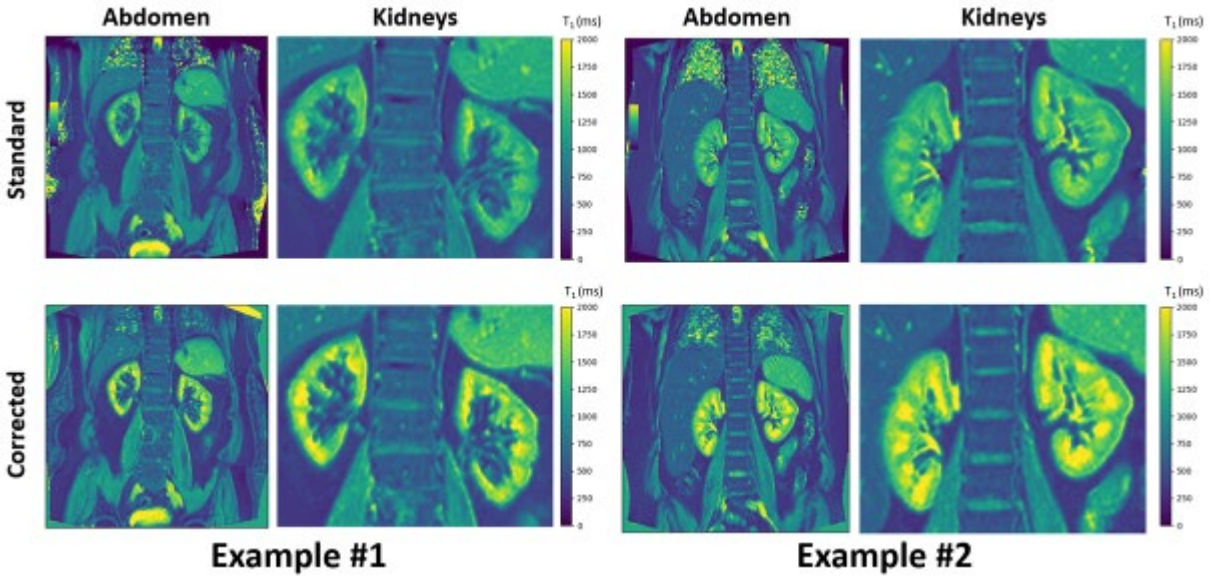

Figure 4: Two examples of patients T_1 maps.

LB295.

Magnetization-transfer residuals in T1 mapping in the human brain

N. Priovoulos[1,2], M. Caan[2], W. van der Zwaag[1]

[1]Amsterdam UMC, Spinoza Center for Neuroimaging, Amsterdam, Netherlands
[2]Amsterdam UMC, Department of Biomedical Engineering and Physics, Amsterdam, Netherlands

Introduction: The inversion recovery (IR) rate is sensitive to the brain's myelin content [1] and therefore is commonly used for brain imaging and quantification (T1 mapping), with extensive neuroscientific and clinical applications. T1 mapping has been shown, however, to have sizable scanner-to-scanner variability [2]. IR is typically modeled as a single exponential to simplify the fit, but it has been shown to have a subtly biexponential behavior [3] due to magnetization transfer (MT) between free-water and lipid signal pools [3,4]. This discrepancy may assign unmodeled signal to residuals and increase T1 mapping variability. Here, we examine the effect of lipid pool fraction, imperfect lipid-pool inversion, field strength and their interaction to the residuals of T1 mapping when this is assumed to be a single exponential.

Methods: Coupled-compartment IR simulations [3] were performed for 3T and 7T field strengths and different lipid-pool sizes and inversion efficiencies (Fig.1). Additionally, the IR was densely sampled in 4 participants (1 female) in a 7T Philips Achieva with a 2Tx/32Rx whole-head coil, using an adiabatic inversion pulse followed by 15 3D-EPI readouts (FOV = 140 x 141 x 20 mm^3, voxel-size = 1.5 x 1.5 x 2 mm^3, TE/ TRvolume/ TImin/ TImax/ TAtotal = 9/290/27/4120/5000 ms, flip angle=11^o, SENSEy/z=2.7/1, 10 repetitions). In the brain data, white-matter areas of interest were drawn at TI=1200ms and the signal polarity recovered using the phase difference with a reference image. For both simulations and data, the IR was log-transformed, linearly fitted towards T1 and the residuals extracted using R4.3.0.

Results: The simulations captured the expected behavior, such as faster IR with higher lipid-pool fraction and lower field strength. Importantly, our simulations showed that the lipid-pool inversion efficiency can induce variability in IR through MT, with lower lipid-pool inversion efficiency quickening IR and scaling with lipid-pool size and field strength (Fig.2A,C). These increased MT effects result in a systematic intensity difference in residuals along the IR curve (Fig.2A,Cbottom), reflecting the cross-relaxation between pools. Subsequently, the residuals scale with lipid-pool fraction, while an inefficient lipid-pool inversion much reduces lipid-pool fraction IR contrast (e.g. contrast between WM/GM) and shows more pronounced residuals, particularly at 7T due to the slower lipid-pool recovery (Fig2.B right).

The data across participants confirmed a systematic intensity variation in the linear residuals along TIs (Fig.3). The residuals showed anatomical contrast, suggesting sensitivity to the lipid-pool fraction and confirming that the typical linear T1 fit does not capture the whole of the anatomical variation. Importantly, anatomical information in the residuals was particularly pronounced in TIs=[600-1200]ms but not in later TIs (Fig.4B), in line with our simulations that predicted higher lipid-pool fraction sensitivity in the residuals of these TIs (Fig.2B). The residuals in white matter closely align with the simulations, assuming the expected lipid-pool fraction f=0.3 (Fig.4C), showing good agreement between simulations and MRI acquisitions.

Discussion: Anatomical variability in IR rate produces a fundamental brain MRI contrast. Here, we suggest that the biexponentional IR behavior due to MT can induce systematic residuals when the IR is assumed to be a single-exponential process. These residuals can occur through both anatomical differences (i.e. myelin content differences as captured by lipid-pool fraction), system variations (e.g. inefficient lipid-pool inversions), field strength and their interaction. Note that these residuals propagate to TIs typically used in brain imaging (e.g. [1000-5000] in 7T MP2RAGE). These results suggest that MT effects, such as interactions between lipid-pool fraction and incomplete lipid-pool inversion, are possible mechanisms of scanner-to-scanner variability in T1 mapping. Importantly, our methodology suggests a way this variability can be modelled and attenuated across systems through concurrent MT and T1 mapping.

Conclusion: We show the presence of systematic residuals in brain IR that likely relate to MT effects due to anatomical differences and potential system imperfections.

1: Stuber, 2014
2: Stikov, 2014
3: van Gelderen, 2016
4: Teixeira, 2020

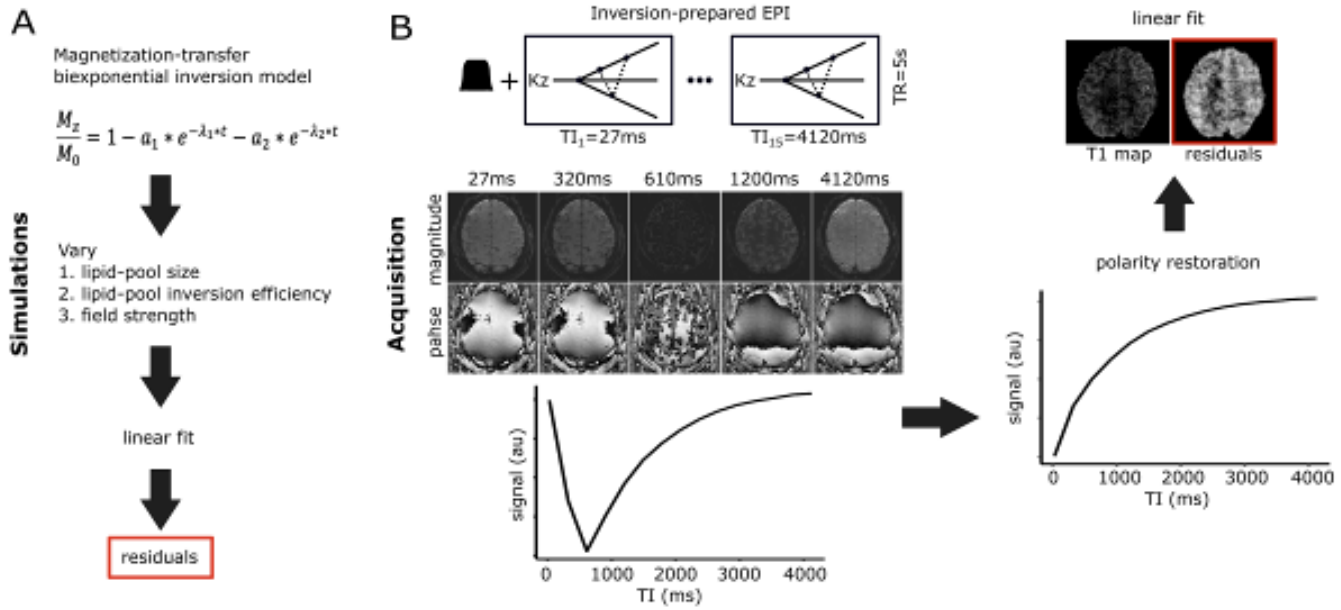

Fig.1: A, A magnetization-transfer bi-exponential model was used to simulate an inversion-recovery experiment while varying the lipid-pool size, the lipid-pool inversion efficiency and field strength. A linear fit towards the T1 was applied and the residuals examined. B, An EPI was used to densely sample the inversion recovery. Following polarity correction, a linear fit was applied and the residuals examined.

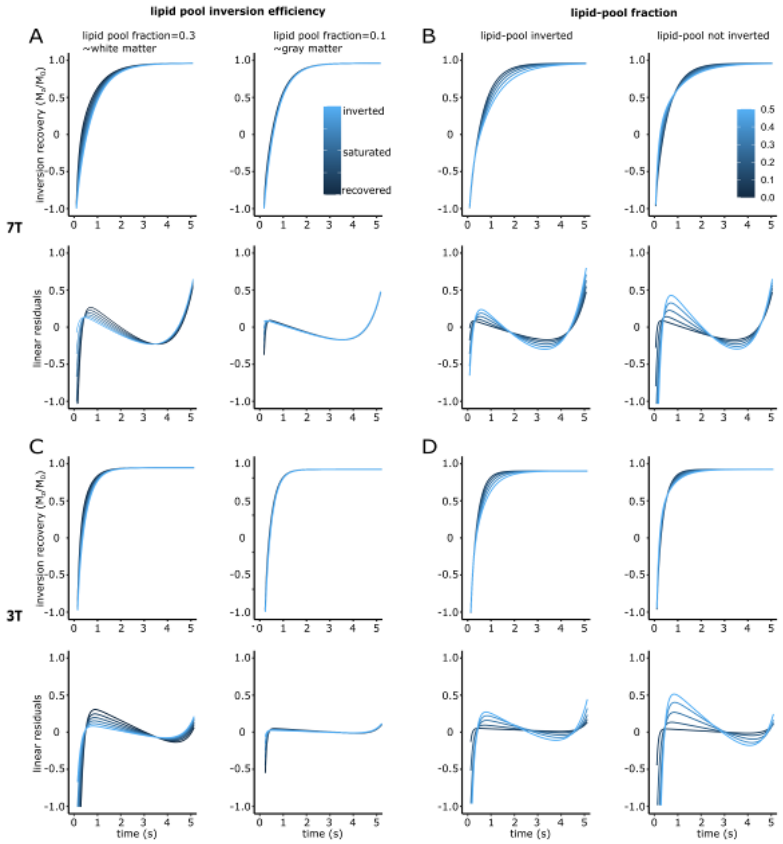

Fig.2: Coupled-compartment inversion recovery simulations and residuals of linear fit for 7T (A, B) and 3T (C, D), while varying the lipid-pool inversion efficiency (A, C) or the lipid-pool fraction (B, D).

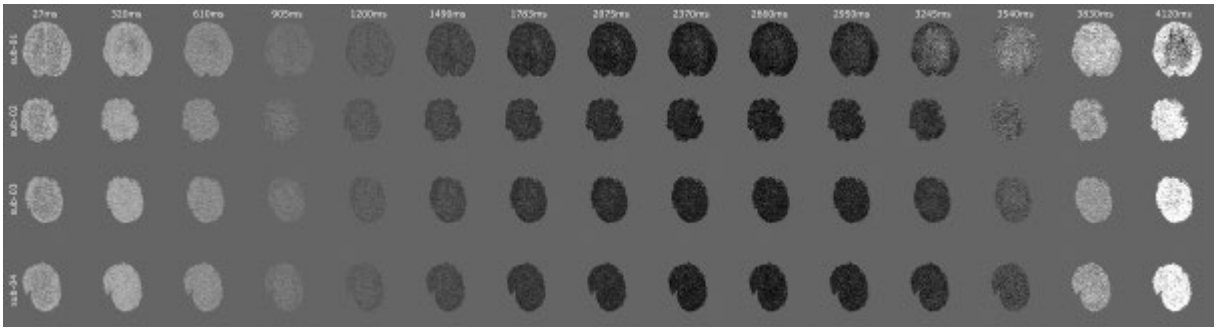

Fig.3: Linear-fit residuals for each participant (row) and TI (column) at the same dynamic range.

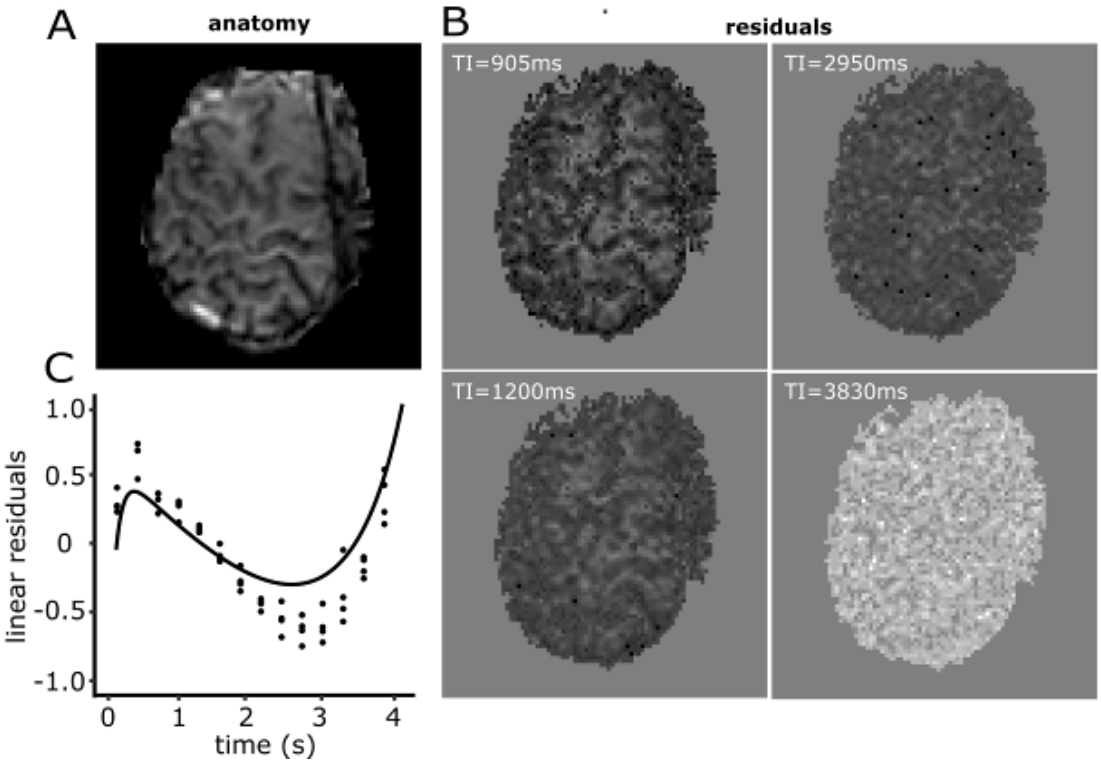

Fig.4: A, EPI magnitude at TI=1200ms. B, Linear-fit residuals at different TIs approximately adjusted for intensity. C, White-matter residuals for each participant (dots) and simulation for similar lipid-pool fraction (f=0.3) for comparison (line).

LB296.

Attention models for incorporating spatial information in deep learning parameter estimation applied to intravoxel incoherent motion

M. Kaandorp[1,2,3], F. Zijlstra[1,2], D. Karimi[3], A. Gholipour[3], P. While[1,2]

[1]St. Olav's University Hospital, Department of Radiology and Nuclear Medicine, Trondheim, Norway
[2]NTNU – Norwegian University of Science and Technology, Department of Circulation and Medical Imaging, Trondheim, Norway
[3]Boston Children's Hospital, Harvard Medical School, Department of Radiology, Boston, MA, United States

Introduction: Deep neural networks (DNNs) present a promising alternative to conventional least squares (LSQ) for model fitting in quantitative MRI. However, these DNNs are often trained voxelwise and do not incorporate spatial information[1]. In contrast, the tissue microenvironment is typically locally homogeneous, where neighboring voxels may contain similar information. Therefore, by exploiting possible correlations between the signals in neighboring voxels, one could expect improved model fitting. Our recent work considered convolution DNNs (CNNs)[2] for incorporating spatial information by training on synthetic data encompassing all plausible combinations of direct correlations in a 3x3 neighborhood. This approach was applied to the intravoxel incoherent motion (IVIM)[3] model for diffusion-weighted imaging (DWI) and yielded promising results, but the convergence rate was suboptimal. Here we extend this approach by using attention models (transformers)[4], which have been shown to outperform CNNs in capturing spatial correlations when applied to diffusion tensor imaging[5]. Furthermore, we investigate whether training on larger neighborhoods can further improve performance.

Methods: We introduce a transformer network[4] utilizing self-attention (3 blocks, 128 units) for IVIM model fitting, and we compare it against a CNN and voxelwise network. Both the CNN and voxelwise networks used in this work were multi-layer perceptrons, where the CNN had a 2D-convolution in its first layer with kernel size 3. The network inputs were patches of DWI signals, and the outputs were the IVIM parameters (D: diffusion, D*: pseudo-diffusion, f: perfusion fraction) and S_0.

The three networks were trained supervised on DWI signals that were simulated by uniformly sampling 3x3 patches of IVIM parameters: $0 \leq S_0 \leq 1$, $0 \times 10^{-3} \leq D \leq 3 \times 10^{-3}$ mm^2/s, $0 \leq f \leq 50\%$, and $3 \times 10^{-3} \leq D^* \leq 100 \times 10^{-3}$ mm^2/s, considering 16 *b* values. Each patch consisted of a random number of neighbors correlated to its center (neighbors-random, Fig. 1A). Rician noise was added to the signals such that when $S_0=1$ the SNR was 200. We evaluated the convergence rate and the final loss on the test set consisting of 100,000 patch-wise sets of IVIM signals. As a baseline to ascertain the optimal achievable performance for a CNN when spatial information is included, an additional set of CNNs was trained specifically for each number of correlated neighbors (neighbors-X, Fig. 1C). We also extended our approach further by training transformer networks on larger patch sizes: 1x1, 3x3, 5x5, 7x7.

Quantitative assessment was performed using 40 novel fractal-noise[6] parameter maps (Fig. 2), which provided ground truths possessing spatial correlations, considering IVIM parameter ranges relevant to the brain. Assessment encompassed comparing parameter maps, median absolute percentage error (MDAPE), and median percentage bias (MDPE). Qualitative assessment was performed on a single IVIM scan from a volunteer. Comparisons were also made to LSQ.

Results: Transformer networks demonstrated superior performance over CNNs for incorporating spatial information. They achieved both improved convergence speed and lower loss (Fig. 1B), matching or surpassing the CNN optima for each specific number of correlated neighbors (Fig. 1C). Fig. 3 further shows that training on larger patch size yielded improved accuracy and decreased bias in regions with low SNR, while retaining edge-like structures, particularly for D*. Fig. 4 qualitatively shows similar findings in an in vivo scan.

Discussion and conclusion: In this work, we showed that attention models outperform CNNs for incorporating spatial information in IVIM model fitting, in terms of convergence speed and accuracy, when trained supervised on synthetic data with spatial correlations. The quantitative evaluation on novel fractal-noise parameter maps indicated improved performance for expanded patch size, while preserving edge-like structures. To conclude, attention models combined with synthetic training data can effectively incorporate spatial information within supervised deep learning. However, future research should further explore how these findings may translate in vivo, as well as possible limitations for even larger patch sizes.

References

1. Kaandorp, Zijlstra, Federau, While. Deep learning IVIM modeling: Exploring the impact of training features and learning strategies. 2023 *MRM*.

2. Kaandorp, Zijlstra, While. Synthetic data shows the potential of unsupervised and supervised learning for incorporating spatial information in IVIM fitting. 2023 *Proc. ISMRM*.
3. Le Bihan, Breton, Lallemand, et al. Separation of diffusion and perfusion in IVIM MR imaging. 1988 *Radiology*.
4. Vaswani, Shazeer, Parmar, et al. Attention is all you need. 2017 *Adv Neural Inf Process Syst*.
5. Karimi, Gholipour. Diffusion tensor estimation with transformer neural networks. 2022 *Artif Intell Med.*
6. Perlin. Image Synthesizer. 1985 *Comput Graph*.

Acknowledgments: FRIPRO Researcher Project 302624.

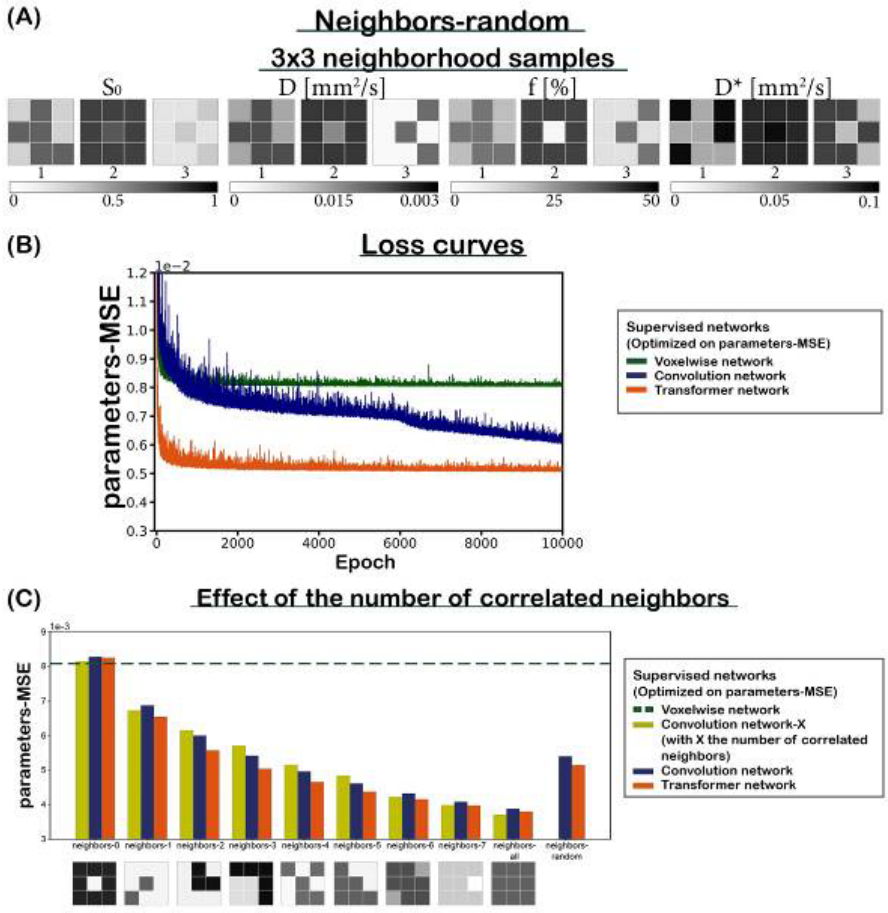

Fig. 1. (A) Example neighbors-random patches. (B) Test curves for networks trained on neighbors-random. (C) Performance of the networks trained on neighbors-random evaluated on neighbors-X with baselines.

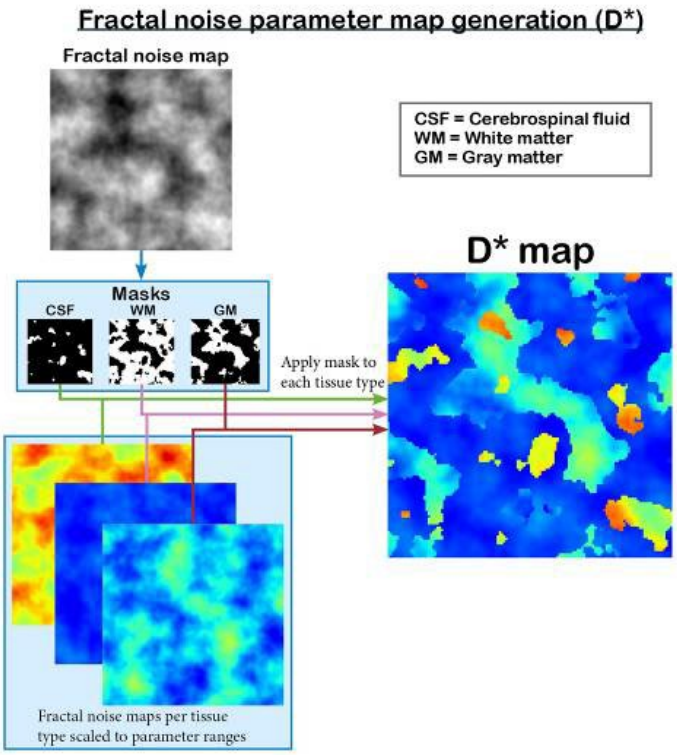

Fig. 2. Example of how a fractal-noise D* map was generated. One fractal-noise map provides masks representing the tissue types. Other fractal-noise maps are scaled to appropriate values of each tissue type. The masks are applied to the corresponding scaled fractal-noise map wherefrom the D* map is generated.

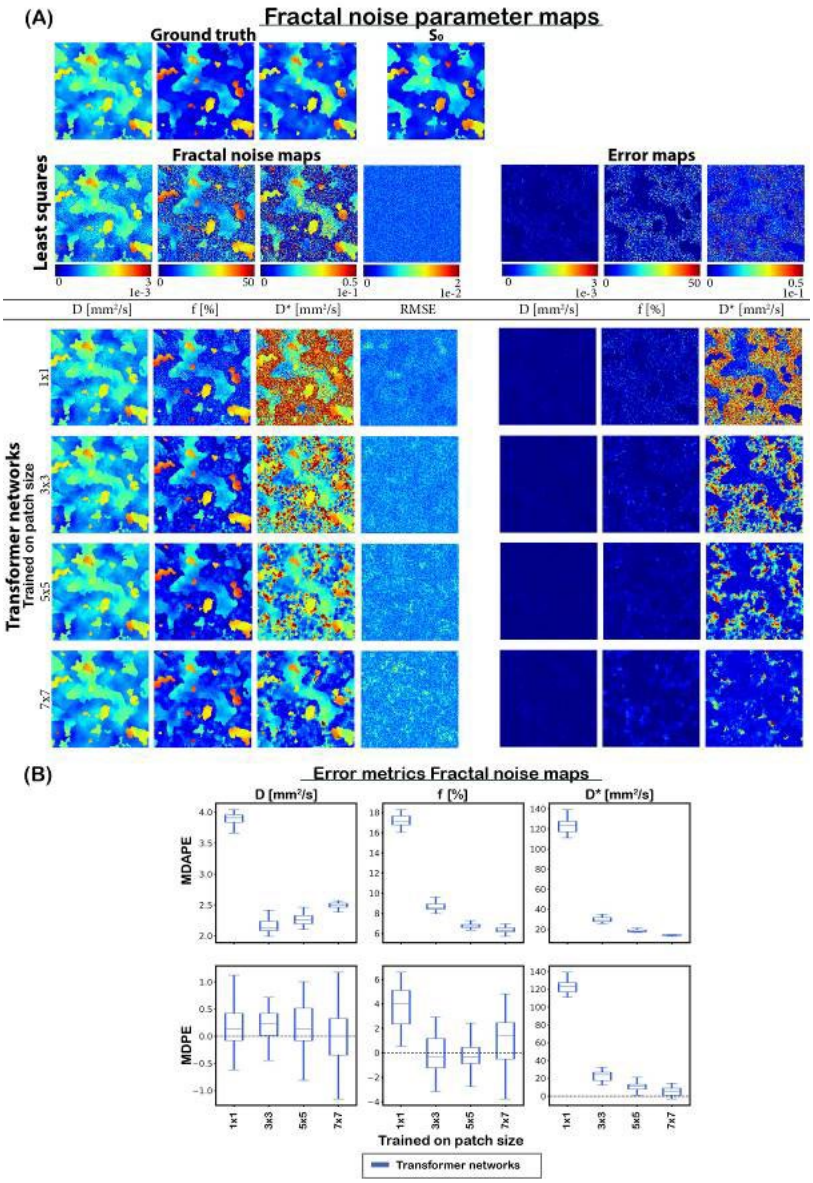

Fig. 3. (A) Example IVIM fractal-noise parameter maps, RMSE maps, and error maps estimated for the transformer networks trained on different patch sizes. (B) Boxplots of MDAPE and MDPE calculated on the fractal-noise test set, evaluated over the last 20 epochs to illustrate variability.

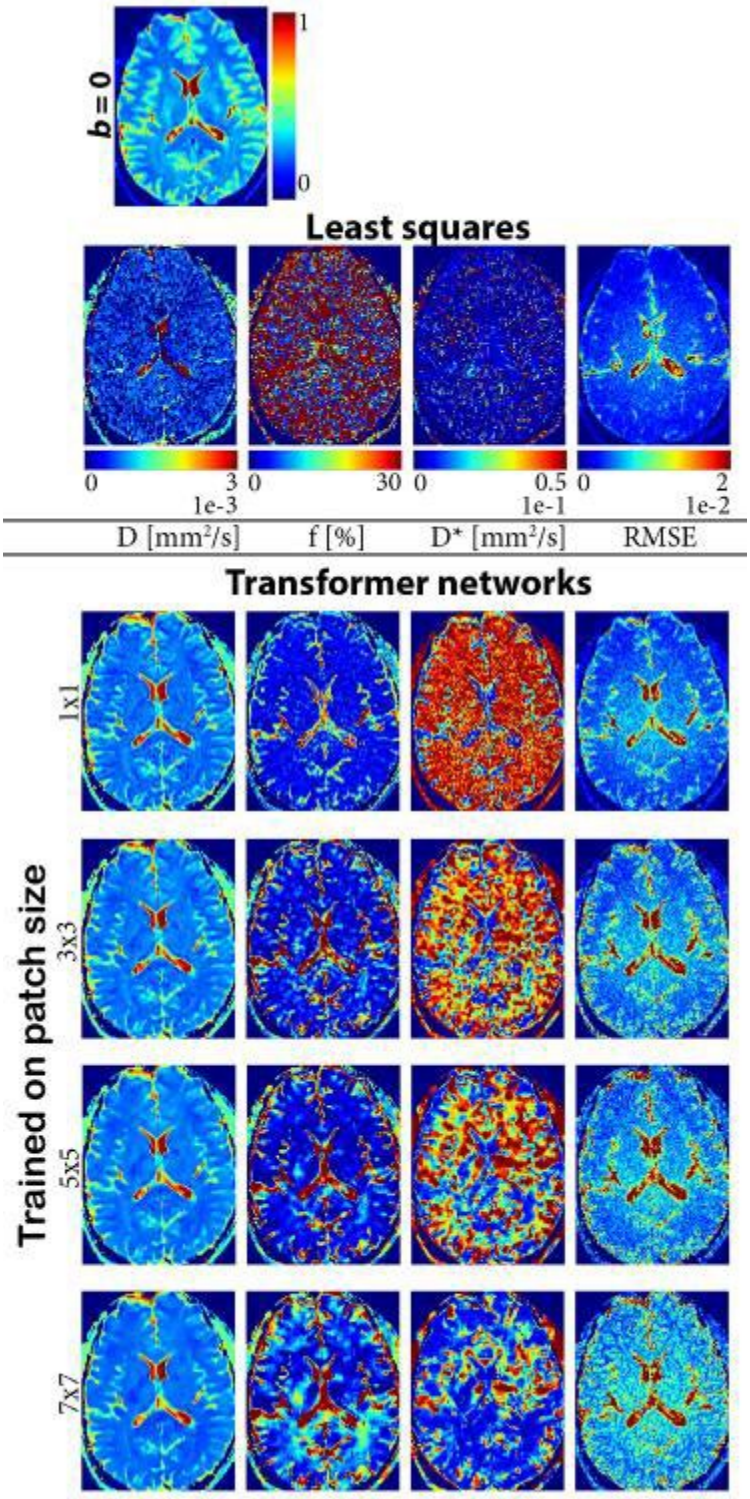

Fig. 4. IVIM parameter maps and RMSE maps for a representative slice from the volunteer scan estimated by the transformer networks trained on different patch sizes.

LB297.

Towards whole-brain diffusion-weighted imaging at 7T using universal multi-band kT-spokes pTx pulses

M. Veldmann[1], D. Löwen[1], E. Pracht[1], P. Ehses[1], R. Stirnberg[1], T. Stöcker[1]

[1]Deutsches Zentrum für Neurodegenerative Erkrankungen (DZNE) e.V., MR Physics, Bonn, Germany

Introduction: MR imaging at ultra-high fields suffers from inhomogeneity of the B1 transmit field. This is especially challenging for whole-brain diffusion-weighted imaging, as typically a spin-echo sequence with large flip-angle slice-selective excitation and refocusing pulses is used.

In this work, we designed slice-selective multi-band pTx pulses for fast plug-and-play whole-brain diffusion imaging using the kT-spokes [1] and universal pulse concepts [2]. We compared this approach to standard multi-band pulses in CP mode.

Methods:

Pulse design:

In a first stage, an initial asymmetric non-selective kT-points pulse (3 kT-points) was optimized on a whole head target across a database of 10 subjects. Based on this, specific pulses per slice position were further optimized through weights that decrease exponentially with increasing distance to the target slice position. In this second optimization stage, the kT-points gradient blips are kept unchanged and the result is still one non-selective pulse per slice [1].

For universal pulse calculation, the ROI of the first slice is aligned with the top of each head in the database.

The two-stage optimized non-selective pulses are then converted to slice-selective bipolar spoke pulses by replacing the rectangular RF shape by a sinc shape with the same flip angle and adding slice-selection gradients [3]. Minimum-time VERSE [4] is applied on the pulses to decrease SAR. The total duration of the pulses was kept approximately the same before and after the application of VERSE.

In the last step, multi-band pulses are created by superposition of the single-band pulses. Examples for resulting multi-band excitation and refocusing pulses are shown in Figure 1.

Acquisition:

Data was acquired on a MAGNETOM 7T Plus scanner (Siemens, Erlangen) from a subject, that was not in the pulse design database.

The multi-band excitation and refocusing pTx pulses (MB-factor 2) were implemented into a product single-shot blipped-CAIPI diffusion-weighted SE-EPI sequence with additional GRAPPA acceleration (R=2). Two b-values (1000/2000 s/mm^2) with 30 diffusion directions each were acquired. Additionally, T2-weighted volumes with zero b-value were obtained with same/inverted phase encoding direction (10/3 volumes).

Other sequence parameters were: slices=110, FOV=210x210x165 mm^3, res=1.5mm iso, PF=6/8, TE=69ms, TR=6.4s, TA=8min. As a reference, the scan was repeated with default multi-band pulses in CP mode.

Preprocessing and quantification:

Images were denoised [5], distortion- and motion-corrected [6]. Fractional anisotropy and mean-diffusivity maps were calculated for both pTx/CP mode datasets from a diffusion-tensor fit [7]. Relative SNR maps were calculated by dividing one of the diffusion-weighted images by the noise map from the denoising step. Images from both scans were registered to a midway space for comparison [8].

Results: Figure 2 shows T2-weighted and diffusion-weighted images after preprocessing. Signal voids in the cerebellum and the center of the brain are observed in CP mode, while these are not present in the pTx images. Lower signal is present in the frontal lobe and the brain stem in the pTx images.

These observations match with the relative SNR maps of the first diffusion-weighted volume (Fig. 3), where SNR in the lower cerebellum is significantly higher in the pTx images. The mean relative SNR in the brain is slightly higher for pTx (14.4) compared to CP (13.4).

Figure 4 shows fractional anisotropy and mean diffusivity maps. Poor DTI fits are represented by increased noise in low-SNR regions.

Discussion: The designed kT-spokes pulses increase SNR in the cerebellum and the center of the brain and improve B1 homogeneity compared to CP mode. This translates to improved quantitative maps such as FA or MD. However, B0 inhomogeneities remain challenging with kT-spokes design, as signal loss is observed in areas with large B0 deviations such as the frontal lobe and the brain stem.

The application of VERSE gradients for SAR reduction is important to reach a reasonable short TR for whole-brain imaging, however it increases the susceptibility to B0 deviations. We observed, that it is crucial to preserve the total pulse duration after applying VERSE.

The concept of universal plug-and-play pulses is especially beneficial for multi-slice diffusion imaging, as designing excitation and refocusing pulses for each slice individually at the MR scanner in an imaging session is currently not feasible due to long computation times.

Conclusion: The designed multi-band kT-spokes pulses improve whole-brain B1 homogeneity in diffusion-weighted images. Large B0 inhomogeneities in the frontal lobe and brain-stem still remain challenging for the pulse design.

References

[1] Gras, NI, 2019
[2] Gras, MRM, 2017
[3] Saib, ISMRM, 2018
[4] Hargreaves, MRM, 2004
[5] Veraart, NI, 2006
[6] Andersson, NI, 2015
[7] Garyfallidis, Front Neuroinform, 2014
[8] Jenkinson, NI, 2002

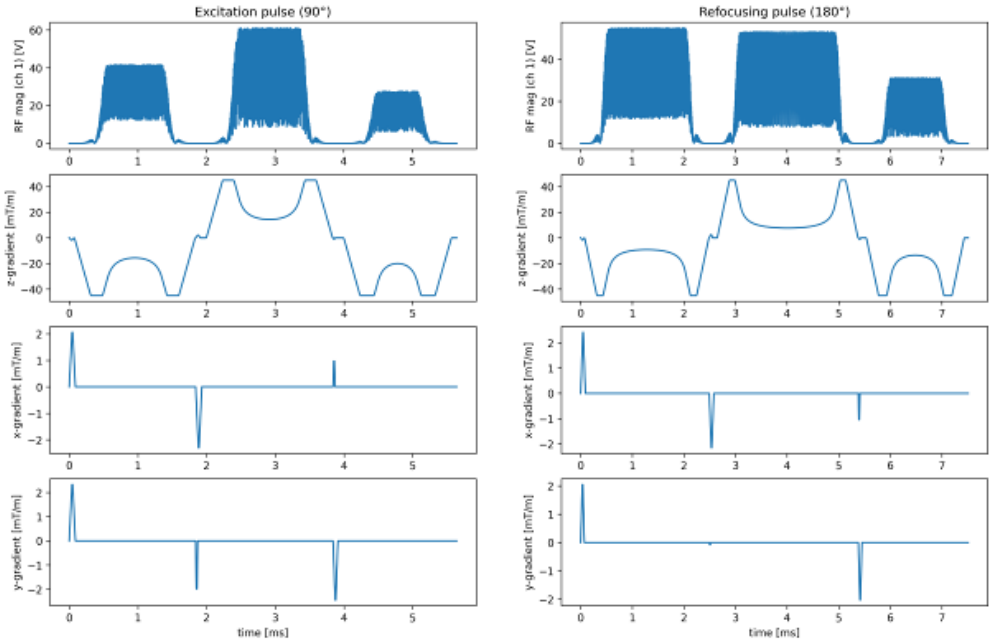

Fig 1: Multi-band kT-spokes excitation and refocusing pulses of one slice group. The magnitude of the first RF channel is displayed in the top row. Below, the slice-selective VERSE-gradient and kT-point blips are shown (x- and y-axes are scaled down for improved visibility of the blips).

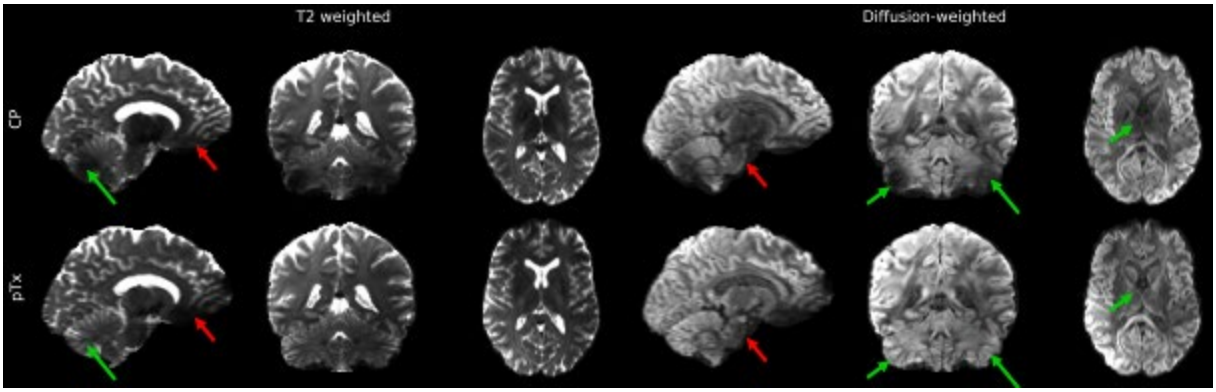

Fig 2: T2- and diffusion-weighted (b=1000s/mm^2) volumes acquired in CP mode and with pTx pulses after preprocessing. Green arrows mark areas, where pTx pulses perform better than CP mode, while red arrows mark areas where CP mode performs better.

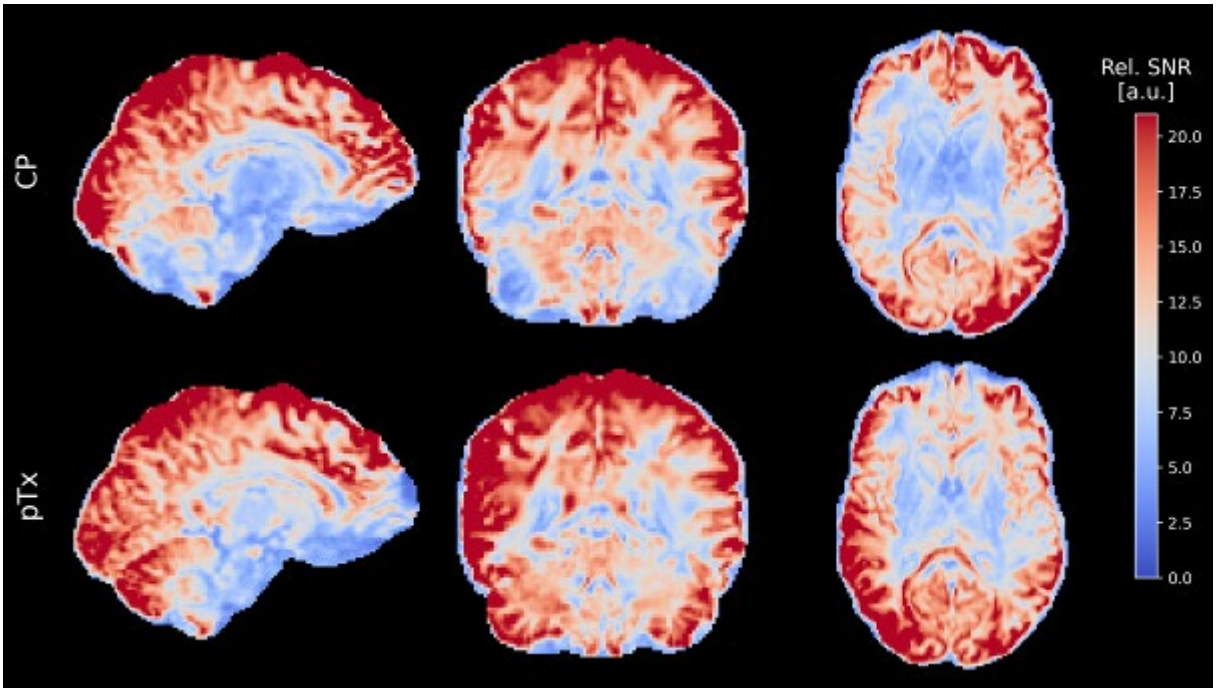

Fig 3: Relative SNR maps of the first diffusion-weighted volume (b=1000s/mm^2). The map was calculated by dividing the diffusion-weighted volume by the noise map from the denoising step.

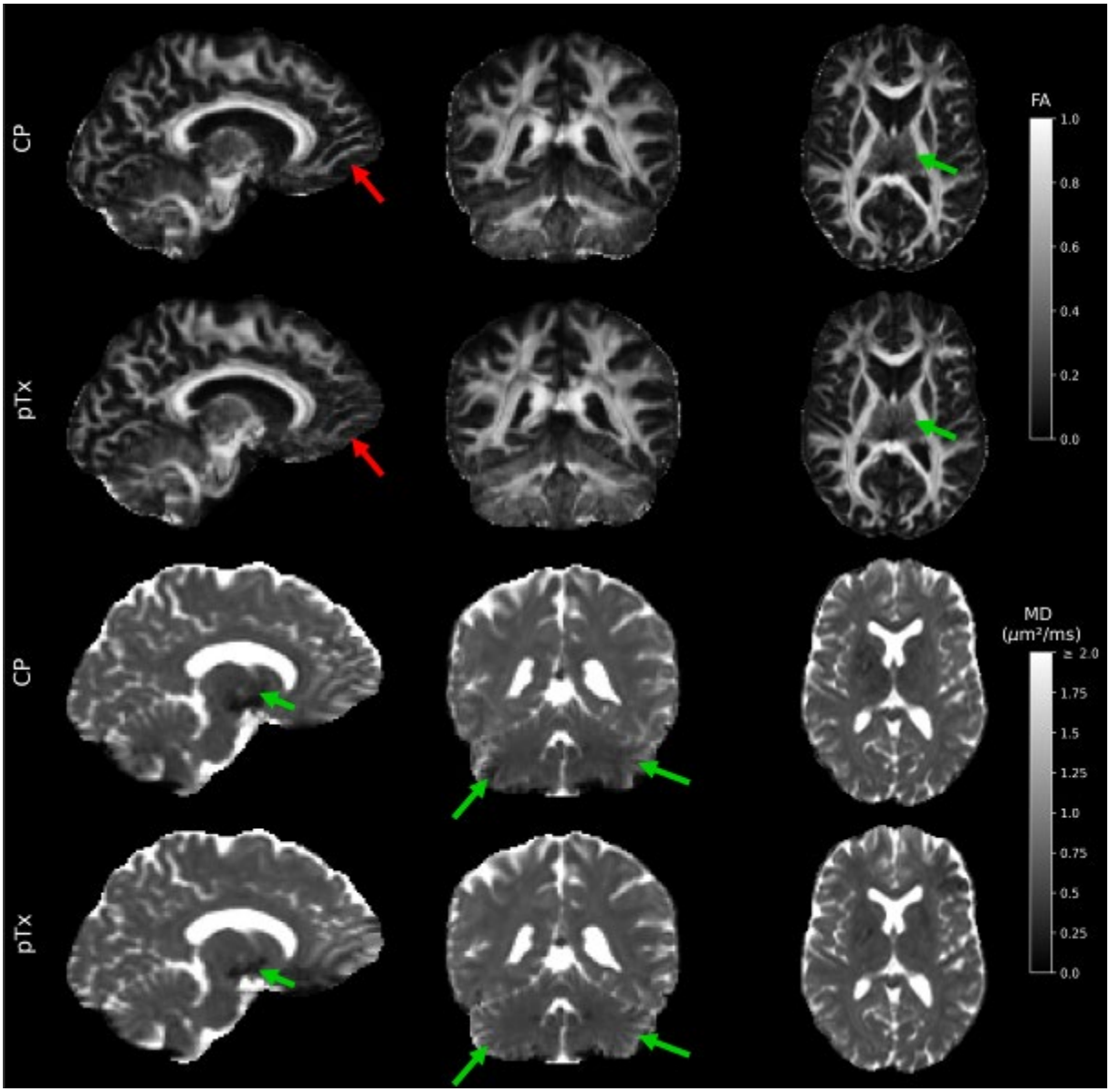

Fig 4: Top two rows: Fractional-anisotropy maps. Bottom two rows: Mean-diffusivity maps. Both maps were obtained from a diffusion tensor fit done for both CP and pTx images. Green/red arrows mark areas with better/worse fit results of pTx compared to CP.

LB298.

Theoretical framework to characterise motion artefacts arising from steady-state diffusion MRI

B. Tendler[1]

[1]University of Oxford, Wellcome Centre for Integrative Neuroimaging, Oxford, United Kingdom

Introduction: Diffusion-weighted steady-state free precession (DW-SSFP)[1] is a powerful diffusion imaging sequence achieving high SNR-efficiency and strong diffusion-weighting (Fig. 1a). To date, the potential of DW-SSFP has been predominantly demonstrated in the post-mortem domain (Fig. 1b)[2]. However, translation of DW-SSFP for in vivo investigations is currently limited by the sequence's severe motion-sensitivity. A key challenge for DW-SSFP is the specialised nature of how motion corrupts the measured signal; unlike conventional diffusion sequences where motion corrupts signal *phase*, in DW-SSFP motion corrupts both the signal *magnitude* and *phase* (Fig. 1c)[3]. Conventional motion-correction methods are unable to account for this form of signal corruption, leading to motion artefacts and incorrect diffusivity estimates.

In this work, I introduce a theoretical framework to characterise the DW-SSFP signal incorporating rigid (translation & rotations) and nonlinear (brain cardiac pulsatility) motion, with Monte Carlo validation. I demonstrate that motion-corrupted DW-SSFP measurements contain sufficient information to estimate and reconstruct the motion-corrected signal.

Theory: DW-SSFP diffusion-encoding consists of a single RF pulse and diffusion gradient per TR (Fig. 1a). Diffusion contrast accumulates over several TRs, forming diffusion gradient pairs similar to spin/stimulated echoes. Motion in each TR induces a unique phase to the magnetisation. The measured signal arises from magnetisation that has experienced different histories of excitation and evolution, leading to the combination of different phase profiles and subsequent magnitude corruption (Fig. 1c). This effect is distinct from the magnitude corruption commonly associated with multi-shot diffusion acquisitions.

The DW-SSFP sequence can be accurately modelled using extended phase graphs (EPG)[4]. To simulate motion, I integrated a coherent bulk motion operator into an EPG framework (Fig. 2). The proposed operator extends the description in Weigel[4] to incorporate (1) gradient duration, (2) rotation and (3) cumulative motion.

Methods: Motion corrupted DW-SSFP time-series data were synthesised incorporating (1) constant translations/rotations and (2) brain cardiac pulsatility (velocity profile based on Greitz et al.[5]). Validation was performed with complementary Monte-Carlo simulations (Camino[6], 10^5 particles, 100 time-steps per TR, $D=1\cdot10^{-3}$ mm^2/s). To additionally visualise the impact of motion, I synthesised motion-corrupted DW-SSFP images assuming a single-shot readout.

To investigate whether the DW-SSFP signal contains sufficient information to estimate motion, simulations were performed using DW-SSFP time-series data incorporating brain cardiac pulsatility and Gaussian noise, reflecting measurements from a single voxel. Fitting (MATLAB *lsqnonlin*) estimated (1) the diffusion-coefficient and (2) the velocity profile over a steady-state signal region.

Simulations based on Miller & Pauly[7] (G=40 mT/m, δ=6.5 ms, TR=40 ms, α=30°). T_1/T_2 fixed to average estimates in white matter at 3T[8] (832/110 ms).

Results: Fig. 3a & b compares the estimated motion-corrupted DW-SSFP time-series for (1) constant translations/rotations (Fig. 3a) and (2) brain cardiac pulsatility (Fig. 3b). Excellent agreement is found between the proposed EPG framework and Monte Carlo Simulations. The DW-SSFP pulsatility time-series (Fig. 3b) reveals excellent visual agreement with experimental DW-SSFP data displayed in Miller & Pauly[7].

Fig. 3c visualises the impact of translation, rotation, and pulsatility on DW-SSFP images. All three types of motion lead to signal attenuation and phase accumulation. Pulsatility simulations reveal good visual agreement with experimental DW-SSFP images displayed in Miller & Pauly[7].

Fig. 4 displays the estimated DW-SSFP time-series and velocity profile fitting to simulated DW-SSFP data incorporating pulsatility and noise. I observe excellent agreement over the fitted data region, estimating $D=0.95\cdot10^{-3}$ mm^2/s (5% difference). No motion correction estimates $D=2.3\cdot10^{-3}$ mm^2/s (130% difference).

Discussion: Motion leads to considerable DW-SSFP signal corruption. Agreement between the proposed EPG framework and Monte Carlo simulations (Fig. 3) demonstrates that continuous motion profiles can be captured with a

single parameter per TR. Motion-induced signal perturbations can be reliably estimated to accurately characterise diffusivity (Fig 4).

Conclusion: Motion can be simulated and predicted from the measured DW-SSFP signal. Future work will explore the integration of this framework with conventional motion-correction methods (e.g. navigators), with the aim of addressing DW-SSFP motion artefacts in vivo.

References

1. Le Bihan, *MRM* '88
2. Miller et al., *Neuroimage* '12
3. O'Halloran et al., *MRM* '14
4. Weigel, *JMRI* '15
5. Greitz et al., *Neuroradiology* '92
6. Hall et al., *IEEE Trans Med Imaging* '09
7. Miller & Pauly, *MRM* '03
8. Wansapura et al., *JMRI* '99

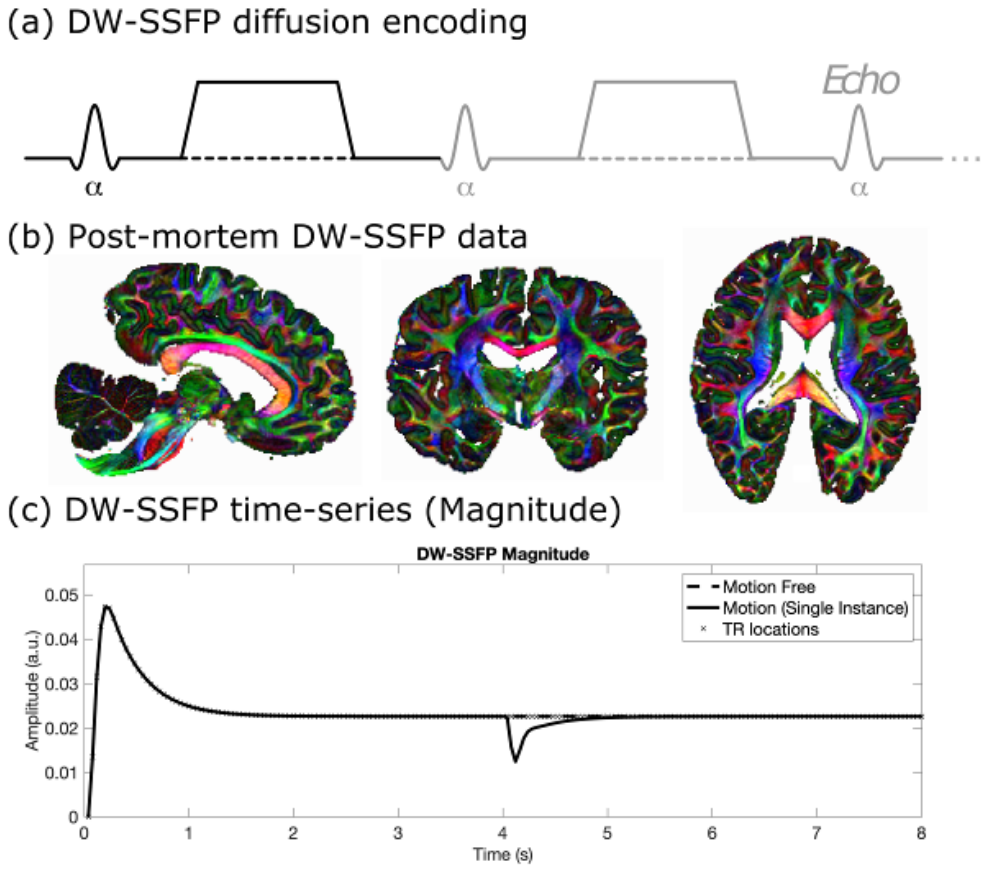

Fig. 1: (a) DW-SSFP diffusion encoding. (b) Human post-mortem DW-SSFP tensor estimates (0.85 mm iso.). (c) Simulated DW-SSFP time-series magnitude data. The signal eventually reaches a steady state, with motion perturbing the signal over several measurements.

The coherent bulk motion operator is expressed as:

$$\mathbf{J_{Motion}}(t) = \begin{bmatrix} e^{-i\cdot\frac{k_j+k_{j+1}}{2}\delta\cdot T(t)}\cdot e^{-i\cdot k_{j+1}\cdot(TR-\delta)\cdot T(t)} & 0 & 0 \\ 0 & e^{i\cdot\frac{k_j+k_{j+1}}{2}\delta\cdot T(t)}\cdot e^{i\cdot k_{j+1}\cdot(TR-\delta)\cdot T(t)} & 0 \\ 0 & 0 & e^{-i\cdot k_j\cdot TR\cdot T(t)} \end{bmatrix}, \quad [1]$$

where:

$$T(t) = \vec{v}(t)\cdot\hat{g} + \left(\hat{g}\times\vec{\theta}(t)\right)\cdot\vec{X}(t). \quad [2]$$

Operators are time-dependent and account for cumulative motion, defining:

$$\vec{X}_{(n+1)\cdot TR} = \boldsymbol{R}\left(\overrightarrow{\delta\theta}_{(n+1)\cdot TR}\right)\vec{X}_{n\cdot TR} + \overrightarrow{\delta v}_{(n+1)\cdot TR}. \quad [3]$$

k_j = dephasing order, δ = gradient duration, $\hat{g}$ = gradient orientation, $\vec{v}(t)$ = velocity, $\vec{\theta}(t)$ = rotational velocity, $\vec{X}(t)$ = position, $\boldsymbol{R}(\overrightarrow{\delta\theta}) = \boldsymbol{R_z}(\delta\theta_z)\boldsymbol{R_y}(\delta\theta_y)\boldsymbol{R_x}(\delta\theta_x)$, $\overrightarrow{\delta\theta_t} = \vec{\theta}(t)\cdot\mathrm{TR}$ and $\overrightarrow{\delta v_t} = \vec{v}(t)\cdot\mathrm{TR}$.

Fig. 2: Proposed bulk motion operator.

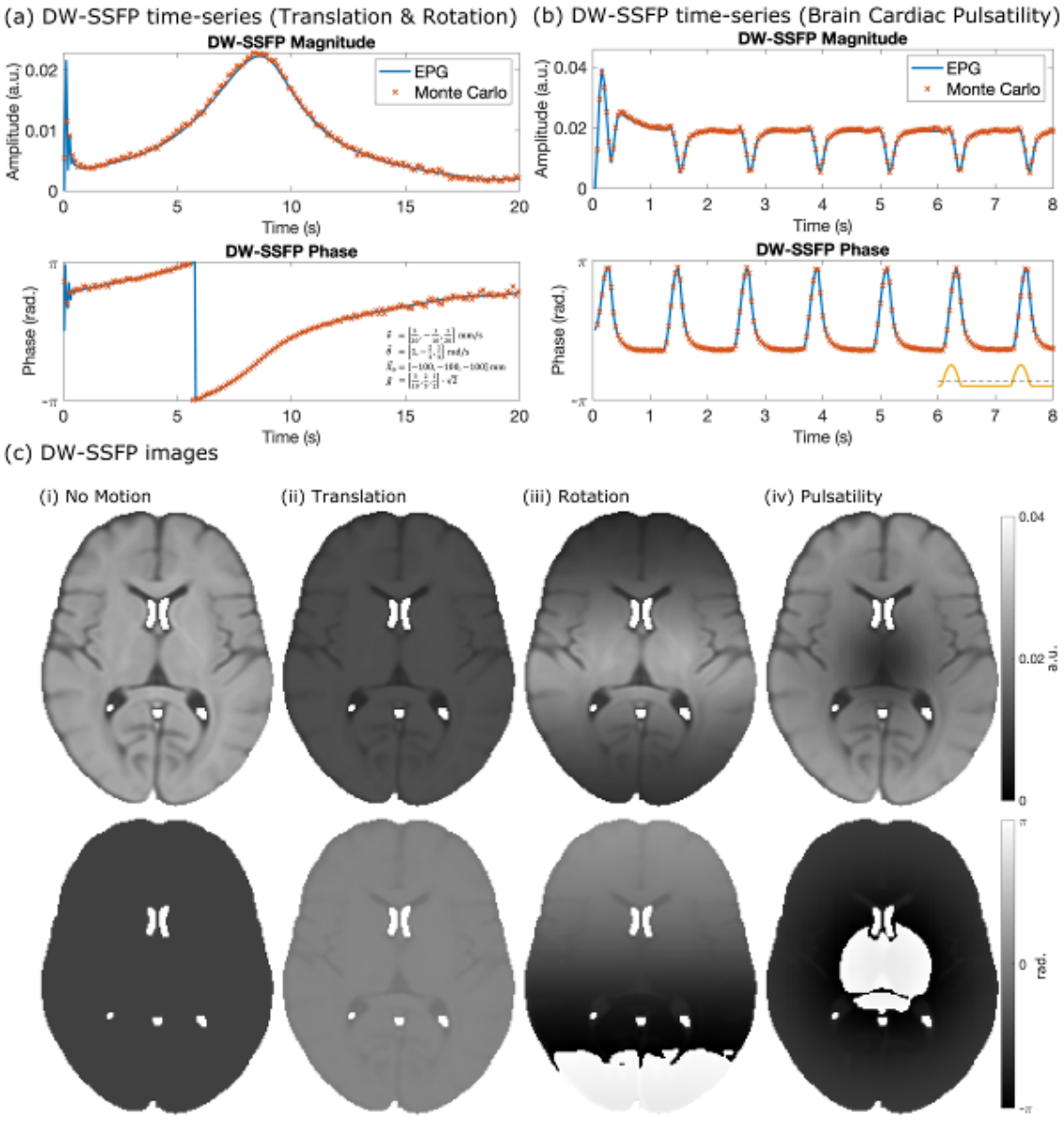

Fig. 3: Modelled motion-corrupted DW-SSFP time-series data with complementary Monte Carlo simulations for (a) translation/rotation and (b) pulsatility. Motion parameters and velocity profile (last two heartbeats) provided in plots. (c) Impact of motion on DW-SSFP images incorporating (ii) constant translation (v=[0.1,0,0] mm/s), (iii) constant rotation (θ=[0,0,0.1] rad/s) and (iv) pulsatility. Images synthesised from HCP1065 DTI template (g=[1,0,0]).

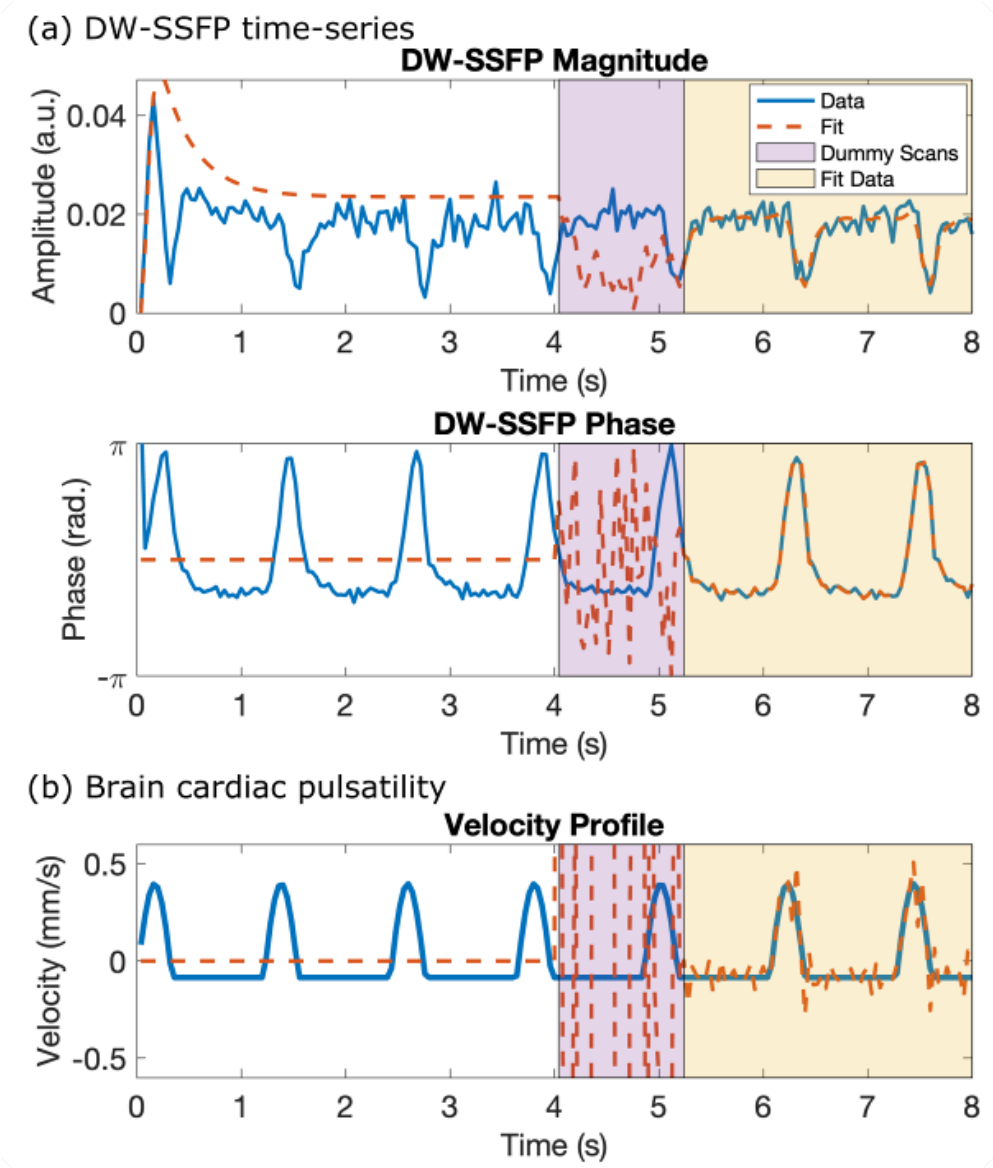

Fig. 4: (a) DW-SSFP signal simulated with pulsatility + noise (blue). Proposed model accurately characterises the DW-SSFP time-series profile (red) in the fitted region (yellow). (b) Estimated velocity profile closely matches in fitted region.

LB299.

Detection of Alzheimer's disease in diffusion tensor imaging data using Mahalanobis distance-based outlier detection

Y. Pauli[1], M. D. Noseworthy[2,3]

[1]ETH Zürich, Zurich, Switzerland
[2]McMaster University, School of Biomedical Engineering, Hamilton, Canada
[3]McMaster University, Department of Radiology, Hamilton, Canada

Introduction: The development of a treatment or cure of Alzheimer's disease (AD) is heavily dependent on the possibility of an early in vivo diagnosis. Presently, a definitive diagnosis can only be established postmortem. However, there have been notable advancements in various promising approaches for early diagnosis, which continue to be the subject of intense investigation. Studies have shown that Alzheimer's disease alters white matter structures in the human brain.[1] Many promising approaches currently under investigation are based on automated disease detection using various machine learning methods.[2,3] Our current work introduces and investigates one such potential tool for early identification of suspected AD. Specifically, our study focused on utilizing Mahalanobis distance-based outlier detection within diffusion tensor imaging (DTI) data.

Methods: The DTI data used in this study consisted of 1158 healthy control subjects and 54 AD subjects. To maintain data homogeneity all images were acquired with a B0 field strength of 3 Tesla and only images with at least 30 gradient directions were used. The age of all subjects included in this study was between 60 and 70 years. DTI data was processed using eddy_correct and dtifit of FSL.

The DTI data of each subject was divided into 18 different regions of interest (ROIs) using binary masks of the JHU DTI-based white-matter tractography atlas. To ensure noise and dimensionality reduction principal component analysis was applied on the DTI metrics fractional anisotropy, axial diffusivity, mean diffusivity and radial diffusivity. An example image of the fractional anisotropy of an AD and a healthy control subject is shown in Figure 1. The Mahalanobis distance for the data analysis was then calculated on the first two principal components of each DTI metric.

Except in the last analysis step, where the whole brain of a subject was considered, a subject was classified as AD if at least one ROI was determined to be an outlier region compared to all healthy control subjects. The analysis did not distinguish the number of ROIs identified as outliers within each subject. Outliers were determined using the probability point function with a confidence interval of 0.9997.

In the last analysis step all ROIs were considered simultaneously by applying the Mahalanobis distance on all 18 Mahalanobis distances for each ROI of a subject. An AD subject was classified as different if the newly calculated Mahalanobis distance was considered an outlier compared to the respective Mahalanobis distance of each subject in the healthy control population.

Results: Out of 1158 healthy control subjects 357 were considered outliers setting the rate of healthy control subjects falsely identified as outliers at 30.83%. The outlier identification rate of AD subjects was 59.26% with 32 out of 54 subjects being classified as outliers. AD subjects aged between 60 and 65 years had a significantly higher outlier identification rate (80.77%) than AD subjects aged between 65 and 70 years (39.29%). Female AD subjects had with 72.72% a higher outlier identification rate than male subjects with 50%. Both these trends were not visible within the healthy control population where the outlier identification rate stayed constant at about 30%.[Table 1] ROIs which were more prevalent as outlier regions in AD subjects included the callosal body, optic radiation left and right, and the superior occipito-frontal fascicle left and right.[Table 2] Considering all ROIs simultaneously did not change any of the trends but improved the outlier identification rate of AD subjects slightly.

Discussion and Conclusions: The rate of falsely identified outlier subjects within the healthy control population was surprisingly high (30%). This high rate of false positives is likely due to high variance within DTI data, especially in the elderly.[4] However, we still showed a higher rate of true positives in the suspected AD patients, despite the underlying issue of high variability. Interestingly, suspected AD outlier detection showed higher true positive rates in younger subjects and also female patients. We believe that higher variance within DTI data of older subjects makes differentiating between healthy subjects and suspected AD patients more difficult and therefore less successful.

Our work seems to show greater promise in detecting early-stage AD within younger cohorts. Future work would benefit from more balanced data (i.e. more AD patients) and also smaller ROI sizes (i.e. here we divided the brain into only 18 ROIs).

References:
[1] C.E. Sexton et al. Neurobiol. Aging, 32(12):2322.e5–2322.e18, 2011.
[2] F.J. Martinez-Murcia et al. J. Biomed. Health Inform. 24:17– 26, 2020.
[3] R. Prajapati et al. 2021 International Conference on Artificial Intelligence in Information and Communication (ICAIIC), 2021.
[4] X. Zhou et al. Magn. Reson. Imaging, 53:105–111, 2018.

Subject Group	Healthy control subjects (Total: 1158)		Alzheimer's Disease subjects (Total: 54)	
	At least one outlier ROI	All ROIs simultaneously considered	At least one outlier ROI	All ROIs simultaneously considered
Female	31.63%	26.38%	72.72%	68.18%
Male	29.66%	27.97%	50%	68.75%
60 – 65 yrs old	30.48%	27.35%	80.77%	76.92%
65 – 70 yrs old	31.08%	26.80%	39.29%	60.71%
All subjects	30.83%	27.03%	59.26%	68.52%

Table 1: Outlier detection rates (ODR) of healthy control subjects and Alzheimer's Disease subjects with respect to age and sex.

ROI	ODR HC	ODR AD	Ratio AD / HC
Acoustic Radiation L	6.56	3.70	0.56
Acoustic Radiation R	5.87	1.85	0.32
Callosal Body	5.61	24.07	4.29
Cingulum L	10.71	20.37	1.90
Cingulum R	10.02	22.22	2.22
Corticospinal Tract L	3.97	1.85	0.47
Corticospinal Tract R	3.71	1.85	0.50
Fornix	0.86	0	0
Inferior Occipito Frontal Fascile L	7.94	3.70	0.47
Inferior Occipito Frontal Fascile R	6.30	5.56	0.88
Optic Radiation L	3.45	14.81	4.29
Optic Radiation R	6.04	24.07	3.98
Superior Longitudinal Fascicle L	6.48	11.11	1.72
Superior Longitudinal Fascicle R	7.17	11.11	1.55
Superior Occipito Frontal Fascicle L	11.31	35.19	3.11
Superior Occipito Frontal Fascicle R	13.04	42.59	3.27
Uncinate Fascicle L	7.08	9.26	1.31
Uncinate Fascicle R	5.61	1.85	0.33

Table 2: Outlier detection rates (ODR) of healthy control subjects (HC) and Alzheimer's Disease subjects and the ratio thereof.

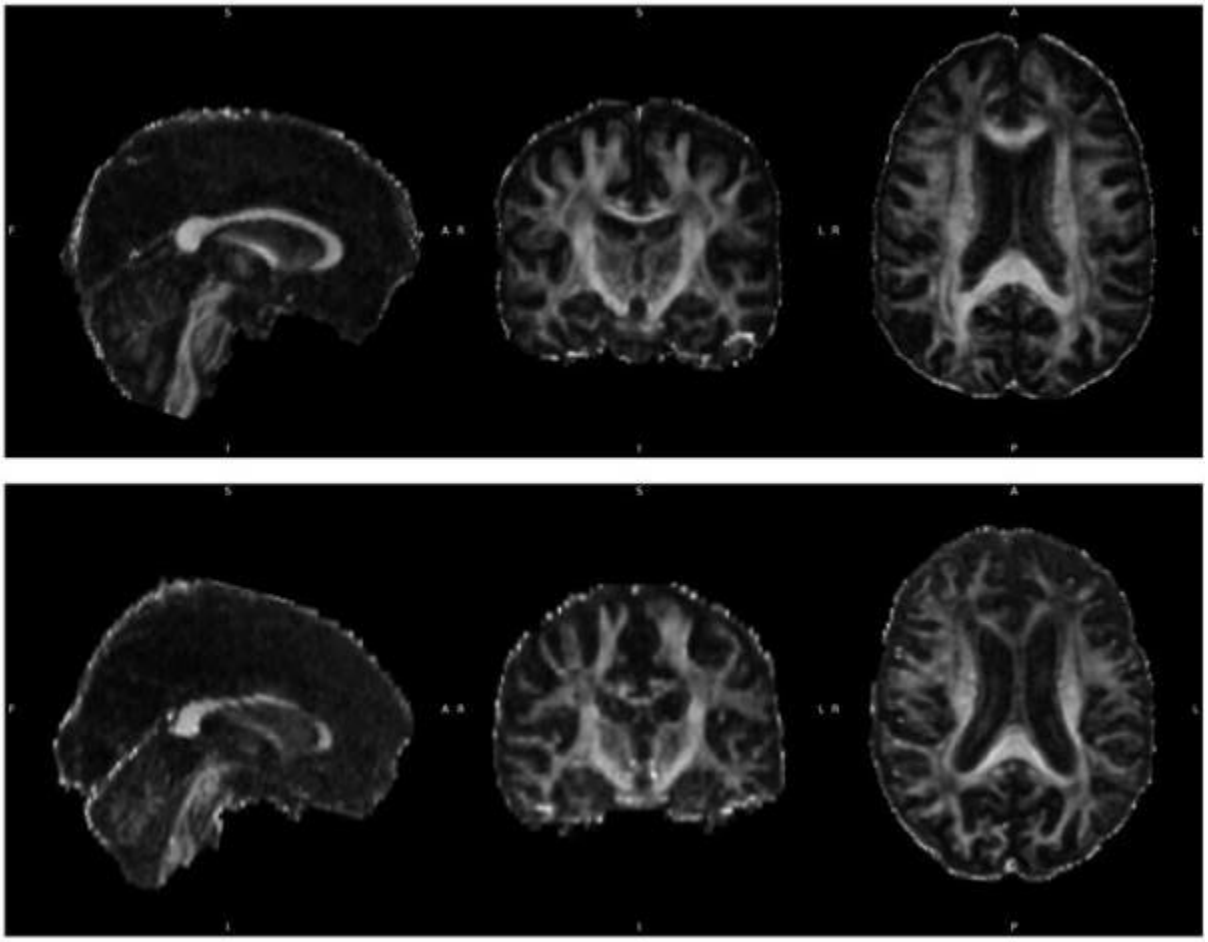

Figure 1: Fractional Anisotropy of an AD subject (top) and a healthy control subject (bottom).

LB300.

Assessing Measurement Consistency of a Diffusion Tensor Imaging (DTI) Quality Control (QC) Phantom

N. Simard[1], A. Fernback[2], N. Konyer[3], F. Kerins[2], M. D. Noseworthy[1,4,5,3]

[1]McMaster University, Electrical and Computer Engineering, Hamilton, Canada
[2]PreOperative Performance, Toronto, Canada
[3]St. Joseph's Healthcare Hamilton - Charlton Campus, Imaging Research Centre, Hamilton, Canada
[4]McMaster University, Department of Radiology, Hamilton, Canada
[5]McMaster University, School of Biomedical Engineering, Hamilton, Canada

Diffusion Tensor Imaging (DTI) is a valuable non-invasive tool that has potential to be an effective imaging biomarker for a variety of neuropathologies, reducing medical error [1]. However, data reliability and comparability of DTI sequences across imaging platforms limit the validation of DTI in large scale multicenter studies [2]. Furthermore, MRI system stability makes repeated temporal measures difficult to quantitatively compare, thus limiting the use of DTI. As such, a quantitative reference phantom for QC is presented that has the potential to validate accuracy of in vivo measurements across both time and vendor. Although alternatives such as routine imaging phantoms and standardization through travelling human "phantoms" exist, none are capable of quantifying temporal and imaging platform variations [2,3]. As DTI has applications in neurosurgery the need for QC, data reliability, and reduced medical error is essential. Therefore, in this work, the goal was to investigate DTI across 3 vendors by scanning a specific QC phantom that is designed to mimic a neurological environment with multi directional fibers, crossing fibers, and appropriate brain relaxivity values.

Methods: A proprietary DTI phantom (**Fig.1**) was designed and fabricated by PreOperative Performance (Toronto Canada). The phantom contained vials of varying ADC values and also fiber bundles to mimic white matter. The phantom was scanned using a research-dedicated GE MR750 3T MRI system and 32 channel head coil (software ver. 29.1, GE HealthCare, Milwaukee WI). To test consistency of measurements 8 separate DTI scans were performed to match what can be done on a clinical system (32 directions, b=1000s/mm2, 4 b=0s/mm2 images, 2mm isotropic voxels, 70 slices). Real-time field adjustment, a newer DTI feature on this scanner, was included to avoid the need for a Bo map. Because motion probing gradients (MPGs) are different across vendors we performed identical measures using MPGs from Philips and Siemens as well. All data was subsequently processed using *eddy_correct* and *dtifit* from FSL [4] and resulted in fractional anisotropy (FA) and mean diffusivity (MD) maps. Image co-registration was subsequently performed using the FSL command *flirt* using a 12 degree of freedom (df) trilinear interpolation. Lastly, to assess consistency in both time and across imaging platforms a 2-way 3d ANOVA was performed on both FA and ADC maps, over the entire phantom, using the AFNI command 3dANOVA2 with "repeat" and "vendor" as factors.

Results: Based on false discovery rate (FDR) corrected p-values, F-statistics calculated using a 3D 2-way ANOVA showed there was no appreciable difference in either FA or MD across vendors MPGs and time (**Fig.2**). The variation in global FA values between all three vendors, and in data at different time points, was 0.32%. There were no appreciable differences in fiber FA values when comparing across vendor"s MPGs and across time (**Fig.3**). Similarly with mean diffusivity (MD) the variation across all scans was 0.0019% (**Fig.3**).

Discussion: Based on our results the phantom is vendor agnostic and stable over time. This DTI QC phantom contains anisotropic diffusion modules of a well-defined filament material that approximates the size and scale of the myelinated axons of white matter. Inside the phantom is a modular scaffold that supports a plurality of arrangements of fiber bundle networks such that network terminus and bifurcation/intersection locations are in desired locations and orientations. Additional isotropic diffusion modules composed of isolated domains contained a solution with predictable ADC properties and are co-located on this inner-housing system. The inner housing elements are immersed with a suitable matrix fluid producing biologically relevant T1 and T2 values.The PreOperative Performance QC phantom is a solution for temporal and multisite/multivendor comparison of DTI data. It demonstrates that reliability and comparability of data obtained across imaging platforms is possible, providing vendors the ability to standardize their protocols. This QC phantom, specifically designed for DTI, further eliminates the logistical hurdles associated with travelling human "phantoms" and ensures appropriate calibration to the DTI sequences across vendors. This can further unlock more capabilities of the DTI sequence to improve pre-surgical planning, more accurately investigate white matter pathway disruptions, improve fiber tracking, help us better understand human brain connectivity, and finally become a more effective imaging biomarker in a variety of neuropathologies. This phantom could perform as a component of a quality assurance (QA) system if it were to include the phantom, agreed upon reference standards and the method(s) of data analysis.

[1] Rolston et al. (2014) Surg. Neurol. Int. 5:S435. **[2]** Tong et al. (2020) Sci. Data. 7(1):157. **[3]** Souza et al. (2017) Res. Biomed. Eng. 33:156. **[4]** Jenkinson et al. (2012) 62:782

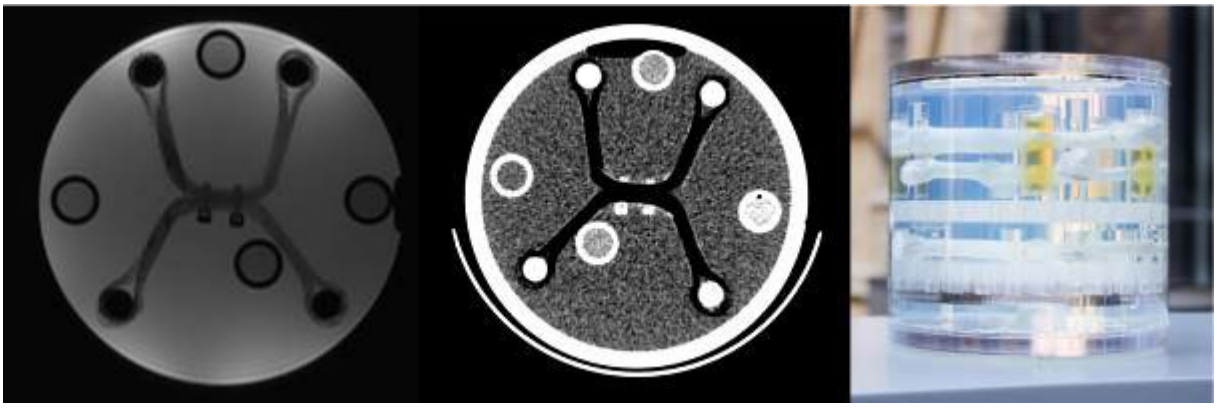

Fig 1. Proton density (PD) weighted image (3T), CT scan and photograph of the DTI QA phantom (PreOperative Performance, Toronto, ON, Canada)

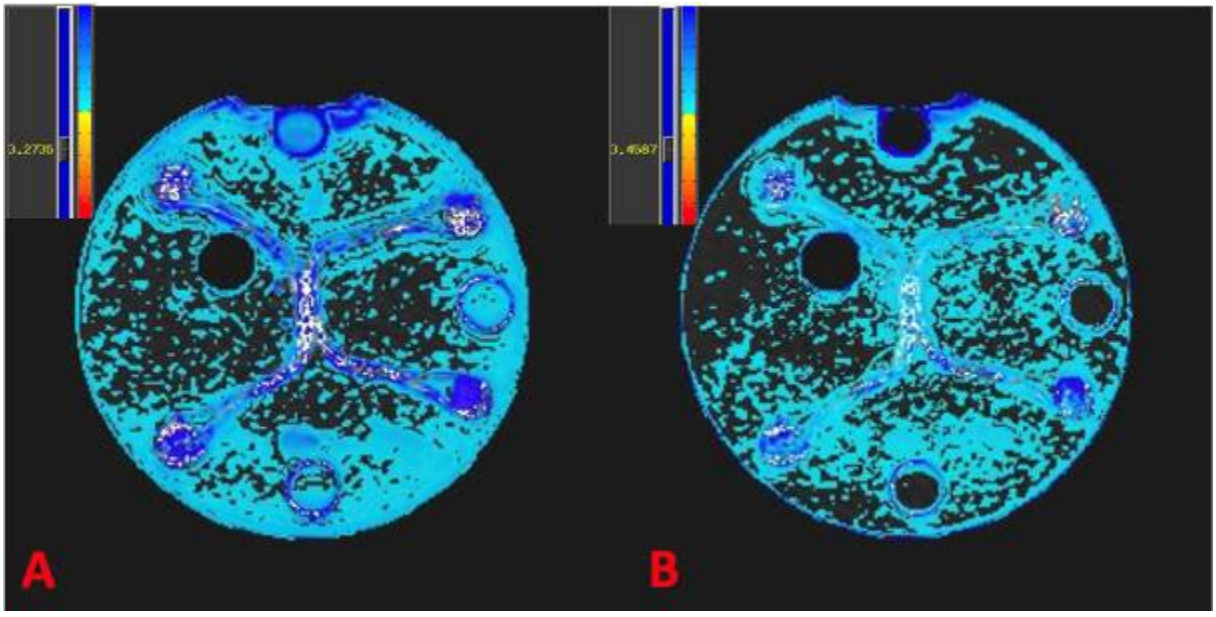

Fig 2. F-statistic (FDR corrected, $p<0.05$) maps through phantom fibers showing (A) statistical model of FA through different vendor MPGs over time; and (B) statistical model of MD. No appreciable differences were noted.

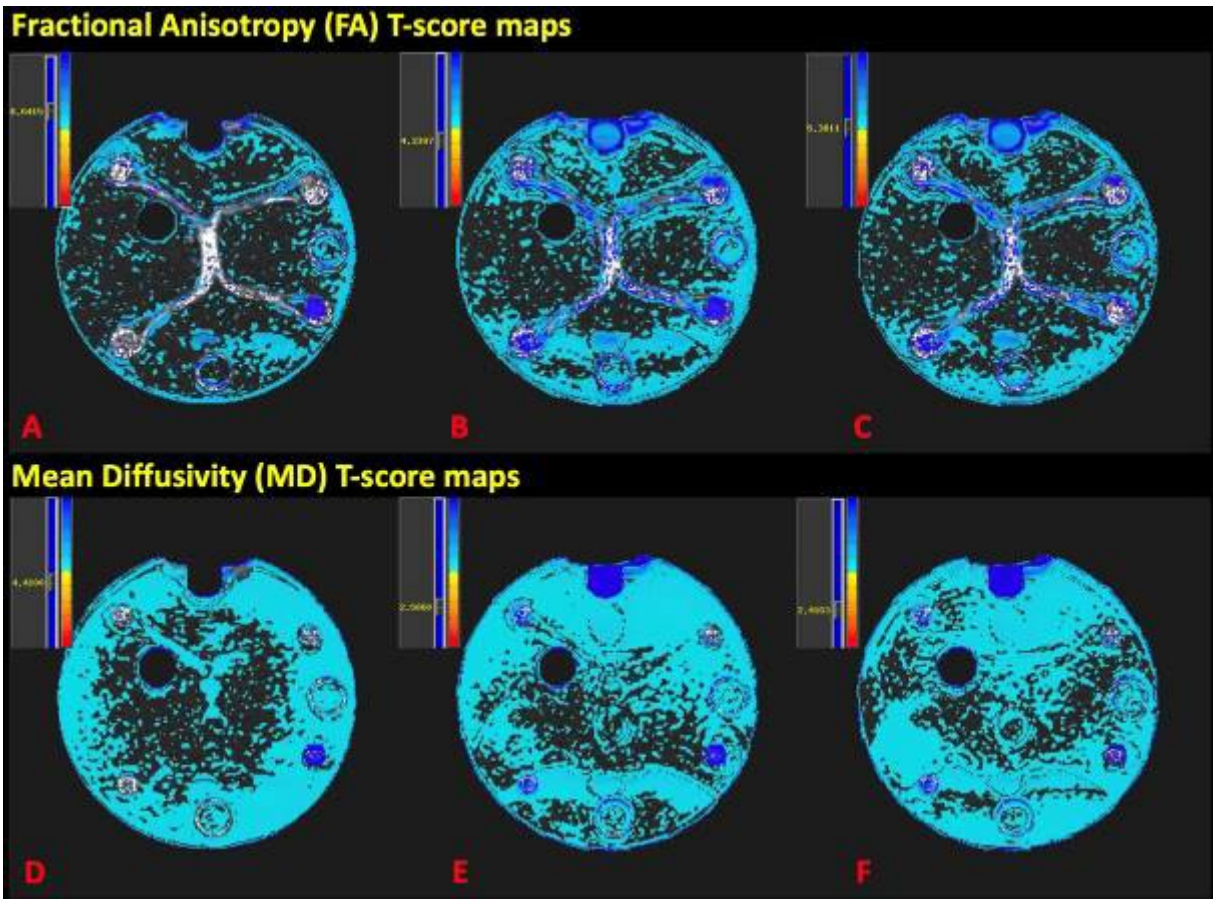

Fig 3. Bonferonni corrected ($p<0.05$) T-score FA maps (top row) and MD maps (bottom row) through phantom fibers showing (A and D) differences between GE and Philips; (B and E) Philips and Siemens; and (C and F) Siemens and GE. There was a 0.32% variation in FA values, and 0.0019% variation in MD values between data acquired at different times and with different vendor MPGs. Neither FA nor MD values were appreciably different across time or vendor.